CDF 6681
version 2.0

Measurements of $\sigma \cdot B(W \rightarrow e\nu)$, $\sigma \cdot B(Z \rightarrow ee)$ and $R = \frac{\sigma \cdot B(W \rightarrow e\nu)}{\sigma \cdot B(Z \rightarrow ee)}$ using CDF Run II Data

Dan Amidei[1], Ken Bloom[1], Mircea Coca[2], Eva Halkiadakis[2] *,
Eric James[3], Jian Kang[1], Young-Kee Kim[4], Giulia Manca[5], Victoria Martin[6],
Pasha Murat[3], Aidan Robson[5], Willis Sakumoto[2], Michael Schmitt[6],
Greg Veramendi[7], Alexei Varganov[1]

1 *University of Michigan, Ann Arbor, Michigan*
2 *University of Rochester, Rochester, New York*
3 *Fermi National Accelerator Laboratory, Batavia, Illinois*
4 *Enrico Fermi Institute, University of Chicago, Chicago, Illinois*
5 *University of Oxford, Oxford, United Kingdom*
6 *Northwestern University, Evanston, Illinois*
7 *Ernest Orlando Lawrence Berkeley National Laboratory, Berkeley, California*
∗ To whom correspondence should be addressed: evah@fnal.gov

February 24, 2004

Abstract

The cross sections of the W and Z bosons decaying into an electron and a neutrino or an electron-positron pair, respectively, are measured using high p_T electron data from the CDF Run 2 detector at the Fermilab Tevatron. We measure these cross sections for the first time at a center-of-mass energy of 1.96 TeV. The data were collected between March 2002 and January 2003, with total integrated luminosity of 72.0 pb^{-1}. Our measurement yields $\sigma \cdot B(W \rightarrow e\nu) = 2.781 \pm 0.015(stat) \pm^{0.057}_{0.062} (syst) \pm 0.167(lum)$ nb for cenral electrons and $\sigma_Z \cdot Br(\mathrm{Z}^0 \rightarrow \mathrm{e}^+\mathrm{e}^-) = 256.3 \pm 3.9(stat.) \pm 5.3(syst.) \pm 15.3(lum.)$ pb for a combined central-central and central-plug electron analysis. These measurments agree well with both the theoretical predictions at $\sqrt{s} = 1.96$ TeV and the Run Ia measurement after accounting for the change in the center-of-mass energy. We also measure $R = \frac{\sigma \cdot B(W \rightarrow e\nu)}{\sigma \cdot B(Z \rightarrow ee)} = 10.85 \pm 0.18(stat.) \pm^{0.19}_{0.18} (syst.)$.

Contents

List of Tables

List of Figures

Part I

Introduction

Since their discoveries in 1983, many of the intrinsic properties of the Z boson have been examined in great detail via e^+e^- collisions at LEP at CERN and the SLC at SLAC, and the W boson properties have been studied via e^+e^- collisions at LEP and via $p\bar{p}$ collisions at the SPPS at CERN and the Tevatron at Fermilab. The mass of the Z boson measured at LEP has an accuracy of about two parts in 10^5 [1], and the mass of the W boson measured at LEP and the Tevatron has an accuracy of about four parts in 10^4 [2]. In addition, the total width and branching ratios of the Z boson are accurately measured [1]. These precision measurements focus on the electroweak character of the vector bosons.

At the Tevatron, where the W and Z bosons are produced in $p\bar{p}$ collisions, their production properties can be characterized by QCD. Since the electroweak properties of the vector bosons are not correlated with the QCD properties of their production, the vector bosons can therefore serve as a clean probe of the strong interactions. The large mass of the W and Z bosons assures a large energy scale ($Q^2 \sim M_Z^2$ to M_W^2) for probing perturbative QCD with good reliability.

At the upgraded Tevatron energy of $\sqrt{s} = 1.96$ TeV, perturbative QCD predicts an increase of about 40% from leading order (LO) to next-to-leading order (NLO) calculations and additional increase of about 4% from NLO to next-to-next-to-leading order (NNLO) calculations in the production cross section of the vector bosons [3]. These can be compared with 20% from LO to NLO and 3% from NLO to NNLO at $\sqrt{s} = 1.8$ TeV [4; 5; 6]. Furthermore, the vector boson production cross section at $\sqrt{s} = 1.96$ GeV is expected to be about 9% higher than the cross section at $\sqrt{s} = 1.8$ GeV.

The product of the production cross section and the leptonic branching ratio for the W and Z bosons, $\sigma_W \cdot Br(W \rightarrow \ell\nu)$ and $\sigma_Z \cdot Br(Z \rightarrow \ell^+\ell^-)$, has been measured at $\sqrt{s} =$ 630 GeV at the SPPS $p\bar{p}$ collider [7; 8] and at $\sqrt{s} = 1.8$ GeV at the Tevatron $p\bar{p}$ collider by the CDF [9; 10; 11] and D0 [12] collaborations. In this paper, we report the first measurements of $\sigma_W \cdot Br(W \rightarrow \ell\nu)$ and $\sigma_Z \cdot Br(Z \rightarrow \ell^+\ell^-)$ in the electron channel (and muon channel to follow) at $\sqrt{s} = 1.96$ TeV using the upgraded Tevatron and the upgraded CDF detector.

The ratio of W and Z cross sections times branching ratios can be expressed as

$$R = \frac{\sigma_W \cdot Br(W \rightarrow \ell\nu)}{\sigma_Z \cdot Br(Z \rightarrow \ell^+\ell^-)} = \frac{\sigma_W}{\sigma_Z} \cdot \frac{\Gamma(W \rightarrow \ell\nu_\ell)}{\Gamma(W)} \cdot \frac{\Gamma(Z)}{\Gamma(Z \rightarrow \ell^+\ell^-)}, \quad (1)$$

where $\ell = e, \mu$. With the theoretical prediction of the production cross sections and the partial and total width measurements of the Z boson from the LEP experiments, we extract the leptonic branchings ratios of the W boson, $\Gamma(W \rightarrow \ell\nu_\ell)/\Gamma(W)$. Using a Standard Model calculation for the W partial width, we indirectly measure the total width of the W boson. The W branching ratio and total width are well predicted by the Standard Model, so the comparison represents a precision test of the consistency of electroweak theory.

The remainder of the paper is organized as follows. In the next part we describe the datasets used for this paper and the corrections applied to energy and momentum measurements. We also discuss the Monte Carlo generation and simulation in part III. The event selection criteria in described in part IV. Background estimation is presented in part V. Detector acceptances and lepton identification efficiencies are the subjects of parts VI and VII. We present our results and conclusions in parts 21 and IX.

Part II

Datasets

1 Triggers

The data for this analysis are selected using the good runs (see section 3) from 23 Mar 2002 until 12 Jan 2003 (141544-156487). This dataset originates from the Stream B Inclusive high p_T Central Electron Sample. We select the ELECTRON_CENTRAL_18 trigger path:

- **Level 1:** L1_CEM8_PT8. This requires at least one seed central EM trigger-tower with $E_T^{EM} > 8$ GeV and $E_{HAD}/E_{EM} < 0.125$ (for $E_T^{EM} < 14$ GeV), and an XFT track pointing to the seed tower with $p_T > 8$ GeV.

- **Level 2:** L2_CEM16_PT8. This requires at least one central Level 2 EM cluster with $E_T > 16$ GeV and $E_{HAD}/E_{EM} < 0.125$, and an XFT track pointing to the cluster with $p_T > 8$ GeV.

- **Level 3:** L3_ELECTRON_CENTRAL_18. This requires at least one central electron candidate with $E_T^{EM} > 18$ GeV and $E_{HAD}/E_{EM} < 0.125$ (for $E_{EM} < 100$ GeV) and $p_T > 9$ GeV.

2 Processing/Stripping

The Level 3 trigger dataset for high-p_T electrons described above is identified as `bhel08`, which uses the offline version 4.8.4 to perform reconstruction. In order to reduce the size of these datasets the events are filtered into a smaller dataset, `btop0g`. At least one electron passing loose requirements (Table 1) is required in each event. This reduces the overall electron sample by 25 %. The stripped datasets are further processed with a newer offline release 4.11.1 to pick up improved calorimeter corrections (see section 5.1) and the tracks are refitted to take advantage of the improved beamlines (see [13] for details).

Variables	Cut values (for EM $E_T < 70$ GeV)	Cut Values (for EM $E_T > 70$ GeV)
E_T^{EM}	> 18 GeV	> 18 GeV
E_{had}/E_{em}	< 0.125	no cut
E/P	< 4.0 (or $P_T > 9$ GeV)	$P_T > 15$ GeV
Lshr	< 0.3	no cut
$\|\Delta x\|$	< 3.0 cm	$<$3.0 cm
$\|\Delta z\|$	< 5.0 cm	< 5.0 cm
Region	central (CEM)	central (CEM)

Table 1: Stripping Cuts

3 Good Run List

All runs used in this analysis are required to satisfy a minimal set of requirements:

- At least 10 nb^{-1}
- Data Type = 1 (Beam)
- Run Type = 1 (Physics)
- Trigger table name is ”PHYSICS*” with no ”*TEST*”
- Require Run Control Good Run Bit = 1
- Require Offline Good Run Bit = 1
- Require Analysis Run Bit = 1

Runs 141544 to 150143 are required to have:

- CLC, L1, L2, L3, CAL, CMU, CMP, and SMX online bits set to one.
- CAL, COT, CMU, and CMP offline bits set to one.

Runs 150145 to 156487 are required to have

- CLC, L1, L2, L3, CAL, CMU, CMP, CMX, and SMX online bits set to one.
- CAL, COT, CMU, CMP, and CMX offline bits set to one.

Exceptions to these rules are noted here [14].

4 Luminosity

We find the luminosity for this dataset by adding the relevant offline Data File Catalog (DFC) entries for these runs using the method described in [15].
The total integrated luminosity is 72.0 ± 4.3 **pb**$^{-1}$.
The luminosity is calculated using the formula:

$$\mathcal{L} = \frac{R_{p\bar{p}}}{\sigma_{in}\epsilon_{clc}},$$

where $R_{p\bar{p}}$ is the rate of the inelastic $p\bar{p}$ events measured with the luminosity monitor (CLC) [16], ϵ_{clc} is the CLC acceptance and σ_{in} is the $p\bar{p}$ inelastic cross section. We have used $\sigma_{in} =$ 61.7 mb at $\sqrt{s} = 1.96$ TeV for the luminosity estimation [17]. The 6.0% quoted uncertainty is dominated by the uncertainty in the absolute normalization of the CLC acceptance (ϵ_{CLC}) for a single $p\bar{p}$ inelastic collision and by the the inelastic cross section, each contributing an uncertainty of $\sim 4\%$. We have also applied a +1.9% correction to the luminosity which comes from extrapolating the inelastic cross section from $\sqrt{s} = 1.80$ TeV to $\sqrt{s} = 1.96$ TeV as described in [17].

5 Corrections

5.1 Calorimeter Corrections

Corrections to CEM and PEM response are applied from the database. In offline version 4.11.1 the following corrections are implemented and are applied during clustering [18]:

- Corrections for tower-to-tower gain variations.
- Corrections for time-dependent gain changes.

For the CEM the time-dependent corrections are extracted by Larry Nodulman from plots of $\langle E/p \rangle$ as a function of time, and include an overall scale correction to bring the peak of the di-electron invariant mass to 91 GeV. Figure 1 demonstrates that the CEM corrections are made properly. For the PEM the time-dependent corrections are extracted from laser calibration and source data.

In addition, face corrections are applied at the ntuple level to data and simulation via standard routines in `CemCorrAlg` and `PemCorrAlg`, to correct for response dependence on local x and z coordinates (extracted from test-beam data) [19].

Despite these corrections a 7% variation is observed in data for $\langle E/p \rangle$ as a function of the local x position (CES-x). In order to make a flat distribution of $\langle E/p \rangle$ versus CES-x the following correction factor is applied to the CEM energy:

$$f_x = \frac{1.015}{(1 + 0.000157 \times x^2)}, \tag{2}$$

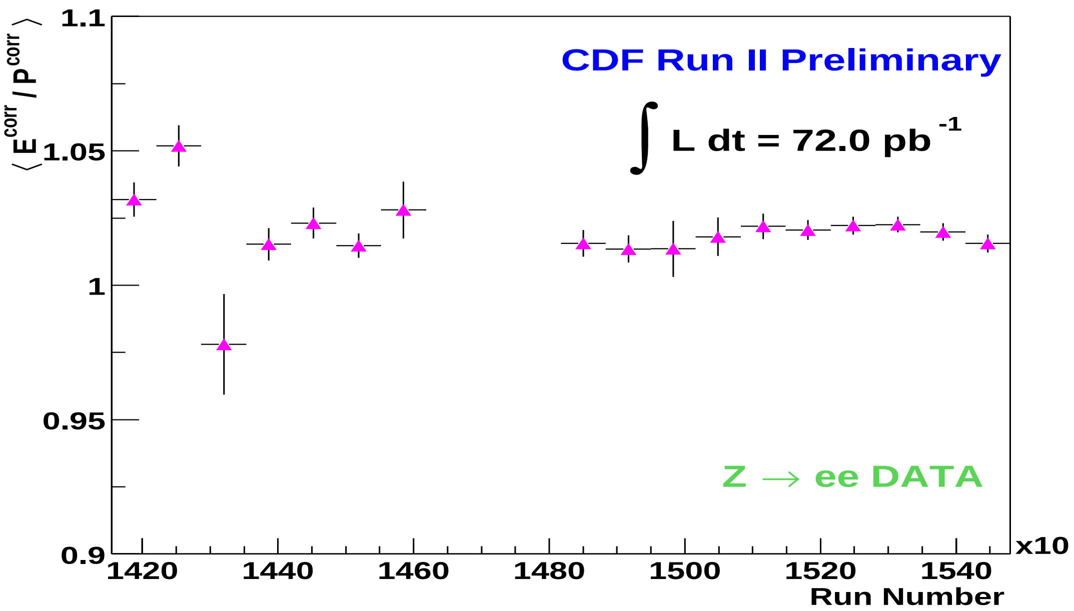

Figure 1: $\langle E/p \rangle$ *as a function of run number. The average of* E/p *is calculated in the range between 0.9 and 1.1.*

where x is measured by the CES. The corrected CEM energy is then $E_{corr} = f_x \times E$. The correction factor and the corrected $\langle E/p \rangle$ as a function of CES-x are shown in Figure 2.

The isolation variable in the calorimeter is corrected for leakage to the neighbor calorimeter towers [20].

5.2 Beam-constained Tracking/Curvature Corrections

Beam-constrained tracking and "COT-only" tracks are used in all studies presented in this document. The beam constrained tracking code is located in the TrackingMods package. Some details on how to use this code can be found in [21].

When using beam-constrained tracking we introduce a curvature bias. We correct the p_T of the COT beam constrained track as described in [22] and [23].

5.3 Missing E_T Calculation

By default, the electron transverse missing energy ($\not{E}_T$) is calculated assuming the interaction point is located at z = 0.0 cm. We correct the $\not{E}_T$ using the z_0 of the electron track as the event interaction point. In Run I it was shown ([24]) that using z_0 is a better measure of the event vertex than the primary vertex returned by the jet vertex algorithm, in case of $W \to e\nu$ and $Z^0 \to e^+e^-$ events.

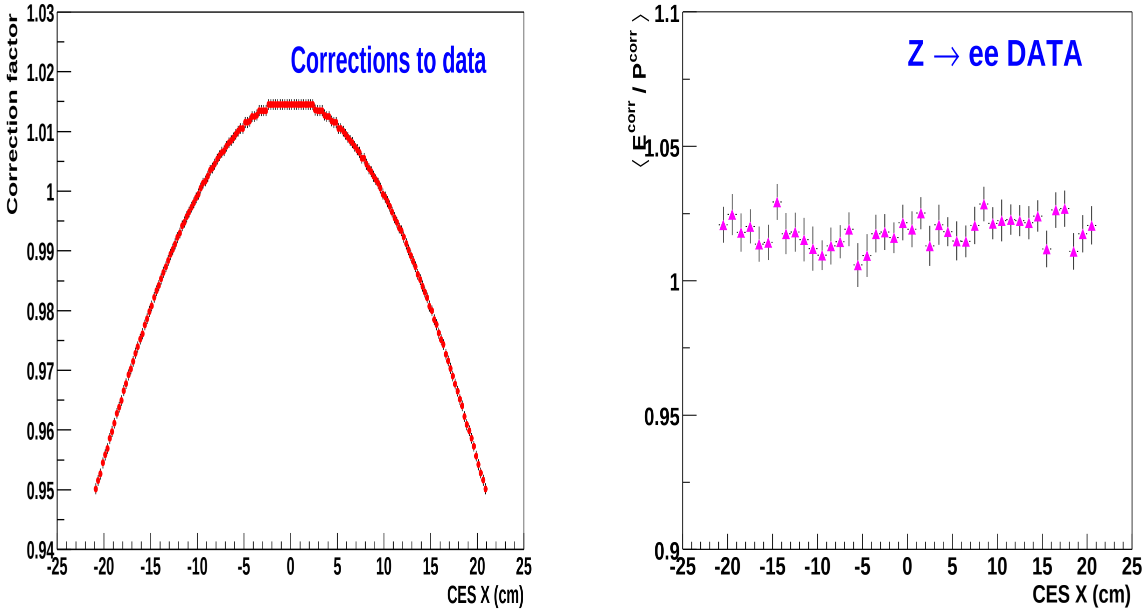

Figure 2: *The CEM energy correction factor applied to the data (left) and $\langle E/p \rangle$ as a function of CES-x after the corrections (right). The average of E/p is calculated in the range between 0.9 and 1.1.*

Part III

Monte Carlo

Monte Carlo samples are used to estimate the detector acceptance and background contributions to W production. The Monte Carlo samples are generated with PYTHIA 6.203[25], using CTEQ 5L[26] Parton Distribution Functions. The PYTHIA Monte Carlo generates W bosons at leading order(LO) with the p_T parametrized to match the data.

A full detector simulation is used to model the behavior of the CDF detector. The Monte Carlo samples used for this analysis are:

1.) A sample of 2M $W^{\pm} \rightarrow e^{\pm}\nu$ events (corresponding to the dataset identifier `wewk9e`), used for the detector acceptance studies;

2.) Four samples of $W^{\pm} \rightarrow e^{\pm}\nu$ events, of 1M events each (dataset identifiers `wewk3e`, `wewk4e` and `wewkae`, `wewk6e`), generated and simulated with exactly the same procedure as above, but with additional extra material in the central and plug regions, respectively. In the central it consists of a thick copper cylinder corresponding to a ± 1.5% X_0 placed between the beam-line and the COT inner radius, while in the plug it is a iron plate, corresponding to a ± 1/6 of X_0. The chosen values correspond to a $\pm 1\sigma$ variation with respect to the amount of material used in the default sample, described in section 7. These samples will be used for studying the systematic uncertainties on the acceptance of $W \to e\nu$ events;

3.) A sample of 500,000 $\mathrm{Z}^0/\gamma^* \to \mathrm{e}^+\mathrm{e}^-$ events (`zewk1e`), with minimum invariant mass of the dielectrons of 30 GeV;

4.) A sample of 500,000 $\mathrm{W}^\pm \to \tau^\pm\nu$ events (dataset identifier `wewk1t`), used for the background studies;

5.) A sample of 500,000 $\mathrm{Z}^0/\gamma^* \to \tau^+\tau^-$ events (`zewk1t`), where the τ decays generically, used for background studies;

6.) Four samples of $\mathrm{Z}^0/\gamma^* \to \mathrm{e}^+\mathrm{e}^-$ events, of 1M events each (dataset identifiers `zewk3e`, `zewk4e` and `zewk7e`, `zewk8e`), generated and simulated with exactly the same procedure as in **3.)**, with additional extra material in the central and plug regions, respectively. Again, they correspond to a $\pm 1\sigma$ variation with respect to the amount of material used in the default sample, described in section 7. These samples will be used for studying the systematic uncertainties on the acceptance of $Z^0 \to e^+e^-$ events;

No restrictions are placed at generation level on the transverse momentum of the final state leptons and on their pseudorapidity. Initial and final state radiation are turned on, as are multiple interactions and fragmentation and decay. In order to generate Monte Carlo which models the data, the beam energy used was set to 980 GeV, and the vertex parameters are set to a mean of 3 cm in z, and a Gaussian spread of 25 cm, to reflect what is observed in the data.

6 PYTHIA/Parameters

The acceptance for Drell-Yan dilepton pairs is obtained using the Monte Carlo event generator PYTHIA [25], and CDF detector simulation programs. PYTHIA generates the hard, leading order (LO) QCD interaction, $q + \bar{q} \to \gamma^*/Z$ (or $q + \bar{q}' \to W$), simulates initial state QCD radiation via its parton shower algorithms, and generates the decay, $\gamma^*/Z \to l^+l^-$ (or $W \to l\nu$). The CTEQ5L [27] nucleon parton distribution functions (PDFs) are used in the QCD calculations. The intermediate vector-boson p_{T} is tuned to CDF's Run 1 measurement of the fully corrected $d\sigma/dp_{\mathrm{T}}$ of ee pairs in the mass region $66 < M_{ee} < 116$ GeV [28]. PYTHIA's nonperturbative "K_{T} smearing" parameters, (PARP(91) and PARP(93)), and shower evolution Q^2 parameters, (PARP(62) and PARP(64)), are used in the tuning. The PARP(91) parameter affects the location of the "peak" in the $d\sigma/dp_{\mathrm{T}}$ distribution around 3 GeV, and the PARP(62) and PARP(64) parameters for the shape of the p_{T} distribution in the 7 – 25 GeV region. The "tuned" γ^*/Z p_{T} distribution is shown in Fig. 3.

The shape of the rapidity distribution of the intermediate vector boson is set by the choice of PDFs. The $d\sigma/dy$ distribution for ee pairs in the mass region, $66 < M_{ee} < 116$,

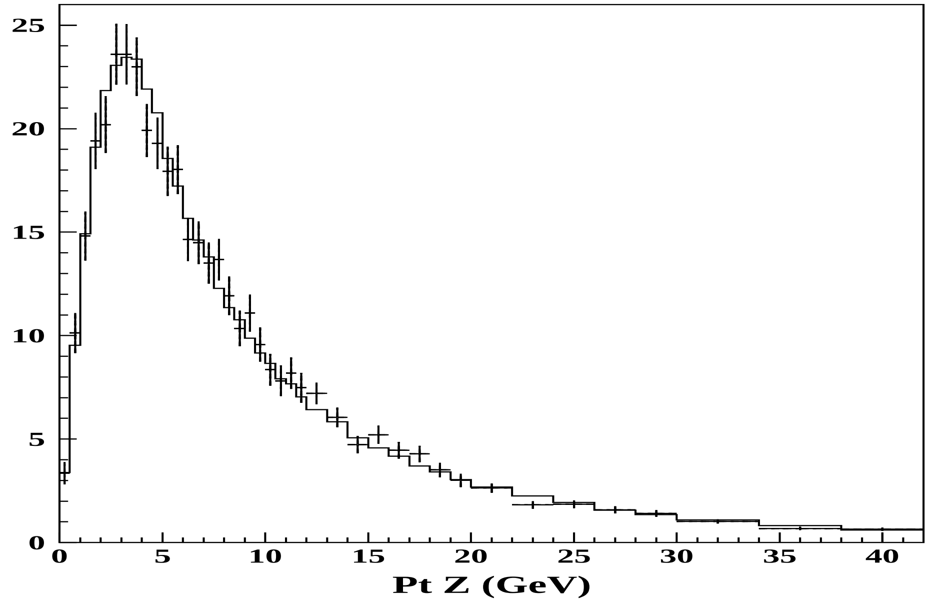

Figure 3: *Tuned PYTHIA 6.21* $d\sigma/dp_{\mathrm{T}}$ *of ee pairs in the mass region* $66 < M_{ee} < 116$ *vs* p_{T}. *The Run 1 measurement is the crosses, and the histogram, PYTHIA. The* y *axis is* $d\sigma/dp_{\mathrm{T}}$, *in pb per GeV/c.*

has been measured in Run 1[29]. The comparison between the PYTHIA 6.21 y distribution and the Run 1 measurement of $d\sigma/dy$ is shown in Fig. 4.

7 Material Description

The description of the material in the tracking volume reflects our best understanding of the detector from technical drawings, notes, material spreadsheets and knowledge of the experts. The default material description is described in [30] along with its implementation in the CDF simulation.

Because of its sensitivity to radiation, the E/p distribution is used the estimate the amount of material in the central tracking volume. The ratio of the number of events in the peak ($0.9 < E/p < 1.1$) to the number of events in the tail of the distribution ($1.5 < E/p < 2.0$) is a measure of the amount of material the electrons have passed through. We add a cylinder of silicon in between the silicon detecter and the COT. By varying the thickness of the cylinder, the simulation can be made to match the data. Using both Z and W electrons, we find that a cylinder of about 4.5 % radiation lengths (X_o) of silicon is required in the simulation so that the E/p distribution matches the data. We cross check

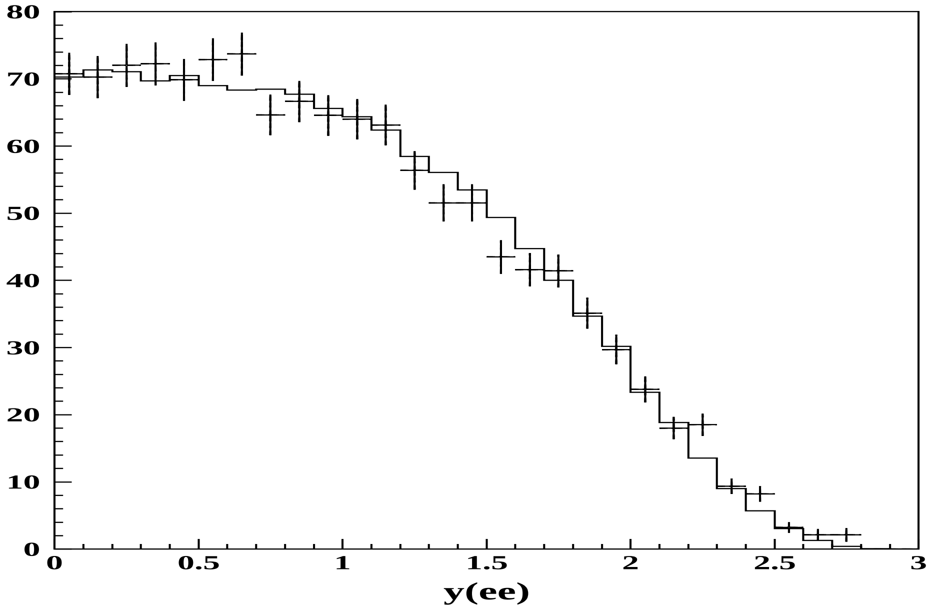

Figure 4: *Tuned PYTHIA 6.21 $d\sigma/dy$ of ee pairs in the mass region* $66 < M_{ee} < 116$ *vs y, the boson rapidity. The Run 1 measurement is the crosses, and the histogram, PYTHIA. The abscissa is $d\sigma/dy$, in pb.*

this result by counting the fraction of electrons with tridents in W events, and by looking at the Z track mass which is also sensitive to radiation effects. A summary of the studies is shown in Figure 5. The results fall in the range of 4–6 $\%X_o$ of silicon. The results of studies for W's in the $E/p > 2.5$ region are biased by dijet background contaminating the high E/p tail, and are ignored. We have also studied the effect of using different materials, and we have found that using materials with smaller X_o, such as lead and copper, push the estimate lower. There is reason to believe that the missing material is copper cables due to the apparent lack of material around R=15 cm from conversion studies and for consistency with muon energy loss studies. As a conservative estimate we use $(4.5 \pm 1.5)\%X_o$ of copper as the amount of material to add to the simulation to best reproduce the data. A more detailed description of the material estimation from electrons can be found in [31].

The plug preradiator detector is used to estimate the amount of material that plug electrons must pass through. The plug preradiator detector reads out the first scintillator panel of the plug calorimeter. The amount of energy deposited in the plug preradiator is dependent on the shower evolution of the electron at the front of the calorimeter. If the electron has passed through more material in front of the calorimeter, then the shower will be more evolved, and will subsequently deposit more energy in the plug preradiator. The ratio of the energy measured in the plug preradiator to the total energy measured by the

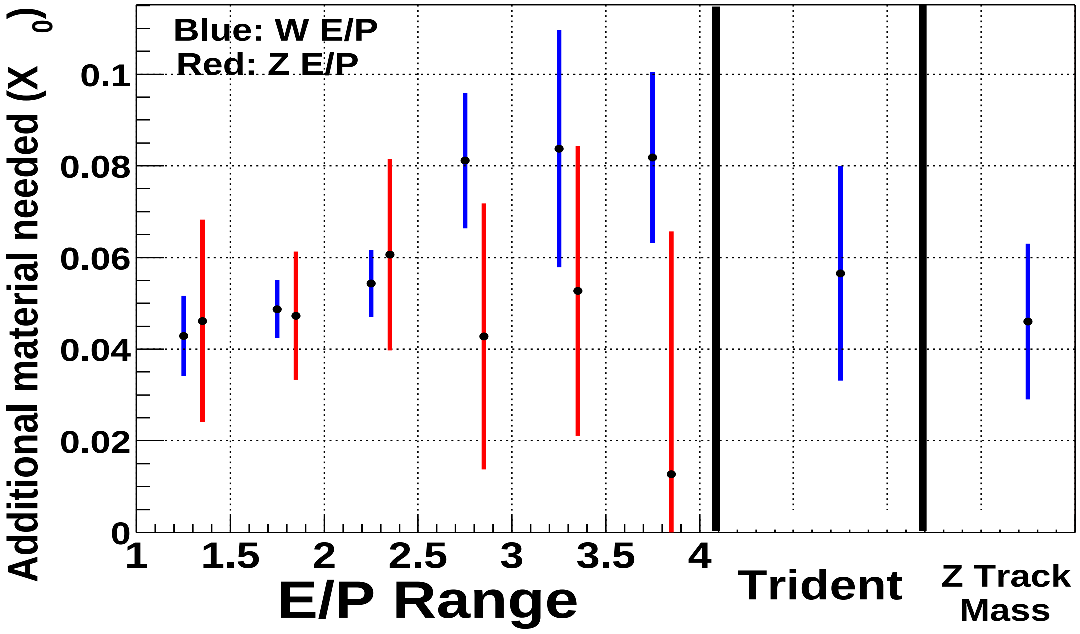

Figure 5: *Different estimates of the amount of additional material needed in the simulation so that it matches the data. Estimates from E/p use the ratio of the number of events in the peak (0.9–1.1) to the number of events in the tail in 0.5 increments (1.5–2, 2–2.5, etc.) The estimate from tridents compares the fraction of electrons in W events that are tridents in simulation and in the data. The Z track mass compares the ratio of events around the Z peak to the number of events in the tail between data and simulation.*

plug calorimeter is used to estimate the amount of material in front of the plug calorimeter. From this study we estimate that we need an additional $1/3 \pm 1/6 X_o$ thick steel disk in front of the plug calorimeter to reproduce what we see in the data.

Part IV

Event Selection

8 Electron identification variables

$Z^0 \rightarrow e^+e^-$ and $W \rightarrow e\nu$ events are selected using their signature of two isolated electrons or one isolated electron and missing energy, $\not\!\!E_T$. W electrons are required to be in the central region of the calorimeter. Z electrons are required to be either in the central (C) or

Variable	Cut
$\|\eta\|$	< 1.1 (CEM)
E_T	> 25 GeV
P_T	> 10 GeV
Iso Frac (Δ R = 0.4)	< 0.1
E_{had}/E_{em}	$< 0.055 + 0.00045 \cdot E$
E/P (or $P_T > 50$ GeV)	< 2.0
Lshr	< 0.2
Q $\cdot \Delta x$	-3.0, 1.5 cm
$\|\Delta z\|$	< 3.0 cm
χ^2_{strip}	< 10
$\|z_0\|$	< 60.0 cm
# Stereo SL	≥ 3 with ≥ 7 hits
# Axial SL	≥ 3 with ≥ 7 hits
`fidEle`	1 (fiducial in CEM)

Table 2: Criteria used in the selection of the tight central electron common to the W and Z samples.

in the plug (P). In this note we describe only the CC Z analysis. The CP analysis and the combination of CC+CP Z's are described elsewhere [32; 33].

The central electron identification cuts are described in [34] and [35] and summarized in Table 2. The variables used for the selection of the central electrons in the event are described in the following.

- E_T : The transverse electromagnetic energy deposited by the electron in the CEM is calculated as the electromagnetic cluster energy multiplied by sin (θ), where θ is the polar angle provided by the best COT track pointing to the EM cluster. An electron cluster is made from a seed EM tower and at most one more shoulder tower in the same wedge, passing some well-defined requirements [36]. The maximum cluster size could have two towers in pseudorapidity ($\Delta\eta \approx 0.2$) and one tower in azimuth ($\Delta\phi \approx 0.13$ *rad*)

- p_T : The transverse momentum of the beam-constrained COT track as measured using the track curvature in the COT in the magnetic field.

- Isolation:

  The energy in a cone of radius $\Delta R = \sqrt{\Delta\eta^2 + \Delta\phi^2} \leq 0.4$ around the electron cluster excluding the electron cluster divided by the energy in the electron cluster. We correct the isolation variable for calorimeter leakage (see [37] and [20]).

- E_{had}/E_{em} :

  The ratio of the hadronic (CHA+WHA) calorimeter energy to the electromagnetic (CEM) calorimeter energy for a cluster.

- E/P :

  The ratio of the EM cluster transverse energy to the COT track transverse momentum.

- L_{shr} :

  The lateral shower profile for electrons. This variable compares the energy in CEM towers adjacent to the seed tower for data and test beam electrons [38].

- Q * Δx :

  The distance in the r-ϕ plane between the extrapolated beam-constrained COT track and the best matching CES cluster, times the charge of the track.

- Δz :

  The distance in the r-z plane between the extrapolated beam-constrained COT track and the best matching CES cluster.

- χ^2_{strip}:

  The χ^2 comparison of the CES shower profile in the r-z view with the same profile extracted from test beam electrons.

- z_0 :

  The z coordinate of the track intersection with the beam axis in the r-z plane.

- Track quality cuts:

  The electron associated track must have passed through 3 axial and 3 stereo superlayers (SL), with at least 7 hits out of 12 in each of these SLs.

- Fiduciality:

  This variable ensures that the electron is reconstructed in a region of the detector which is well instrumented. The electron position in the CEM is determined using either the value determined by the CES shower ("CES-based", corresponding to `fidEle=1`) or by the extrapolated track ("track-based", corresponding to `fidEle=4`), and it must satisfy the following requirements:
  –the electron must lie within 21 cm on the tower centre in the $r - \phi$ view in order for the shower to be fully contained in the active region; this corresponds to the cut $|X_{CES}| < 21$ cm, where X_{CES} is the local coordinate of the calorimeter tower;
  –it shouldn't be in the regions $|Z_{CES}| < 9$ cm, where the two halves of the central calorimeter meet, and $|Z_{CES}| > 230$ cm, which corresponds to the outer half of the last CEM tower (tower 9) and it is more subjected to the leakage into the hadronic

part of the calorimeter;
–it shouldn't be in the region immediately close to the point of penetration of the cryogenic connections to the solenoidal magnet (the "chimney"), which is un-instrumented, corresponding to $0.77 < \eta < 1.0$, $75^o < \phi < 90^o$ and $|Z_{CES}| > 193$ cm.

9 $W \rightarrow e\nu$ Sample Selection

$W \rightarrow e\nu$ events are selected requiring one tight isolated electron as described in table2, with the additional requirement of having $\not\!\!E_T > 25$ GeV. Using these criteria we find 37584 W candidates; an estimation of the background in this sample is discussed in Section V.

In Figure 6, which shows the distribution of E_T vs. $\not\!\!E_T$, we see the $W \rightarrow e\nu$ signal along the diagonal. Figure 7 shows the distribution of Isolation vs. $\not\!\!E_T$, where one can see the $W \rightarrow e\nu$ signal in the region of an isolated electron with large missing energy. Additionally, Figures 8 through 10 show the transverse mass (M_T), E_T and $\not\!\!E_T$ distributions for data (blue dots), Pythia signal Monte Carlo (red), QCD background (magenta), Pythia $Z^0 \rightarrow e^+e^-$ background Monte Carlo (green) and Pythia $W \rightarrow \tau\nu$ background Monte Carlo (cyan).

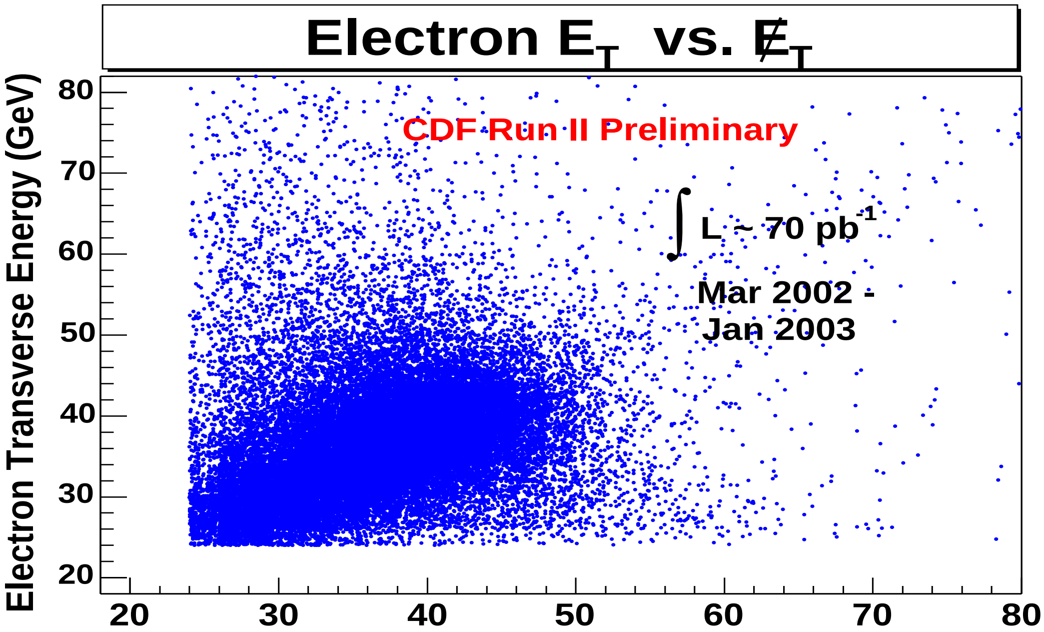

Figure 6: *Distribution of E_T vs. $\not\!\!E_T$. The $W \rightarrow e\nu$ signal is along the diagonal.*

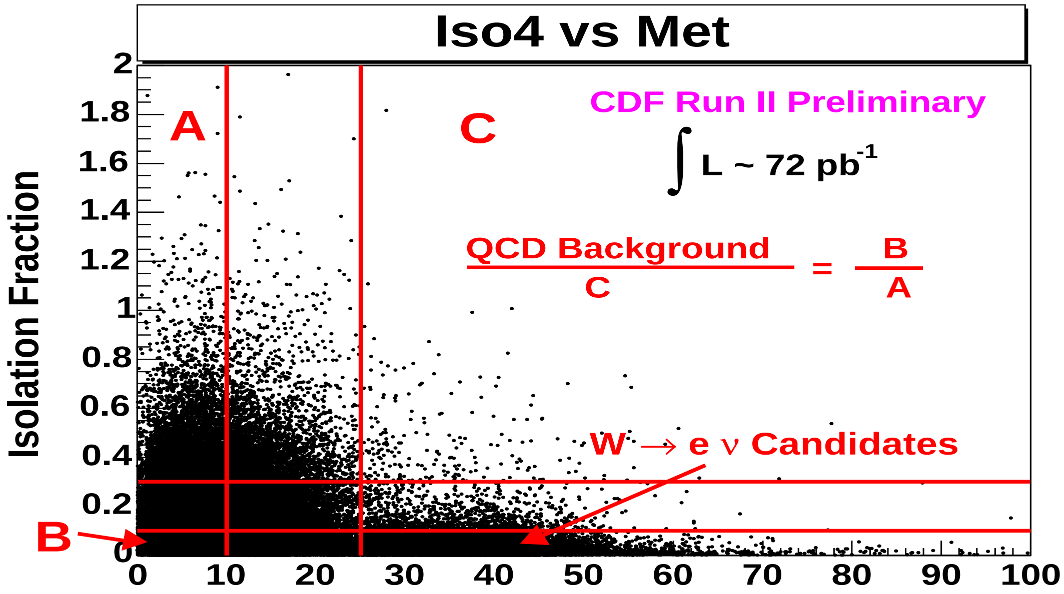

Figure 7: *Isolation Fraction vs.* $\not{E}_T$

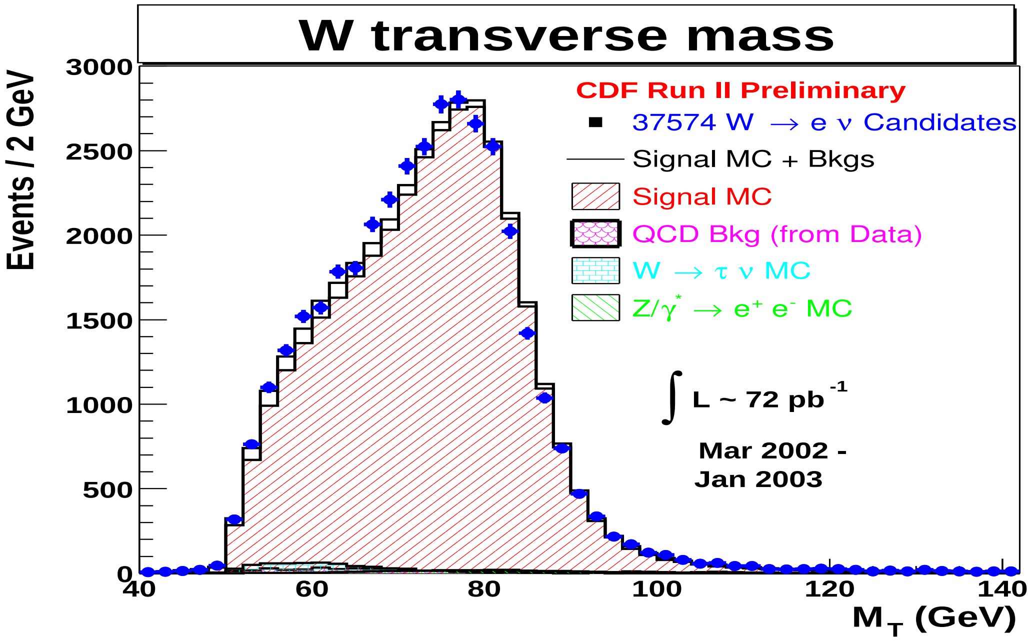

Figure 8: *Transverse Mass distribution for* $W \rightarrow e\nu$ *events. The data (blue dots), Pythia signal Monte Carlo (red), QCD background (magenta), Pythia* $Z^0 \rightarrow e^+e^-$ *background Monte Carlo (green) and Pythia* $W \rightarrow \tau\nu$ *background Monte Carlo (cyan) are shown.*

The signal MC histograms are normalized to the number of background-subtracted candidate events we observe in the data and the background histograms are normalized to the estimated background events (see section V). The shape of the QCD background is taken from non-isolated events in the data. For the $\not{E}_T$ plot, since we remove the $\not{E}_T$ cut to plot the distribution, we replace the isolation cut with an anti-isolation cut (> 0.3) to obtain the shape of the QCD background. Since the E_T and M_T plots are made after applying the $\not{E}_T$ cut, the number of QCD type events is very small after applying the anti-isolation cut. Hence, for these plots we remove a few of the electron ID cuts (Lshr, Δx, Δz, χ^2_{strip}), loosen the anti-isolation cut (> 0.1) and apply an anti-E_{had}/E_{em} cut to obtain the shape of the QCD background in these distributions. The agreement between the data, the Monte Carlos and the QCD background is reasonable.

In addition, Figure 11 shows the ϕ, η distributions of the $W \rightarrow e\nu$ candidate events. Figures 12 and 13 show the $N-1$ electron ID distributions of Lshr, E/P, E_{had}/E_{em}, Isolation, Δx, Δz and χ^2_{strip}; each distribution is shown after all identification cuts *except* the cut on the variable which is plotted.

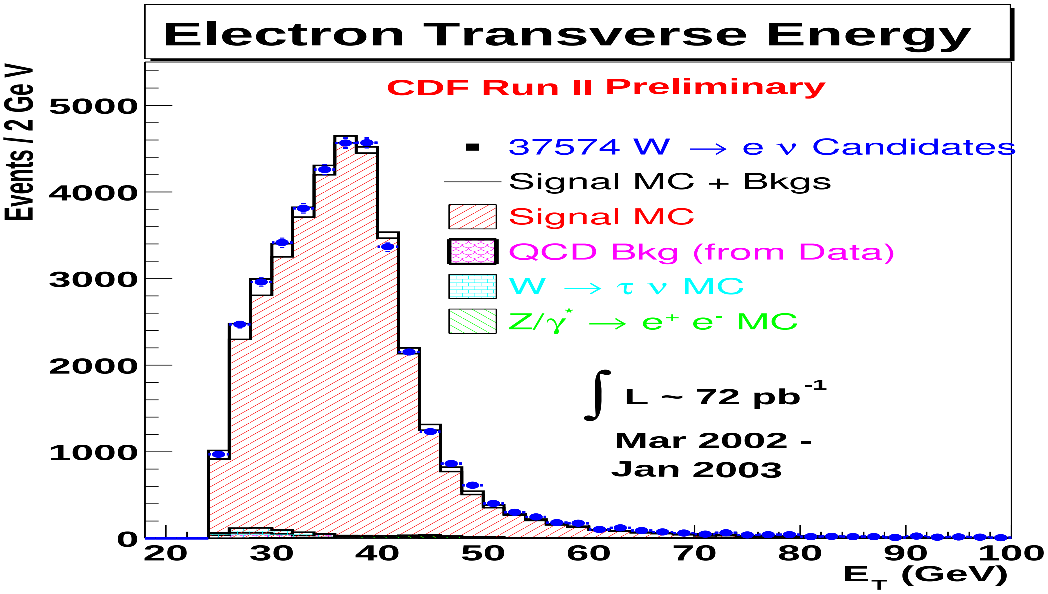

Figure 9: *E_T distribution for $W \rightarrow e\nu$ events. The data (blue dots), Pythia signal Monte Carlo (red), QCD background (magenta), Pythia $Z^0 \rightarrow e^+e^-$ background Monte Carlo (green) and Pythia $W \rightarrow \tau\nu$ background Monte Carlo (cyan) are shown.*

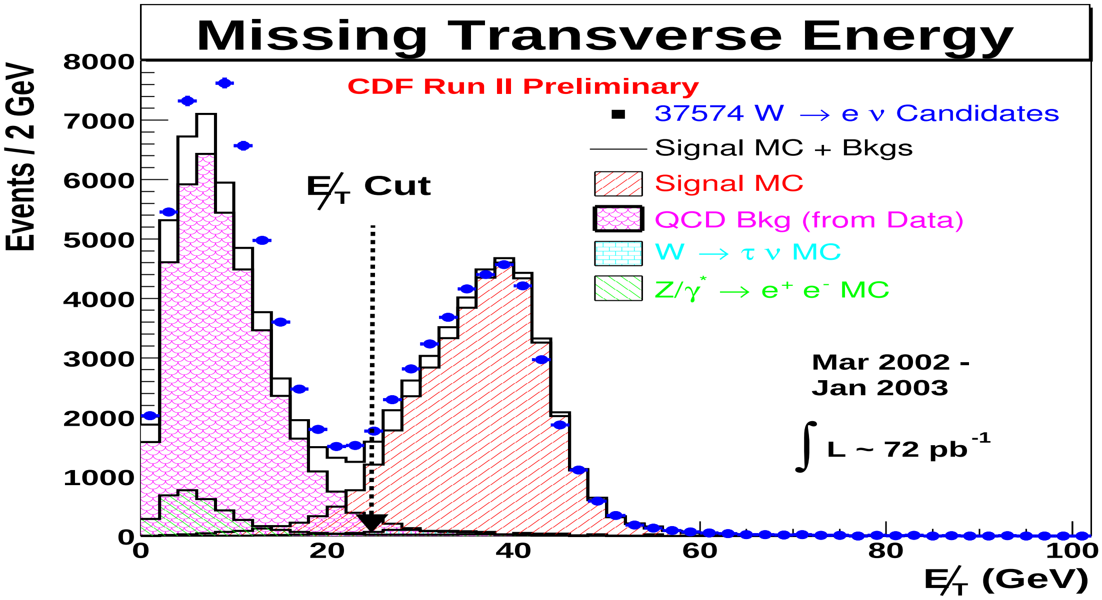

Figure 10: *$\not\!\!E_T$ distribution for $W \rightarrow e\nu$ events. The data (blue dots), Pythia signal Monte Carlo (red), QCD background (magenta), Pythia $Z^0 \rightarrow e^+e^-$ background Monte Carlo (green) and Pythia $W \rightarrow \tau\nu$ background Monte Carlo (cyan) are shown.*

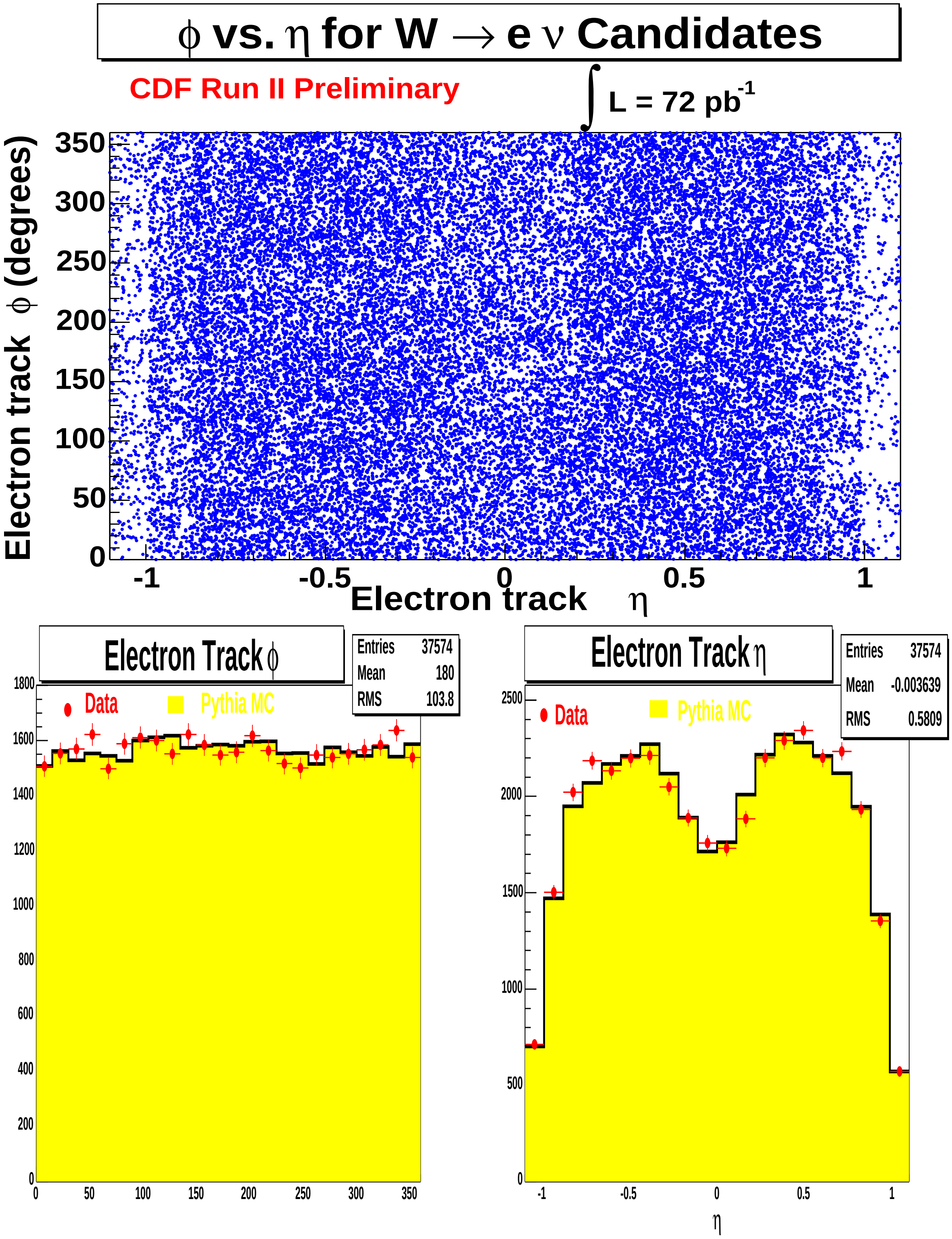

Figure 11: *φ and η distributions for $W \rightarrow e\nu$ candidate events.*

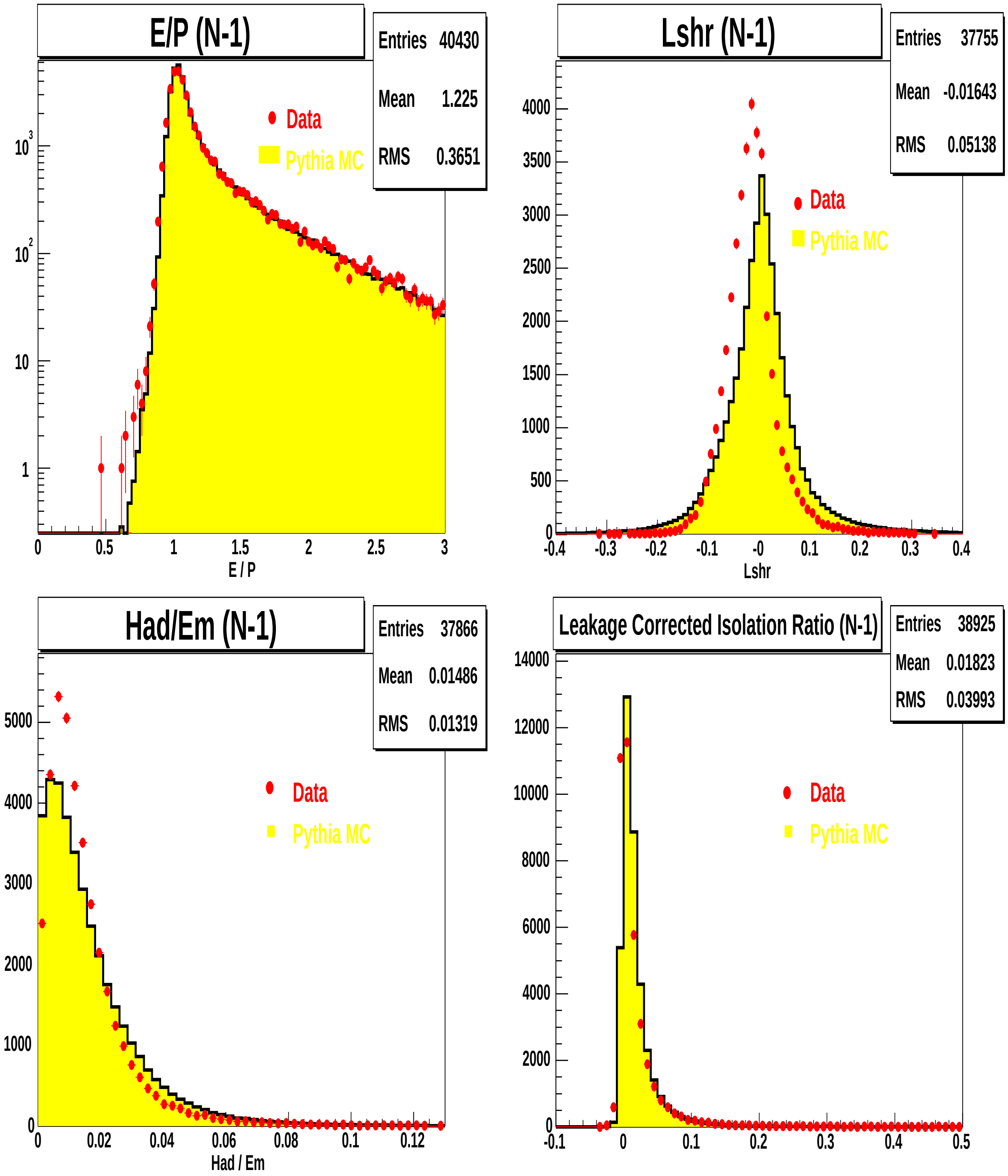

Figure 12: *$N - 1$ electron ID distributions of E/P, Lshr, E_{had}/E_{em}, Isolation for $W \to e\nu$ candidate events. Each distribution is shown after all identification cuts except the cut on the variable which is plotted. The dots represent the data and the histogram represents signal MC normalized to the data.*

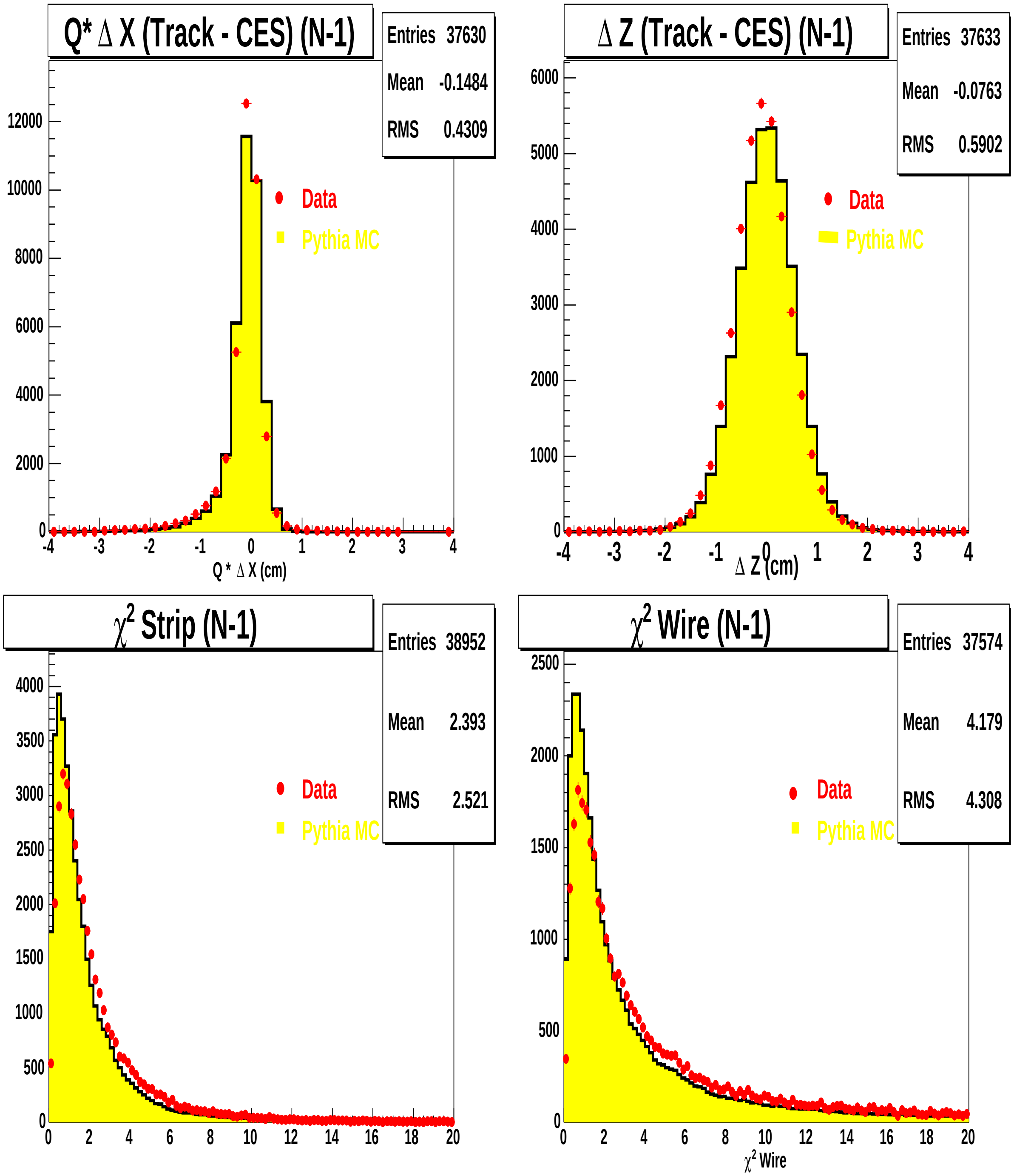

Figure 13: $N-1$ *electron ID distributions of* Δx, Δz, χ^2_{strip}, *and* χ^2_{wire}, *for* $W \to e\nu$ *candidate events. Each distribution is shown after all identification cuts except the cut on the variable which is plotted (the* χ^2_{wire} *plot is after all the cuts). The dots represent the data and the histogram represents signal MC normalized to the data.*

10 $Z^0 \rightarrow e^+e^-$ Sample Selection

$Z^0 \rightarrow e^+e^-$ events are selected starting from the tight central isolated electron sample, with a "tight" electron selection as described in Table 2, and also requiring the presence of another electron, the "loose" electron, satisfying the selection criteria listed in Table 3. The tight cuts on the first electron are sufficient to ensure the selection of Z events. Consequently, the criteria on the selection of the loose electron have been relaxed to purposely accept more signal. For more details about the efficiency of the tight and loose set of cuts see section 17. In this analysis only electrons falling in the central region of the detector have been used. Using these selection criteria we find 1730 $Z^0 \rightarrow e^+e^-$ candidates with opposite sign (OS) charge requirement and 22 with same sign (SS). The invariant mass distribution for these events is shown in Figure 14, for both OS and SS events in data and signal Monte Carlo. The good agreement in the mass peak location and width demonstrates that the CEM energy scale and resolution are in good shape for this analysis.

Variable	**Loose Central**
E_T	> 25 GeV
Fiduciality	CES based
Had/EM	$< 0.055 + 0.0045 \times E$
E_T^{iso}/E_T	< 0.1
p_T	$p_T >$10 GeV/c
Track Quality Cuts	at least 3 Axial and 3 Stereo SL with at least 7 hits each
Z_{vertex}	$\lvert z_0^{electron} \rvert <$60.0 cm
$66 < M_{\mathrm{ee}} < 116$ GeV/c^2	

Table 3: *Criteria for the selection of the loose electron candidate used in this analysis. The energy and momentum are corrected for data only. The central-central $Z^0 \rightarrow e^+e^-$ candidates require at least one tight electron and at least one loose electron in the invariant mass window between 66 and 116 GeV/c^2.*

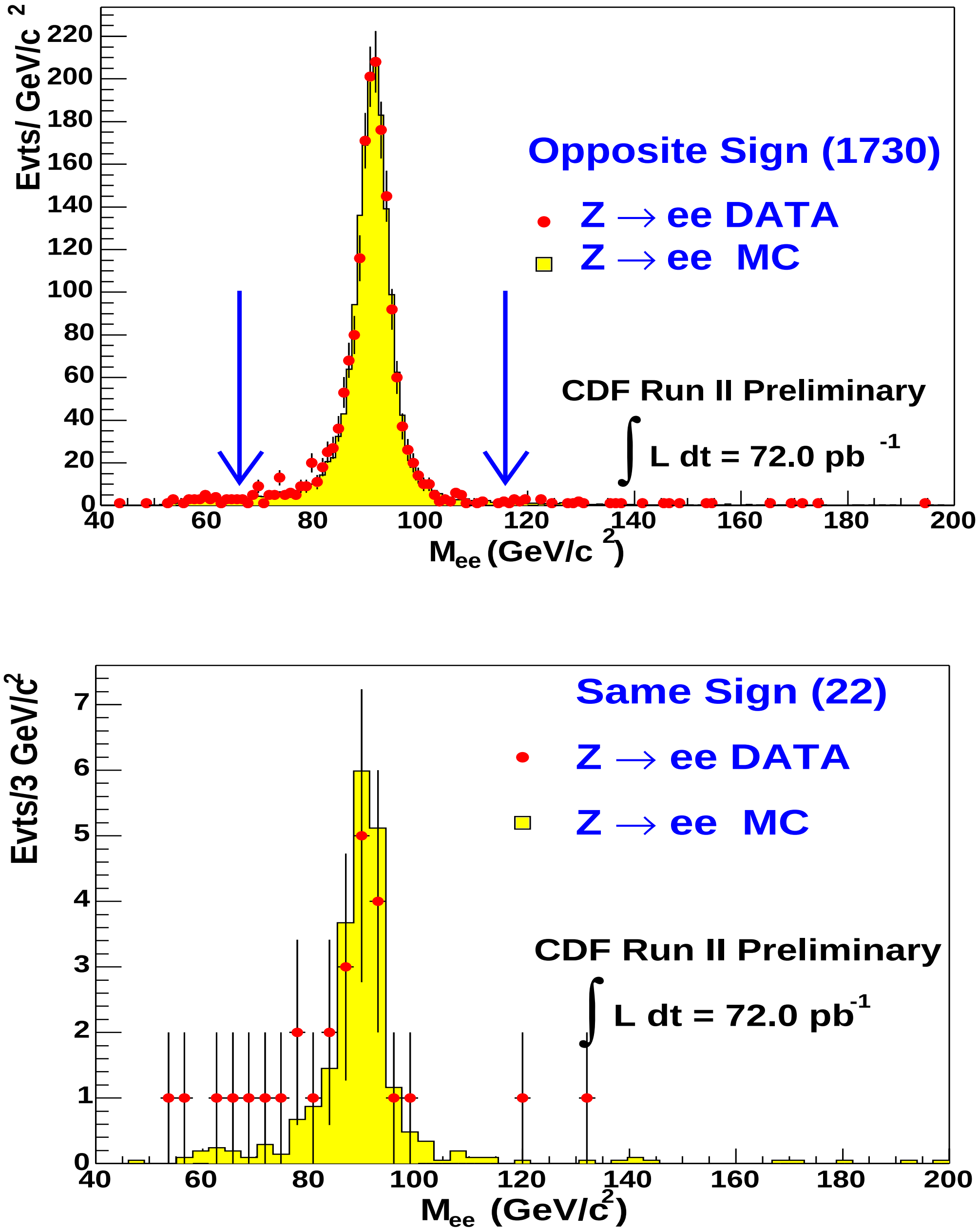

Figure 14: *The* $Z^0 \to e^+e^-$ *(CC) invariant mass distribution of data (dots) and* PYTHIA *Monte Carlo (solid histogram). The top plot shows the events with two electrons of opposite sign (OS), while the bottom plot shows the events where the electrons have the same sign (SS) electric charge. The number of events in the Monte Carlo sample has been normalized such that the number of OS events in the MC sample is equal to the number of OS events in the data. The arrows in the top plot indicate the invariant mass cut applied for this analysis.*

Estimation of the background in this sample is discussed in section V. The η and ϕ distributions for the candidate events are shown in Figure 15 (top),

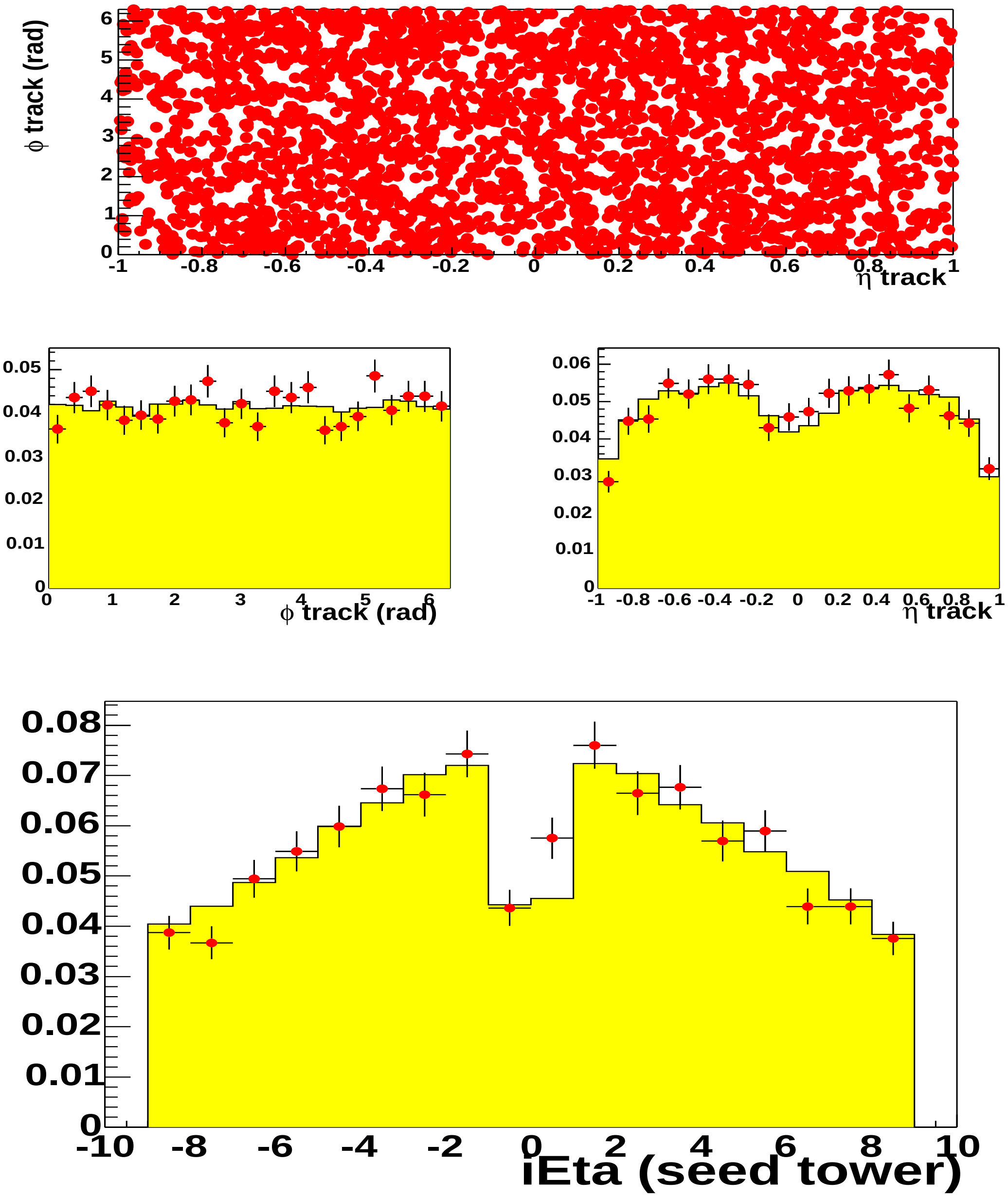

Figure 15: *The η and ϕ defined by the track associated with the tight and loose electrons for $Z^0 \to e^+e^-$ candidates (top and middle), and the distribution of the η tower index in the central region of the calorimeter for $Z^0 \to e^+e^-$ candidates. Points are data and histogram is the Monte Carlo simulation. It can be seen that the last tower, "tower 9", is excluded. The number of Monte Carlo events is normalized to the number of events in the data.*

while in Figure 15 (bottom) the value of the seed tower ("iEta") is shown. Also shown is the signal Monte Carlo, which is normalized to the number events in the data. In Figure 16, Figure 17 and Figure 18 the electron variables used for selecting the $Z^0 \to e^+e^-$ candidate events are compared with the signal Monte Carlo. The agreement is overall very good[1]. In

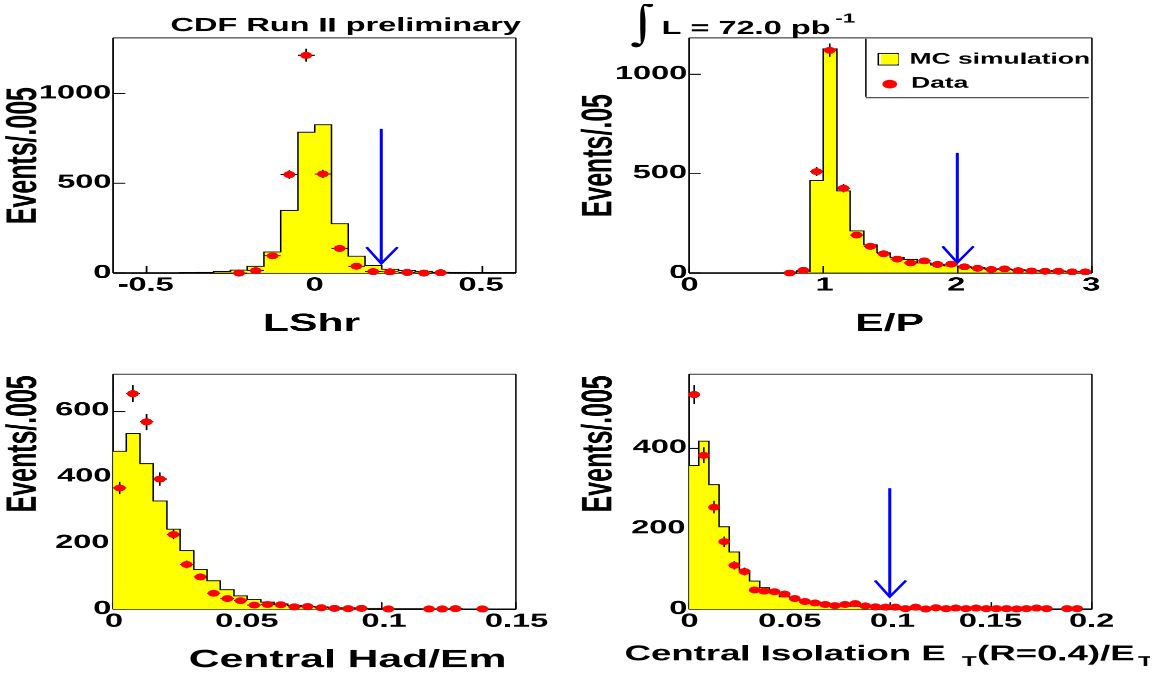

Figure 16: *The electron variables used for the selection of the events. The tight electrons in the $Z^0 \to e^+e^-$ candidates events (dots) and in the signal Monte Carlo (solid histogram) are used; for each variable all the selection criteria, but the one including the variable itself, are applied. The number of Monte Carlo events is normalized to the number of events in the data. The disagreement in the central bin of the Lshr distribution is due to a problem in the simulation which is understood and has been fixed in the newer versions.*

Figure 19 the CES local Z and X distributions are shown for Monte Carlo and data.

Part V

Backgrounds

Many physics processes can mimic the signature of Z and W events in the CDF detector, either because other objects are misidentified and mistakenly reconstructed as electrons, or

---

[1] The disagreement for the bin at zero in the Lshr distribution is due to a problem in the simulation and it has been fixed in the newer releases.

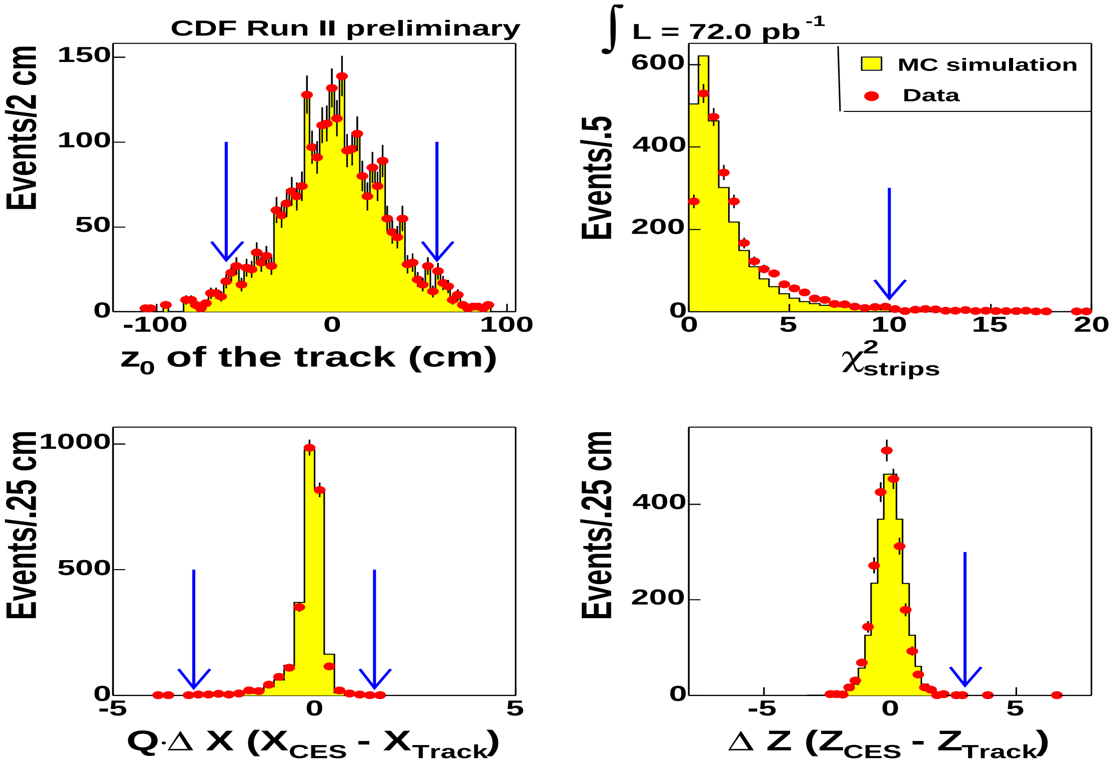

Figure 17: *The electron variables used for the selection of the events. The tight electrons in the* $Z^0 \rightarrow e^+e^-$ *candidates events (dots) and in the signal Monte Carlo (solid histogram) are used; for each variable all the selection criteria, but the one including the variable itself, are applied. The number of Monte Carlo events is normalized to the number of events in the data.*

because the event presents a similar topology. In this section the sources of backgrounds to real Z and W events are analysed, and the estimates for these backgrounds are given.

11 Backgrounds to the W events

The signature of a $W \rightarrow e\nu$ event can also be mimicked by other physics processes. The signature of $\not\!\!E_T$ is produced by jet mismeasurements and by particles incident on uninstrumented regions of the detector.

The backgrounds we consider here come from hadron jets, or QCD; $W \rightarrow \tau\nu$, where the τ decays leptonically; and from $Z \rightarrow ee$. We describe below the details of the estimations of the backgrounds in the W sample.

11.1 QCD Background

11.1.1 Standard Isolation vs. $\not\!\!E_T$ Method

The most challenging background to the $W \rightarrow e\nu$ signal to estimate is due to QCD processes. The sum of these backgrounds is estimated by extrapolating the number of background events from a region away from the W signal into the W signal region. This assumes that for the background there is no correlation between the isolation and $\not\!\!E_T$.

Figure 7 shows isolation fraction vs. $\not\!\!E_T$ for data. We define four regions in isolation fraction vs. $\not\!\!E_T$:

- Region A: isolation fraction > 0.3 and $\not\!\!E_T < 10$ GeV
- Region B: isolation fraction < 0.1 and $\not\!\!E_T < 10$ GeV
- Region C: isolation fraction > 0.3 and $\not\!\!E_T > 25$ GeV
- Region D: isolation fraction < 0.1 and $\not\!\!E_T > 25$ GeV

$$\frac{\text{QCD Background}}{\#\text{ Events in Region C}} = \frac{\#\text{ Events in Region B}}{\#\text{ Events in Region A}} \tag{3}$$

Region D is the $W \rightarrow e\nu$ signal region, while all the others, A, B and C, have mostly background. The background in region D (QCD background) is estimated from equation 3.

Using this technique, we estimate 1146 ± 78 (stat) events out of the 37,584 $W \rightarrow e\nu$ candidate events. However, in order to correctly extrapolate the background in the signal region from regions A, B, C, we should account for the fact that these regions also contain a contribution from the signal itself, as well as backgrounds from other processes, such as $W \rightarrow \tau\nu$ and $Z^0 \rightarrow e^+e^-$. The distributions of isolation fraction vs. $\not\!\!E_T$ for the signal, $W \rightarrow \tau\nu$ and $Z^0 \rightarrow e^+e^-$ are shown in figure 20. Correcting regions A, B, C for these processes we finally estimate the QCD background to be 587 ± 52 (stat) events.

In order to estimate the systematic uncertainty of the QCD background using this technique we vary the location of the upper isolation and lower $\not\!\!E_T$ cuts, since these values are arbitrary. Figure 21 shows the dependence of the values of the isolation fraction and $\not\!\!E_T$ cuts on the background estimate, before (red) and after (blue) correcting regions A, B, C for signal and electroweak processes. The background estimate seems to be independent of the location of the $\not\!\!E_T$ borders definition and highly dependent on the location of the isolation borders definition. Although, there is some evidence from a di-jet Monte Carlo sample that the remaining fluctuations are a feature of QCD ([39]), we still use the fluctuations from the plots of Figure 21 to estimate the systematic uncertainty of the QCD background using this method. This is estimated to be about 50 % or 294 events. Further support for the estimate of the systematic uncertainty is found in sections 11.1.2 and 11.1.3.

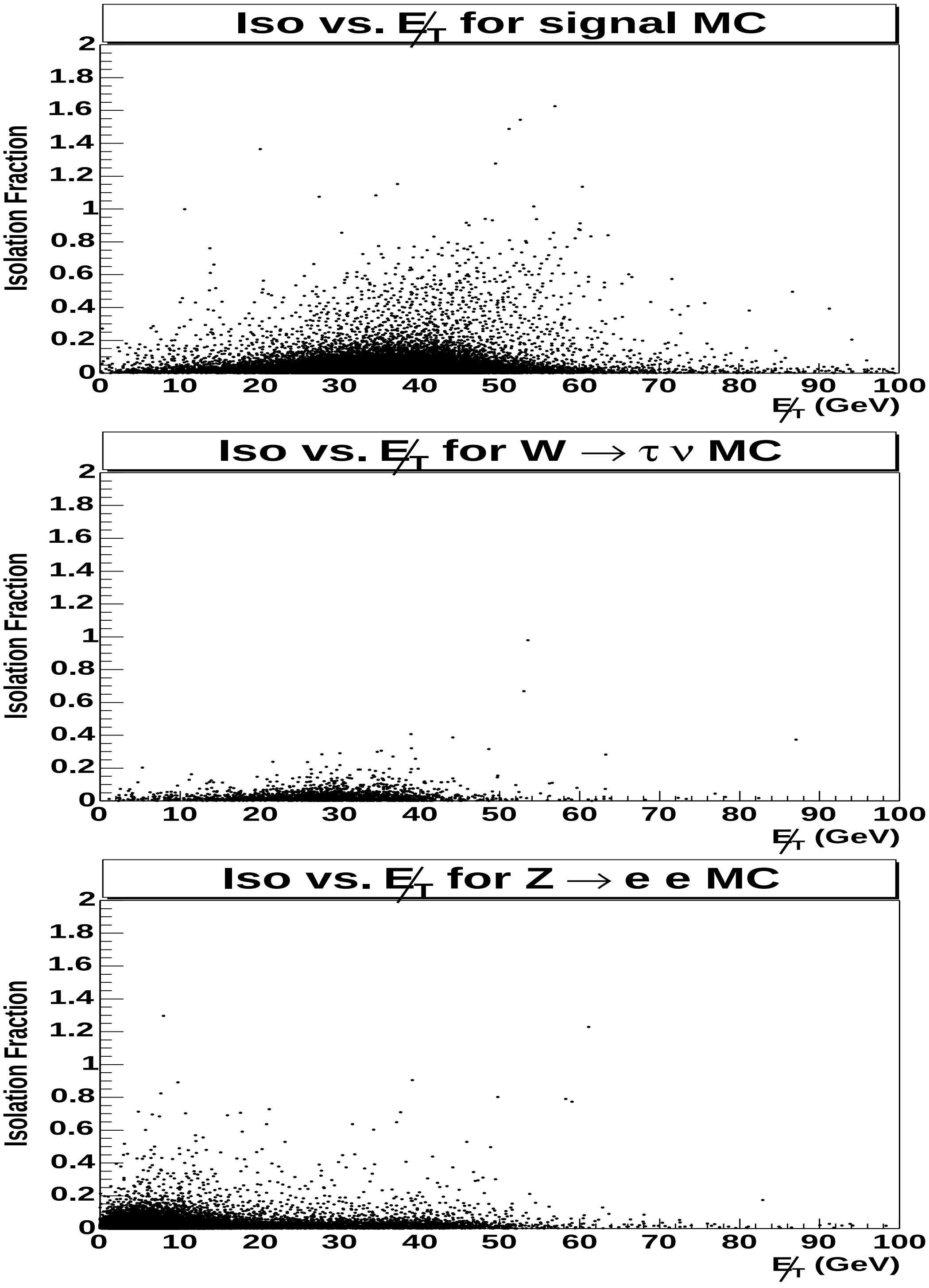

Figure 20: *isolation fraction vs.* $\not\!\!E_T$ *for signal,* $W \to \tau\nu$ *and* $Z^0 \to e^+e^-$ *Monte Carlo samples. We correct the regions A, B, C for these processes when estimating the QCD background using the isolation fraction vs.* $\not\!\!E_T$ *technique.*

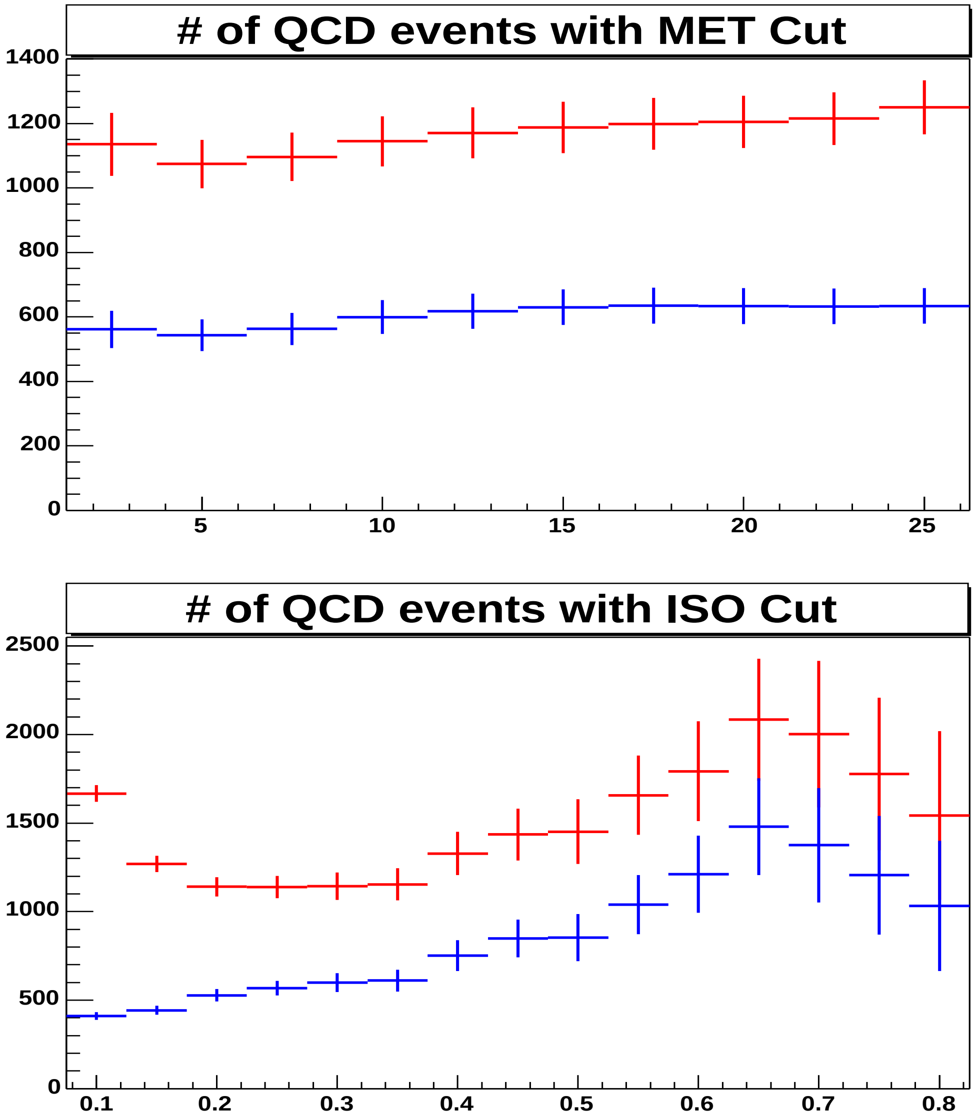

Figure 21: *QCD Background dependence on the isolation fraction and* $\not{E}_T$ *cut values which define the control regions. The nominal method, with no background subtraction, is shown in red and after correcting regions A, B, C for standard model processes is shown in blue.*

11.1.2 Fake Rate Method

An estimation of the QCD background to $W \to e\nu$ can be made using a fake-rate method and the jet sample. This provides an independent cross-check of the standard QCD background estimation method. The method is adapted from that used to estimate the QCD background in $Z \to ee$ events.

The fake rate is measured from events containing at least two jets with $E_T > 15\,\mathrm{GeV}$, $\not\!\!E_{\mathrm{T}} < 15\,\mathrm{GeV}$, and not more than one loose electron. These requirements ensure that contamination from W and Z electrons is negligible. The fake rate is defined as the fraction of jets with $E_T > 30\,\mathrm{GeV}$ that pass the standard tight-electron cuts.

The E_T dependence of the fake rate is shown in Fig.22. Given that the energy summation for jets and electrons is so different, the lower E_T bins are not included in the fit. However a large error on the final background estimate is assigned, based on different methods for fitting this E_T dependence.

The $\not\!\!E_{\mathrm{T}}$ distribution is constructed for all jets, weighted by the fake rate, and is shown in Fig.22. A jet is included if its $E_T^{scaled} > 25\,\mathrm{GeV}$, where E_T^{scaled} is the jet E_T scaled down to the E_T of the electron it would fake.

The spectrum is integrated for $\not\!\!E_{\mathrm{T}} > 25$ to give the final background estimate, which is 800 ± 300 events.

11.1.3 Angular Correlation Method

One of the known failings of the standard I *vs.* $\not\!\!E_T$ method of estimating QCD backgrounds is that it assumes that the "sideband" regions (large I and small $\not\!\!E_T$) are purely QCD background. This is not the case – the fact that the isolation cut is not fully efficient tells us that there is contamination from the W signal in the sideband regions, and there are also contributions from non-QCD background processes such as $W \to \tau\nu$ and $Z \to \mu\mu$.

While we can model these effects with simulations, we can also use more data-driven methods. One is to make use of angular distributions to separate out QCD backgrounds from the W signal. The QCD background is mostly multijet events, dominated by dijets. In such an event, when a jet fakes a lepton, it will typically be seen recoiling against the other jets in the event. By contrast, for real W events, it is the W that recoils against the jets, and thus to a good approximation the lepton direction will be uncorrelated the jets in the event. We therefore construct the sum of the jet momenta (summing over all jets with $E_T > 8$ GeV and $|\eta| < 2.4$), and then the opening angle $\Delta\phi$ between that vector and the electron p_T direction. QCD backgrounds will tend to be back-to-back in $\Delta\phi$, while the W signal will be flat. This behavior has been verified in appropriate simulation samples [40].

This distribution is shown in our non-isolated-electron data sample in Figures 23, for events in which there is at least one jet. (We assume that the zero-jet events are free of QCD backgrounds.) Note that we have required that these events not have a jet within $|\Delta R| < 0.4$ of the electron; this eliminates real W plus jets events in which the lepton has unfortunately landed inside a jet. In the distributions, we can see the flat component from real W production and the peak at 180 degrees due to QCD backgrounds.

We can use this information to build a $\not\!\!E_T$ distributions in the non-isolated-lepton samples that are enriched in QCD events and thus are more like the distributions for QCD events in the isolated samples [40]. We select events with $\Delta\phi \geq 150$ degrees, and plot the $\not\!\!E_T$ spectrum for those events. There is still some W contamination in this sample. We correct for it by subtracting off the $\not\!\!E_T$ spectrum of events in the $42 < \Delta\phi \leq 120$ degrees. This subtraction is normalized on the assumption that the $\Delta\phi$ distribution is flat for W events, with a level that can be estimate from the events in the $42 < \Delta\phi \leq 120$ range. Figure 24 shows the raw $\not\!\!E_T$ distributions for events with $\Delta\phi \geq 150$ degrees (mostly QCD) and for events in the $42 < \Delta\phi \leq 120$ degrees range (mostly $W \rightarrow e\nu$). The spectrum from the events in the QCD region of $\Delta\phi$ have a softer $\not\!\!E_T$ distribution than those from the W region.

Finally, to get an estimate of the QCD background in the signal sample, we use this new $\not\!\!E_T$ distribution in the same way that we use the $\not\!\!E_T$ distribution from the non-isolated sample in the standard method. We assume that the small-$\not\!\!E_T$ events of the isolated sample are pure QCD, and we normalize the small-$\not\!\!E_T$ rate from our new distribution to the small-$\not\!\!E_T$ rate in the isolated sample. The resulting number of events in the signal region of $\not\!\!E_T$ gives us the estimated number of QCD events in our signal sample. We estimate a background of 594 ± 80 events in the electron sample, which is in good agreement with our prediction based on the standard $\not\!\!E_T$ versus isolation method. The uncertainty is based on counting statistics propagated through the estimate.

11.2 Background from $Z^0 \rightarrow e^+e^-$

$Z^0 \rightarrow e^+e^-$ events can also mimic the $W \rightarrow e\nu$ signal when one of the electrons falls into an uninstrumented region of the detector, creating missing energy.

To estimate this background, we generate 500K $Z/\gamma^* \rightarrow e^+e^-$ Pythia events with offline version 4.9.1 and apply all the W selection cuts (see table 2) to estimate the acceptance of this process faking our signal; 9263 events pass the cuts. We do the same for our signal MC events and find that $19.41 \pm 0.03(stat)\%$ of the signal MC events pass all the W selection cuts. Then, based on Standard Model assumptions about the relative production rates of our signal process and the two background processes, we utilize these acceptance values to predict the relative contribution from each process to the total number of events in our candidate sample.

The $Z^0 \rightarrow e^+e^-$ production cross section is related to $W \rightarrow e\nu$ through the ratio R defined in equation 4.

$$R = \frac{\sigma \cdot Br(W \rightarrow e\nu)}{\sigma \cdot Br(Z \rightarrow ee)} \tag{4}$$

In order to correct for this difference in the production cross sections, we utilize a NNLO theoretical calculation by Stirling that gives $R = 10.67 \pm 0.15$ at $\sqrt{s} = 1.96$ TeV. One additional piece of information available to us is the CDF Run I published result for R based on the W and Z boson electron decay channels. The measured value of $R = 10.90 \pm 0.43$ at $\sqrt{s} = 1.8$ TeV is in good agreement with the theoretical prediction (only a small difference is expected from the change in the center-of-mass energy). Although we choose to utilize the value of R based on the theoretical calculation, we add an additional systematic to account for the present level of uncertainty in the experimental measurement (3.9%). Our input value for R based on this conservative approach is shown in equation 5.

$$R = 10.67 \pm 0.15(theory) \pm 0.42(systematic) = 10.67 \pm 0.45 \tag{5}$$

So, using the assumptions above, we estimate the background to be:

$$N_Z = \frac{(N_{WC} - N_O - N_Z)}{R(W/Z)}, \tag{6}$$

which becomes:

$$N_Z = \frac{(N_{WC} - N_O)}{R(W/Z) + 1}, \tag{7}$$

where N_Z is the number of background events in our sample, N_{WC} is the number of $W \rightarrow e\nu$ candidate events, N_O is the number of all other background events (N_{QCD}, see section 11.1.1, and N_τ, see below) and *R(W/Z)* is the ratio of $W \rightarrow e\nu$ to $Z^0 \rightarrow e^+e^-$ cross-sections times acceptances. Since there is a dependence of this and other backgrounds, the method is an iterative process.

We estimate the background from this process to be 317 ± 14 events. The uncertainty is a combination of the statistical uncertainty (including Monte Carlo statistics) and the uncertainty on the ratio of cross sections cross sections.

11.3 Background from $W \rightarrow \tau\nu$

To estimate this background, we generated 500,000 $W \rightarrow \tau\nu$ Pythia MC events and again applied all the W selection cuts to estimate the acceptance of this process faking our signal; 2160 events pass the cuts. Then, assuming the $W \rightarrow \tau\nu$ and $W \rightarrow e\nu$ cross sections are equal:

$$\begin{aligned} N_{\tau \mathrm{background}} &= N_{\mathrm{realW's}}/R(e/\tau) \\ &= (N_{WC} - N_O - N_\tau)/R(e/\tau), \end{aligned} \tag{8}$$

where N_τ is the number of background events in our sample, N_{WC} is the number of $W \rightarrow e\nu$ candidate events, N_O is the number of all other background events (N_{QCD}, see section 11.1.1, and N_Z, calculated above) and $R(e/\tau)$ is the ratio of the $W \rightarrow e\nu$ to $W \rightarrow \tau\nu$ acceptances. This then becomes:

$$N_\tau = (N_{WC} - N_O)/(R(e/\tau) + 1). \tag{9}$$

We estimate that the background from this process is 752 ± 17 events. The uncertainty is a combination of the statistical uncertainty (including Monte Carlo statistics) and the uncertainty on the ratio of cross sections. Again, due to the nature of the method (dependence on other backgrounds) the final estimate is obtained after a few iterations.

11.4 Background Summary

The background estimates are summarized in Table 4.

Background Estimation	number out of 37,574 events
QCD	587 ± 299
$Z^0 \rightarrow e^+e^-$	317 ± 14
$W \rightarrow \tau\nu$	752 ± 17
Total	1656 ± 300

Table 4: Summary of backgrounds in W sample.

12 Backgrounds to the Z events

$Z^0 \rightarrow e^+e^-$ candidates present the very distinctive signature of an isolated, tight central electron and a second isolated electron, selected according to the criteria described in section 10 and Tables 2 and 3. Very few physics processes can mimic this signature, with the QCD quark-antiquark production being the dominant one. Smaller contributions come from the $Z^0/\gamma^* \rightarrow \tau^+\tau^-$ and W+jets processes. All of these constitute background to $Z^0 \rightarrow e^+e^-$ events and as such will be analysed in the following sections.

12.1 QCD Background

Processes which contain a real electron (such as a semi-leptonic decay of a quark or conversion of photons) or which can fake one (such as QCD jets or di-jets events) are included in the QCD background analysed in this section. As there is no reason for these kind of events to be preferentially positively or negatively charged, they are expected to be charge symmetric; that is, the number of opposite sign(OS) and same sign(SS) QCD background events should be the same[41]. Thus, it is possible to use the number of SS sign events to estimate the number of QCD background events in the OS sample.

In this analysis the number of events in the data that pass all the event selection criteria, but fail the opposite sign requirement, is first corrected for the number of real $Z^0 \rightarrow e^+e^-$ events (which can mimic SS events as discussed below) using the Monte Carlo predictions. The remaining number is then used as an estimate of the QCD background in the OS sample. The number of OS events in the data is 1730, and the number of SS sign events is 22; their invariant mass distributions are shown in Figure 14. The number of tracks pointing to the EM cluster and the difference in z_0 between the two electron tracks for the OS and SS samples are compared between the data and the simulation in Figure 25 and Figure 26.

As can be observed from the invariant mass distributions, both the Monte Carlo and the data same sign distributions show a peak around 91 GeV, the mass of the Z boson. The events in the peak are the so called “trident” events (an example of a trident event is given in Figure 27). They are $Z^0/\gamma^* \rightarrow e^+e^-$ events where one electron from the Z radiates a high E_T photon while passing through the material; the photon then converts into an electron and a positron in the material.

If the positron from the photon conversion is chosen as the track associated to the electron cluster, the two tracks will have the same sign charge. As these are real $Z^0/\gamma^* \rightarrow e^+e^-$ events, they should not be removed from the sample. In order to account for this effect, the number of SS events in the data is corrected subtracting the number of same sign events in the Monte Carlo (which gives an estimate of the number of tridents in the data), normalised to the number of OS events in the data. As already stated, there are 22 SS events in the di-electron data sample with invariant mass between 66 GeV and 116 GeV, and 20.4 scaled SS events are found in the $Z^0/\gamma^* \rightarrow e^+e^-$ Monte Carlo sample (see Figure 14 bottom). Thus, the QCD background is estimated to be $1.6 \pm 4.7(stat.)$, where the statistical uncertainty is on the number of SS events in the data. The invariant mass distribution of SS events, after the 20.4 Monte Carlo SS events are subtracted, is shown in Figure 28 (top).

The dominant source of systematic uncertainty on the QCD background is expected to come from the uncertainty on the amount of material between the beam-line and the COT inner cylinder, as this affects the probability that an electron emits a photon by bremsstrahlung. This effect has been studied using two *ad-hoc* samples with an extra $\pm 1\sigma$ X_0 of the material added to the default geometry database, as described in section III. Figure 29 shows the E/p distribution of electrons in the $Z^0/\gamma^* \rightarrow e^+e^-$ data compared with the default simulation (shaded histogram) and the simulation with the extra material (open histogram). The number of SS events in the mass region between 66 GeV/c^2 and 116 GeV/c^2 changes when the extra material is added (Figure 28 bottom). The difference between the value of SS events obtained with the default Monte Carlo and the largest of these two values is taken as a systematic uncertainty on the number of QCD background events in the OS $Z^0/\gamma^* \rightarrow e^+e^-$ sample. The QCD background is thus estimated to be $1.6 \pm 4.7(stat.) \pm 5.2(syst.) = 1.6 \pm 7.0$, where the total uncertainty is calculated by adding the statistical and systematic uncertainties in quadrature. More studies on the systematic uncertainty on the acceptance coming from the material are discussed in chapter VI.

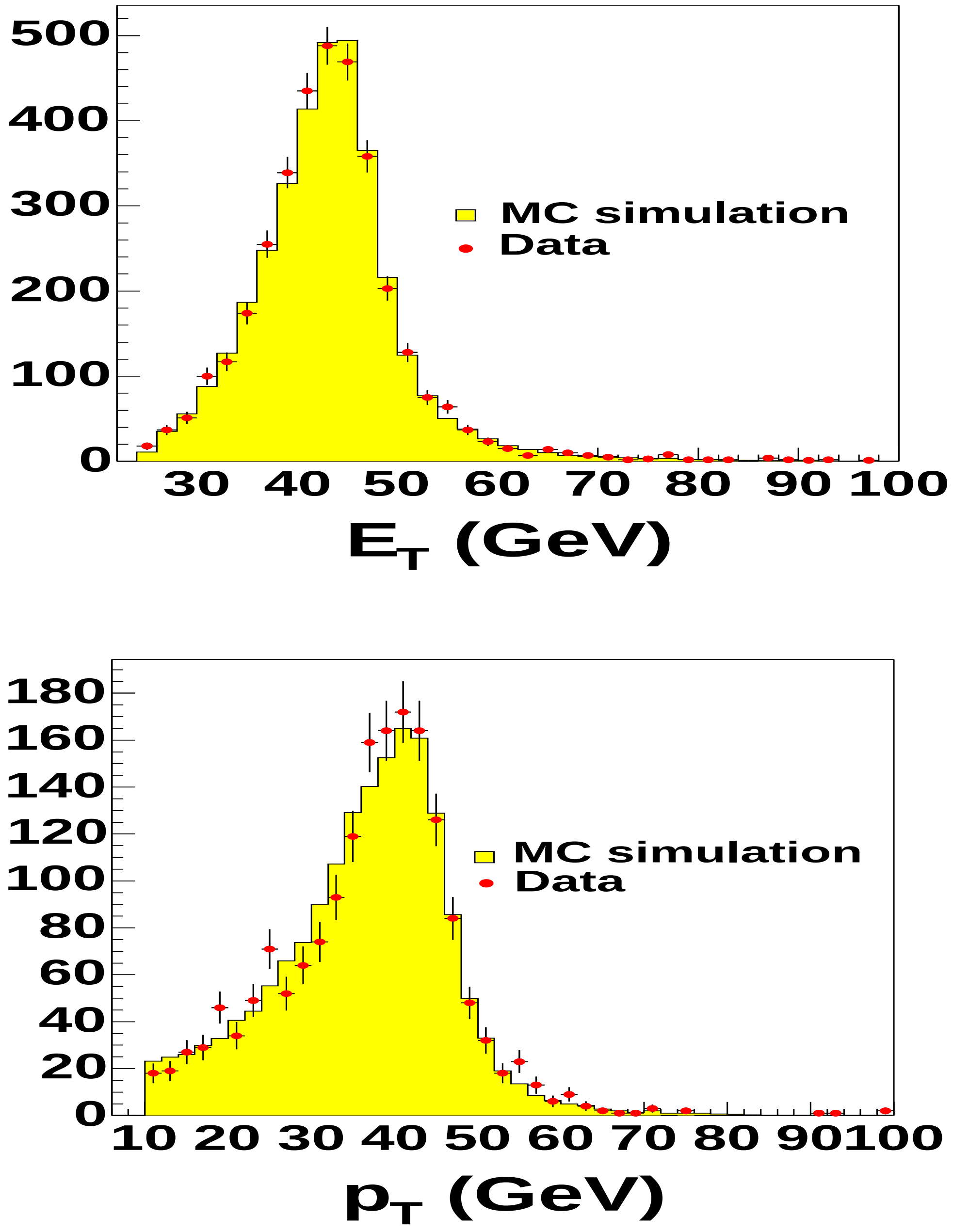

Figure 18: *Distribution of E_T and p_T for the tight electrons from $Z^0 \rightarrow e^+e^-$ candidate events.*

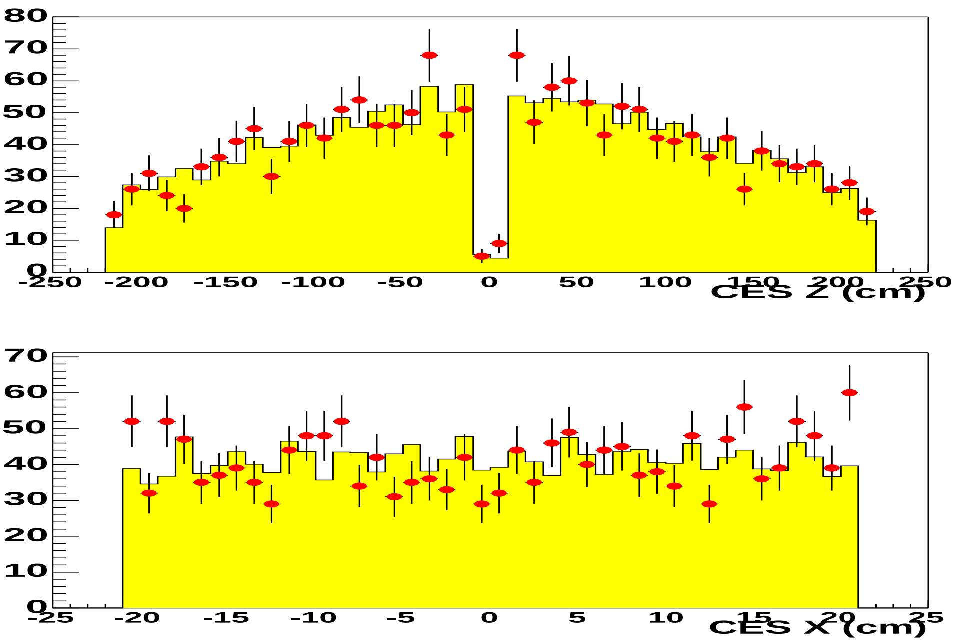

Figure 19: *The CES local Z and X distributions for* $Z^0 \rightarrow e^+e^-$ *candidates (dots) and signal Monte Carlo (solid histogram). The number of Monte Carlo events is normalized to the number of events in the data.*

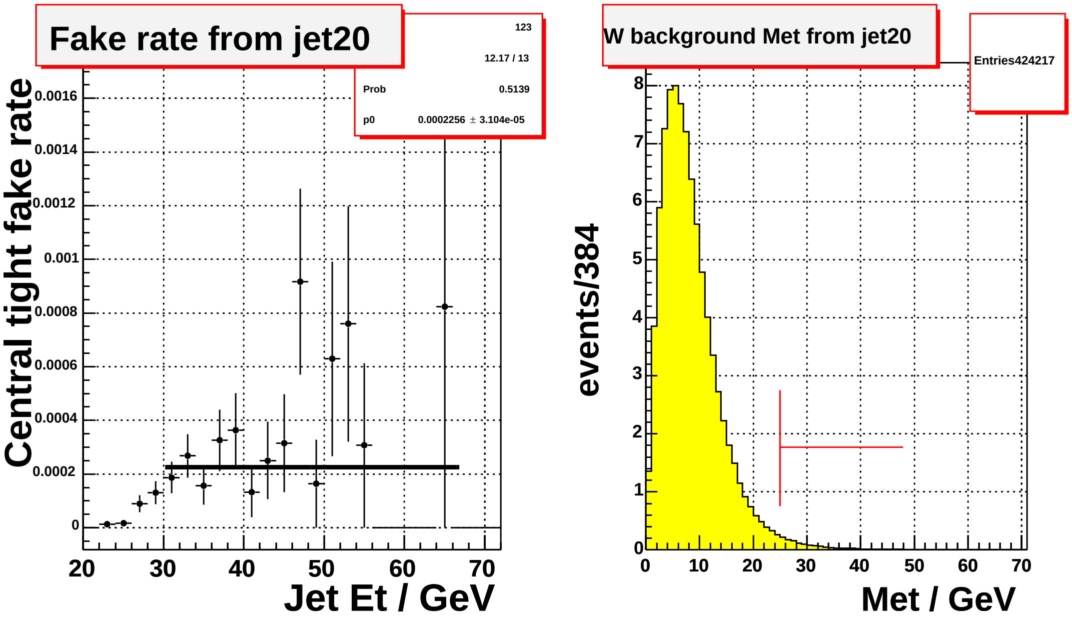

Figure 22: *Central electron fake rate from jet 20 (left), with an example fit.* $\not\!\!E_T$ *distribution for fakes (right).*

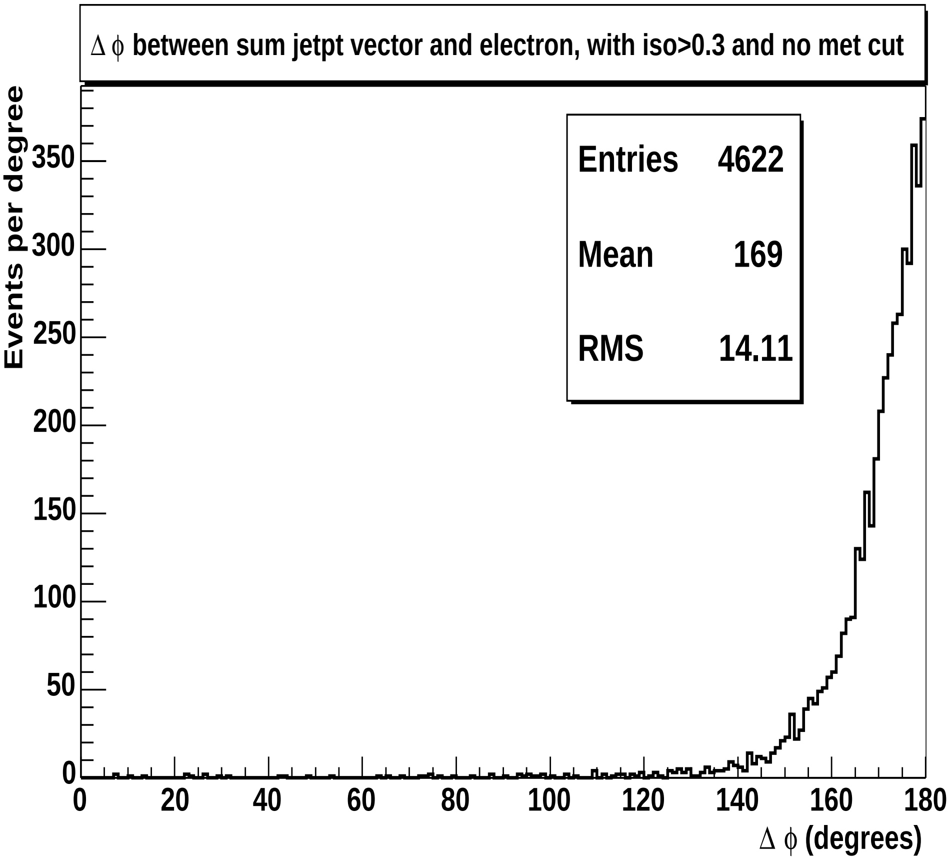

Figure 23: *Distribution of* $\Delta\phi$ *between the sum of the jet momenta and the electron* p_T *in* $W \rightarrow e\nu$ *candidate events (no* $\not\!\!E_T$ *cut) containing a non-isolated electron (isolation fraction ¿ 0.3) and at least one reconstructed jet. Events are required to have no jet within* $|\Delta R| < 0.4$ *of the electron.*

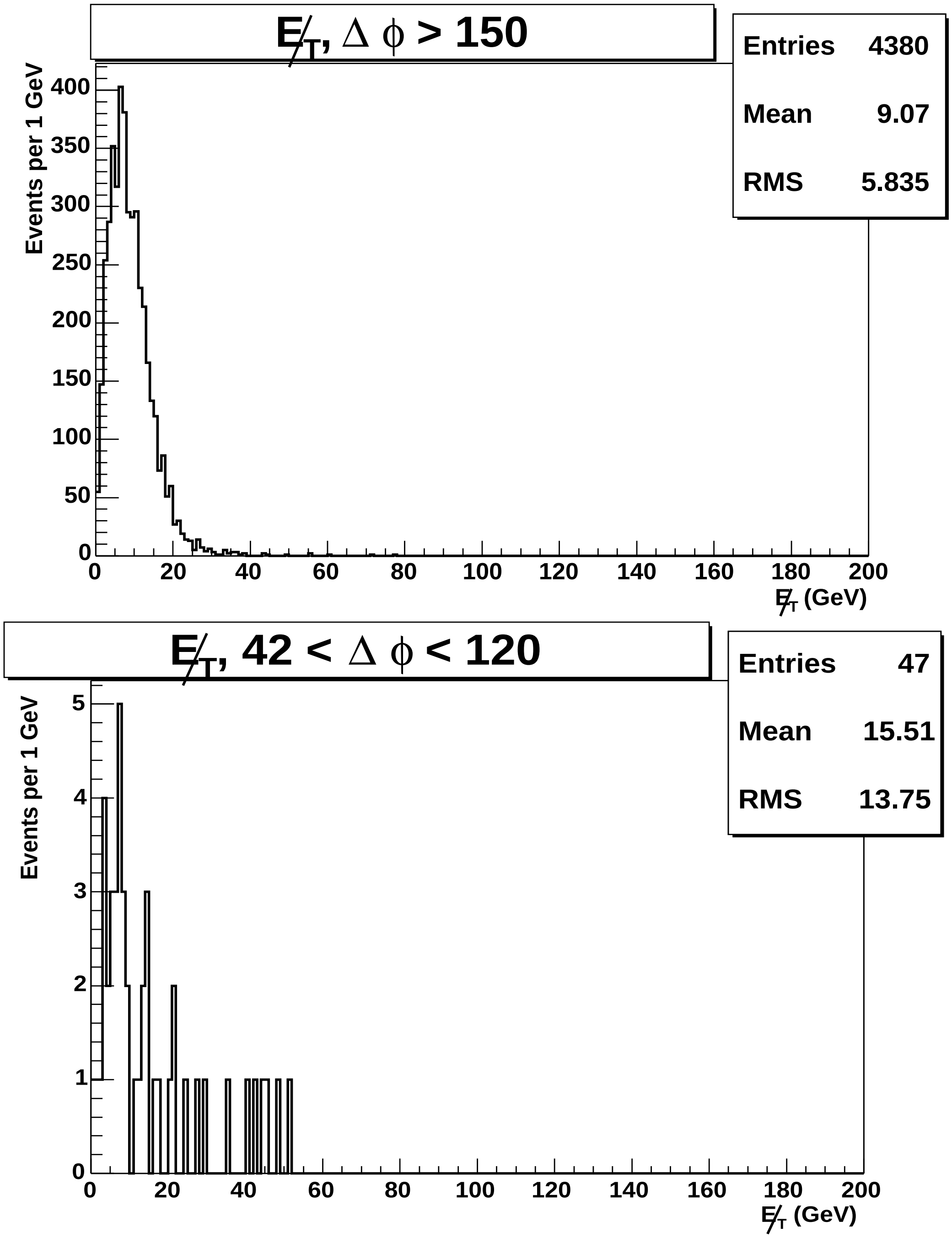

Figure 24: $\not\!\!E_T$ *Distributions for non-isolated* $W \to e\nu$ *candidates where* $\Delta\phi$ *between the sum of the jet momenta and the electron* p_T *is* ≥ 150 *degrees (top) and in the range* $42 < \Delta\phi \leq 120$ *degrees (bottom).*

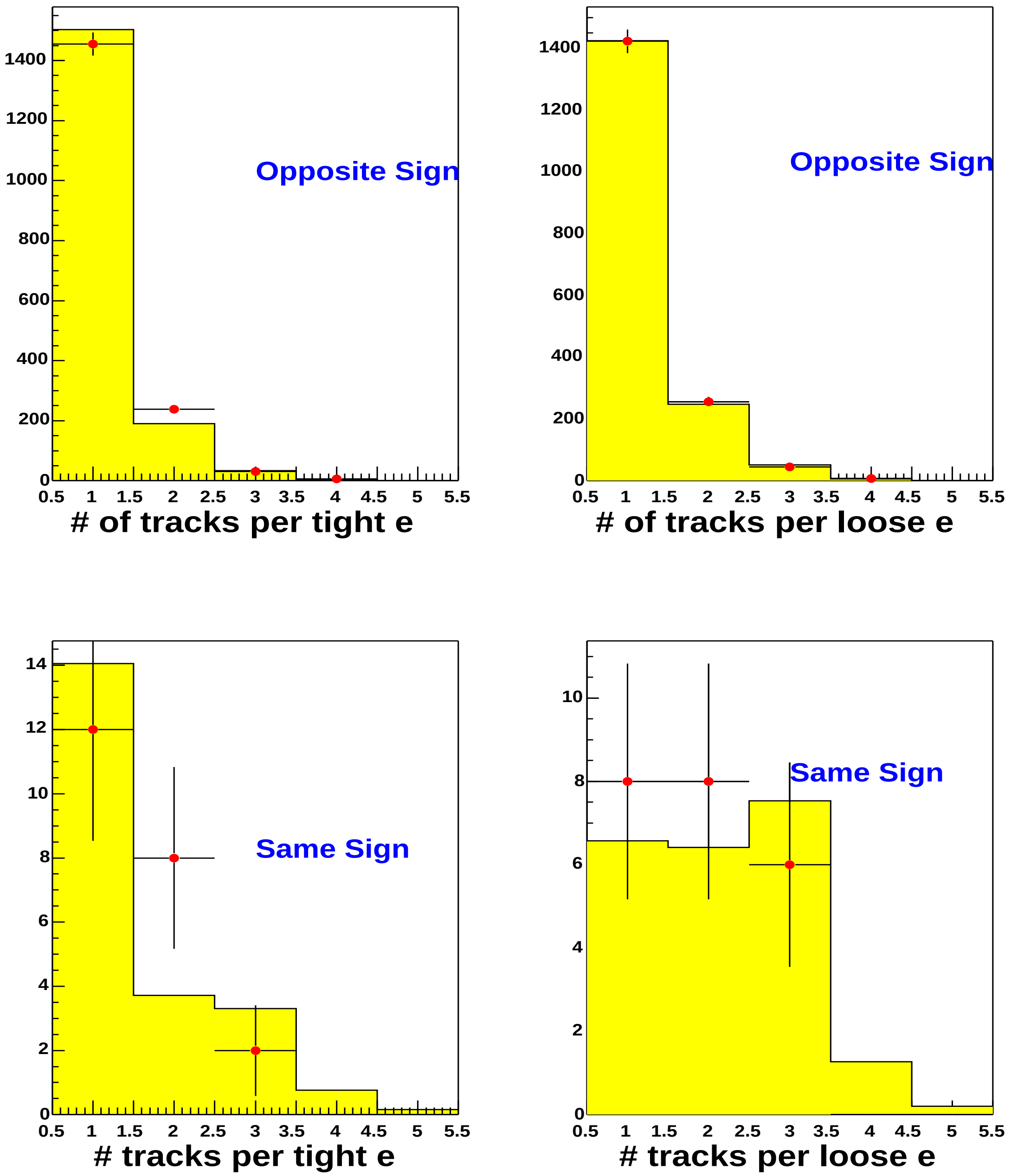

Figure 25: *The number of tracks pointing to electron clusters for the OS events (two left plots) and for the SS events (two right plots). The points are* $Z^0/\gamma^* \to e^+e^-$ *candidates and the histograms are* $Z^0/\gamma^* \to e^+e^-$ *Monte Carlo events; the number of events in the Monte Carlo is normalised to the number of opposite sign events in the data. The presence of clusters with two or three tracks associated with it in the SS sample is due to trident events, as described later in the text.*

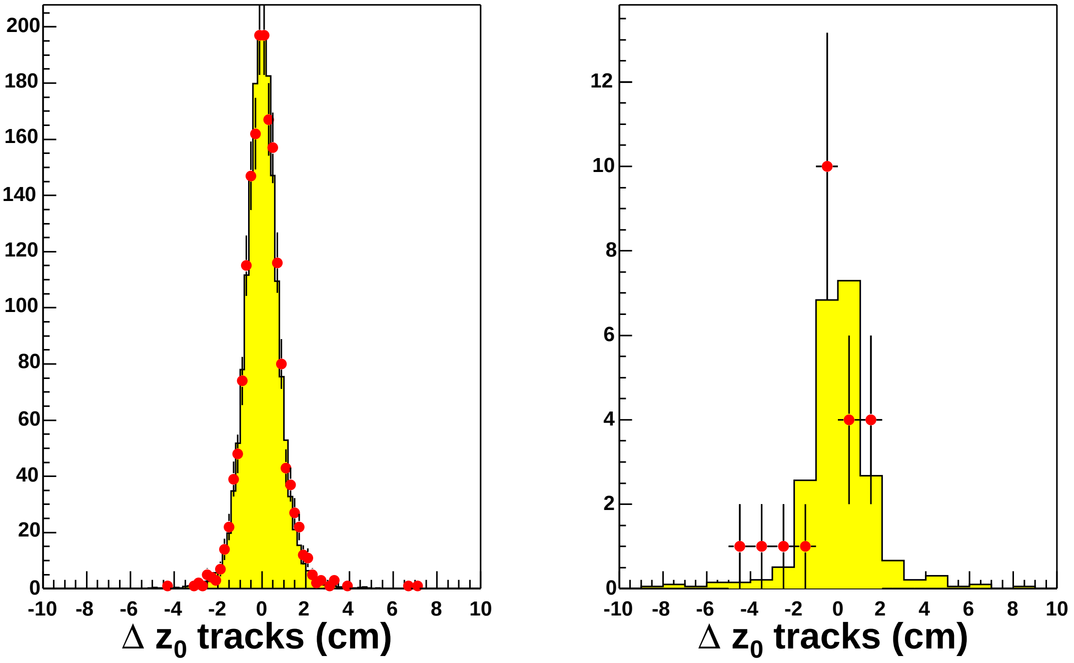

Figure 26: *Δz between the two electron tracks for opposite-sign events (left) and same-sign events (right). The points are* $Z^0/\gamma^* \to e^+e^-$ *candidates and the histograms are* $Z^0/\gamma^* \to e^+e^-$ *Monte Carlo events.*

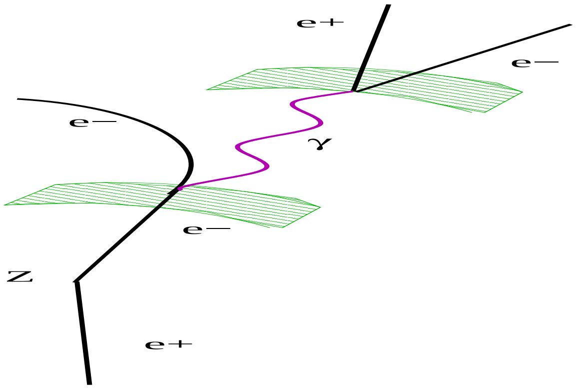

Figure 27: *Sketch of a "trident" event as described in the text. The green bands represent the layers of material in the detector.*

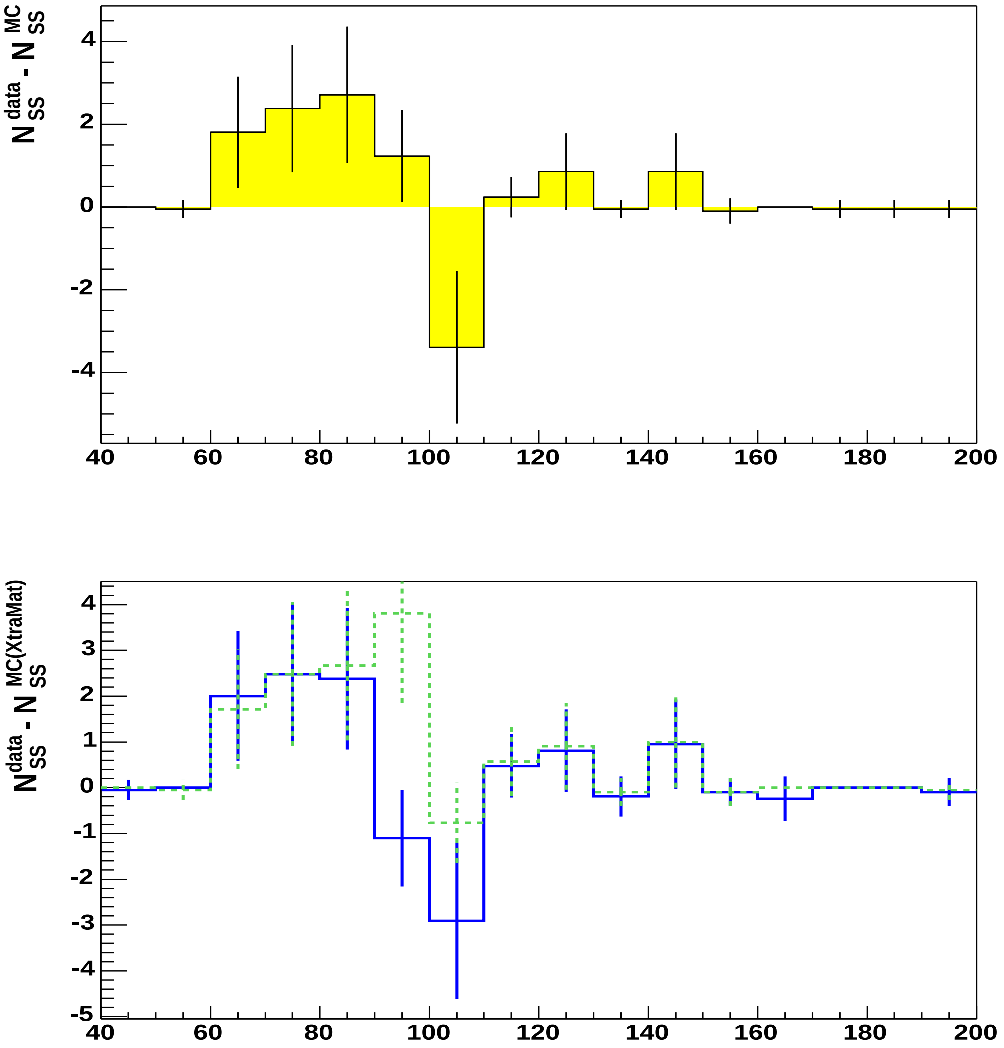

Figure 28: *The same sign invariant mass distribution in the data subtracted by the same sign invariant mass distribution obtained with the* $Z^0/\gamma^* \rightarrow e^+e^-$ *Monte Carlo sample with the default geometry (top) and with the* -1σ*(dotted green histogram) and* $+1\sigma$*(solid blue histogram) extra material (bottom). As expected, in the Monte Carlo with the added extra material the number of SS events (coming from tridents) is higher than in the default Monte Carlo, thus the difference with the data is smaller.*

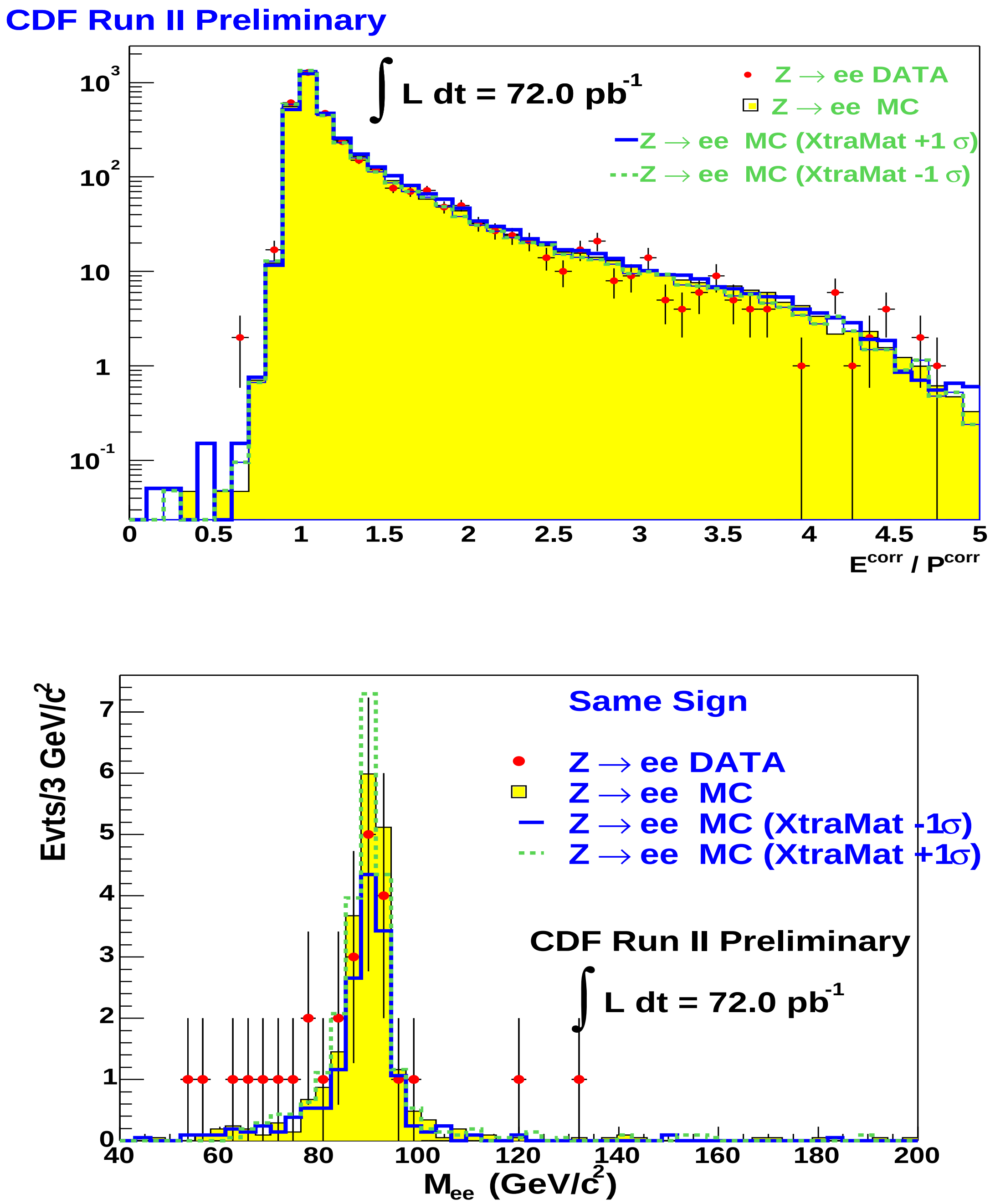

Figure 29: *The E/p distributions for electrons in OS* $Z^0 \rightarrow e^+e^-$ *events (top) and invariant mass distributions of SS events (bottom) for data (points) and Monte Carlo (histograms). The shaded histograms represent simulation with the default geometry and the open histograms represent simulation with the extra* $\pm 1\sigma$ X_0 *of the default material.*

12.2 Background from $Z^0/\gamma^* \rightarrow \tau^+\tau^-$

The production of $Z^0/\gamma^* \rightarrow \tau^+\tau^-$ can sometimes be background to $Z^0/\gamma^* \rightarrow e^+e^-$ events when both taus decay via $\tau \rightarrow e\nu_e\nu_\tau$, and if the electrons form an invariant mass between 66 and 116 GeV/c^2. The Monte Carlo sample described in section III has been used for this study. In the left plot of Figure 30 the invariant mass distribution of the di-electron pairs in the MC $Z^0/\gamma^* \rightarrow e^+e^-$ signal sample is compared with the invariant mass from the di-tau pairs at the generator level . The right plot of Figure 30 shows the invariant mass distribution from di-electron pairs in $Z^0/\gamma^* \rightarrow \tau^+\tau^- \rightarrow ee\nu\nu\nu\nu$ events at the generator level. The reconstructed invariant mass distribution of the electrons from the $Z^0/\gamma^* \rightarrow e^+e^-$ and $Z^0/\gamma^* \rightarrow \tau^+\tau^- \rightarrow ee\nu\nu\nu\nu$ samples is shown in Fig. 31 for the whole range of invariant masses. It can be seen that the majority of the electrons from the tau decays have low invariant masses and would be already rejected by the invariant mass window cut at 66-116 GeV/c^2. In Fig. 32 the reconstructed E_T distributions for the electrons from the two samples are shown. After normalising to the luminosity of the signal Monte Carlo sample, 29 events pass the selection criteria. Assuming lepton universality, the number of $Z^0/\gamma^* \rightarrow \tau^+\tau^-$

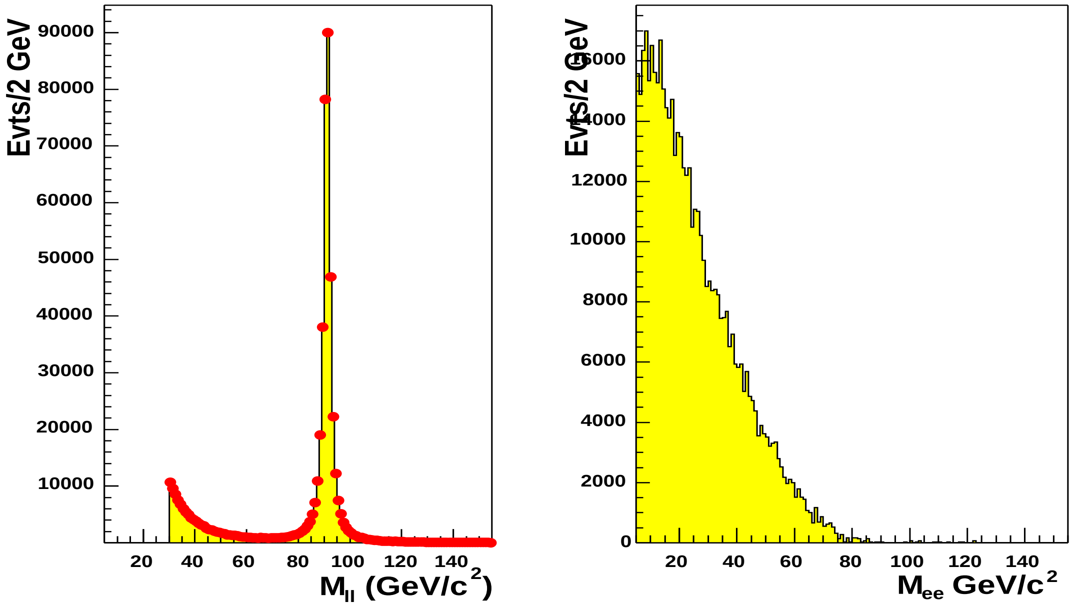

Figure 30: *Left plot: comparison of the $\tau^+\tau^-$ and e^+e^- invariant mass distribution at generator level for the events from $Z^0/\gamma^* \rightarrow e^+e^-$ signal (yellow histogram) and $Z^0/\gamma^* \rightarrow \tau^+\tau^- \rightarrow ee\nu\nu\nu\nu$ background (dots) Monte Carlo as a consistency check before any cut is applied. The peak at low values of $M_{\ell\ell}$ is due to the presence of the γ^*. In the right plot the invariant mass distribution (at generator level) from the electron pairs coming from the taus from the $Z^0/\gamma^* \rightarrow \tau^+\tau^- \rightarrow ee\nu\nu\nu\nu$ decay chain is reported for comparison.*

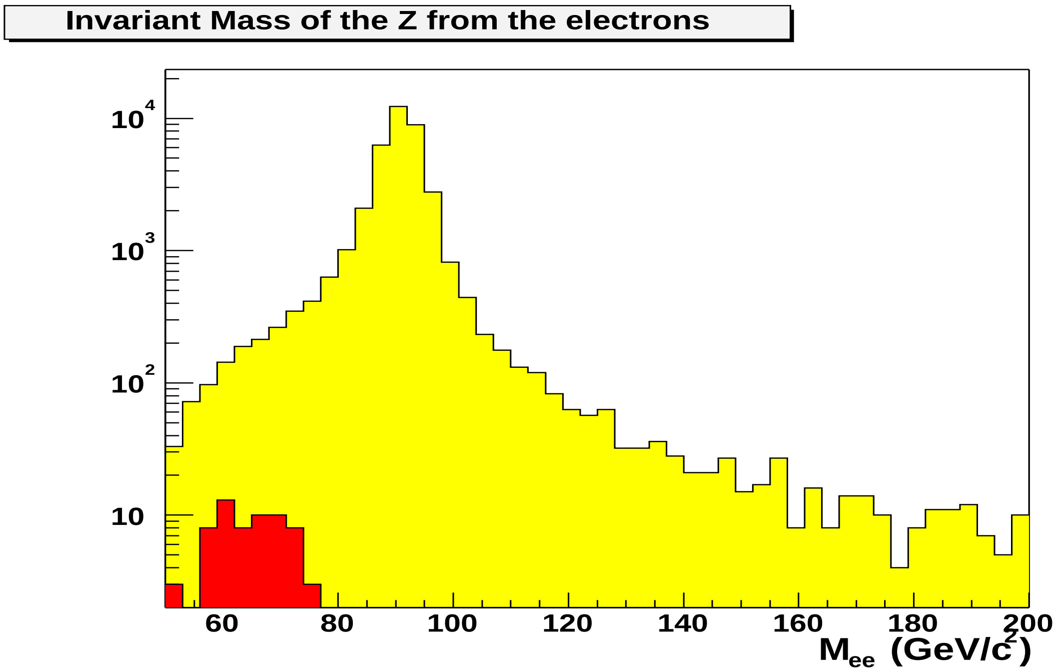

Figure 31: *Invariant mass distribution for the events from* $Z^0/\gamma^* \rightarrow e^+e^-$ *signal (yellow/light shaded histogram) and* $Z^0/\gamma^* \rightarrow \tau^+\tau^- \rightarrow ee\nu\nu\nu\nu$ *background Monte Carlo (red/dark shaded histogram).*

background events can be written as

$$N_{\tau^+\tau^-} = N^{signal}_{e^+e^-} \cdot \frac{r_{\tau\tau}}{r_{ee}}$$

where :

- $N^{signal}_{e^+e^-}$ is the number of $Z^0/\gamma^* \rightarrow e^+e^-$ events in the data, thus

  $N^{signal}_{e^+e^-} = N^{candidates}_{e^+e^-} - N_{\tau^+\tau^-} - N_{others} = N^{candidates}_{e^+e^-} - N_{\tau^+\tau^-} - N_{QCD} - N_{W^\pm \rightarrow e^\pm \nu}$,

  where $N_{\tau\tau}$ is the number of $Z^0/\gamma^* \rightarrow \tau^+\tau^-$ background, N_{QCD} is the number of QCD background and $N_{W^\pm \rightarrow e^\pm \nu}$ is the number of $W \rightarrow e\nu$ background events[2].

- r_{ee} is the number of the $Z^0/\gamma^* \rightarrow e^+e^-$ Monte Carlo events passing the selection criteria, normalised to the luminosity of the signal Monte Carlo sample, and

- $r_{\tau\tau}$ is the number of the $Z^0/\gamma^* \rightarrow \tau^+\tau^-$ Monte Carlo events passing the selection criteria, normalised as before.

The number of $Z^0/\gamma^* \rightarrow \tau^+\tau^-$ background events found is 1.4 ± 0.3, corresponding to $r_{\tau\tau}/r_{ee} = (0.08 \pm 0.02)\%$ contribution to the $Z^0 \rightarrow e^+e^-$ events.

---

[2] See section 12.1 and 12.3 for the calculation of the QCD and $W \rightarrow e\nu$ backgrounds in the $Z^0/\gamma^* \rightarrow e^+e^-$ sample.

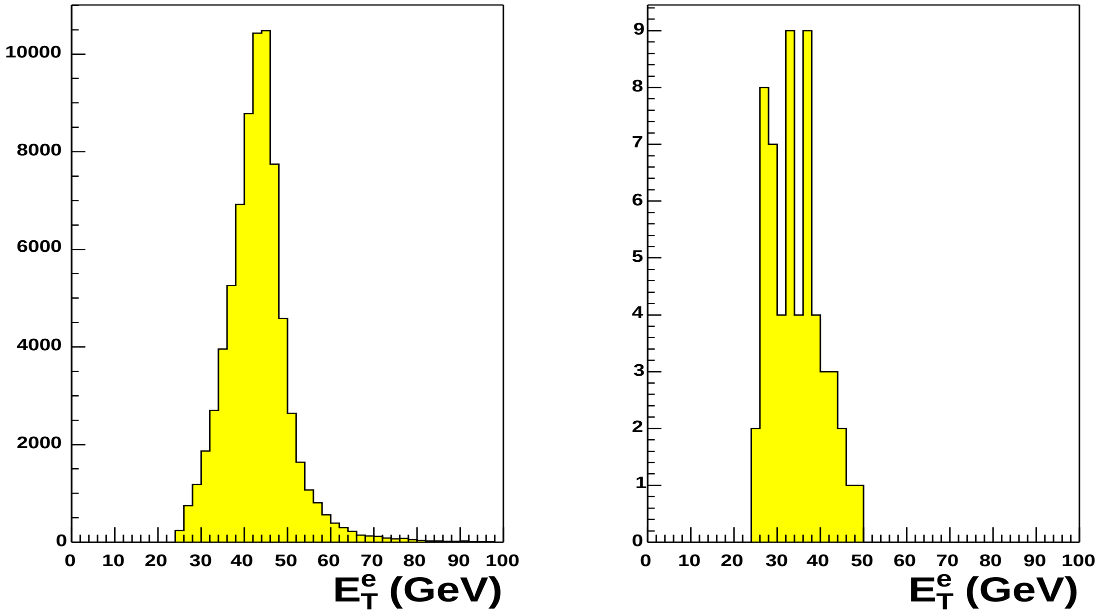

Figure 32: *Transverse energy distribution for the electrons from the Monte Carlo simulation for the* $Z^0/\gamma^* \rightarrow e^+e^-$ *signal (left) and* $Z^0/\gamma^* \rightarrow \tau^+\tau^- \rightarrow ee\nu\nu\nu\nu$ *background (right). The integrated luminosities of the two samples are the same.*

12.3 Background from $W^\pm \rightarrow e^\pm\nu$

The process of W production, where the W decays into an electron and neutrino, can mimic $Z^0/\gamma^* \rightarrow e^+e^-$ decays if the W is produced in association with a hadron jet that showers in the EM calorimeters and the W electron and the jet together fall in the 66-116 GeV/c^2 invariant mass window. The Monte Carlo sample described in section III has been used for this study. The reconstructed invariant mass distribution of the electrons from the $Z^0/\gamma^* \rightarrow e^+e^-$ and $W^\pm \rightarrow e^\pm\nu$ samples is shown in Fig. 33 for the whole range of invariant masses. In Fig. 34 the reconstructed E_T distributions for the electrons from the two samples are shown. After normalising to the luminosity of the signal Monte Carlo sample, 3 events pass the selection criteria. The number of $W^\pm \rightarrow e^\pm\nu$ background events can be written as

$$N_{W^\pm \rightarrow e^\pm\nu} = N_{e^+e^-}^{signal} \cdot \frac{\sigma_{W^\pm \rightarrow e^\pm\nu}}{\sigma_{Z^0 \rightarrow e^+e^-}} \cdot \frac{r_{W^\pm \rightarrow e^\pm\nu}}{r_{ee}}$$

where :

- $N_{e^+e^-}^{signal}$ is the number of $Z^0/\gamma^* \rightarrow e^+e^-$ events in the data, thus

$$N_{e^+e^-}^{signal} = N_{e^+e^-}^{candidates} - N_{W^\pm \rightarrow e^\pm\nu} - N_{others} = N_{e^+e^-}^{candidates} - N_{W^\pm \rightarrow e^\pm\nu} - N_{QCD} - N_{\tau^+\tau^-},$$

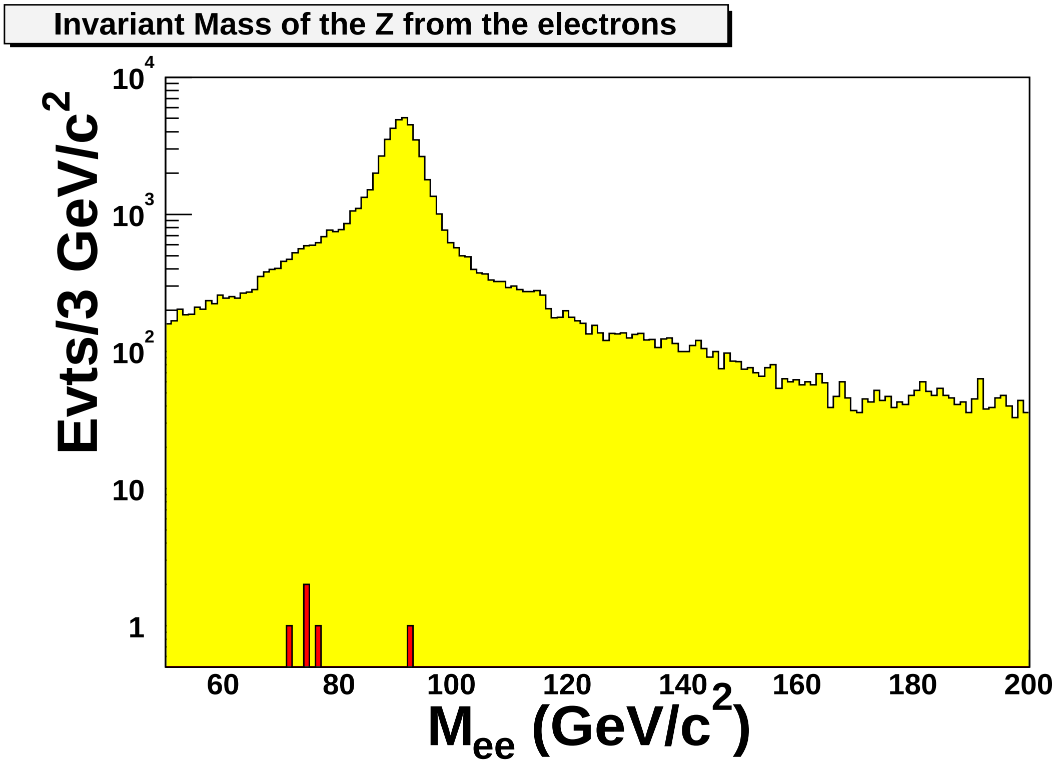

Figure 33: *Invariant mass distribution for the events from* $Z^0/\gamma^* \to e^+e^-$ *signal (yellow/light shaded histogram) and* $W^\pm \to e^\pm\nu$ *background Monte Carlo (red/dark shaded histogram).*

where $N_{\tau\tau}$ is the number of $Z^0/\gamma^* \to \tau^+\tau^-$ background, N_{QCD} is the number of QCD background and $N_{W^\pm \to e^\pm\nu}$ is the number of $W \to e\nu$ background events[3].

- r_{ee} is the number of the $Z^0/\gamma^* \to e^+e^-$ Monte Carlo events passing the selection criteria, normalised to the luminosity of the signal Monte Carlo sample, and
- $r_{W^\pm \to e^\pm\nu}$ is the number of the $W \to e\nu$ Monte Carlo events passing the selection criteria, normalised as before.
- $\frac{\sigma_{W^\pm \to e^\pm\nu}}{\sigma_{Z^0 \to e^+e^-}}$ is the ratio of the theoretical predictions for the $Z^0 \to e^+e^-$ to $W \to e\nu$ cross sections, 10.67±0.15[4].

The number of $W \to e\nu$ background events found is 1.5 ± 0.9, corresponding to $r_{W^\pm \to e^\pm\nu}/r_{ee} = (0.09 \pm 0.05)\%$ contribution to the $Z^0 \to e^+e^-$ events.

---

[3] See section 12.1 and 12.2 for the calculation of the QCD and $Z^0/\gamma^* \to \tau^+\tau^-$ backgrounds in the $Z^0/\gamma^* \to e^+e^-$ sample.

[4] See section 21 for details.

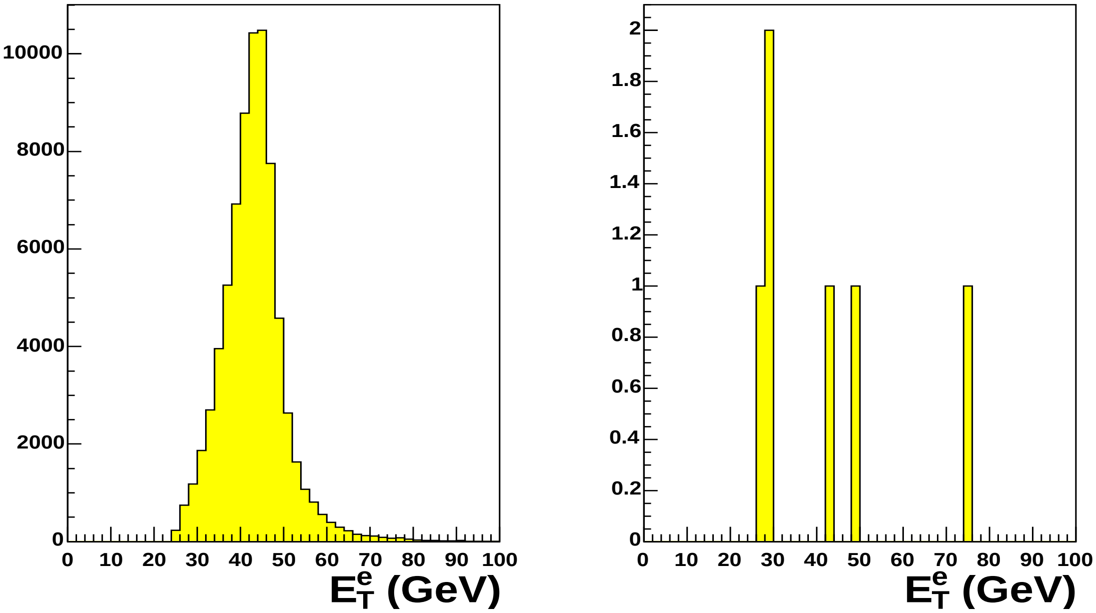

Figure 34: *Transverse energy distribution for the electrons from the Monte Carlo simulation for the* $\mathrm{Z}^0/\gamma^* \to \mathrm{e}^+\mathrm{e}^-$ *signal (left) and* $\mathrm{W}^\pm \to \mathrm{e}^\pm\nu$ *background (right). The integrated luminosities of the two samples are the same.*

12.4 Background Summary

The total number of background events in the $\mathrm{Z}^0 \to e^+e^-$ sample in the invariant mass range of 66 GeV/c^2 and 116 GeV/c^2 is estimated to be 4.5 ± 7.1 events. The main source of background and the number of background events for each source are summarised in Table 5.

source of background	**fraction of the sample**	**number of events**
QCD	$(0.1 \pm 0.4)\%$	1.6 ± 7.0
$\mathrm{Z}^0/\gamma^* \to \tau^+\tau^- \to \mathrm{ee}\nu\nu\nu\nu$	$(0.08 \pm 0.02)\%$	1.4 ± 0.3
$\mathrm{W}^\pm \to \mathrm{e}^\pm\nu$	$(0.09 \pm 0.05)\%$	1.5 ± 0.9
total	$(0.3 \pm 0.5)\%$	4.5 ± 7.1

Table 5: *Sources and amounts of backgrounds to the* $\mathrm{Z}^0/\gamma^* \to e^+e^-$ *signal.*

Part VI

Acceptance

In this section the kinematic and geometric acceptances A_W and A_Z are calculated using the $Z^0/\gamma^* \rightarrow e^+e^-$ and $W^\pm \rightarrow e^\pm\nu$ Monte Carlo samples described in section III. The kinematic component includes the transverse energy threshold for the electrons and the missing transverse energy threshold used to select events with a W boson. The geometric component is the probability that an electron falls within the fiducial volume of the detector. The estimates of the acceptances and their uncertainties are discussed here.

13 W acceptance

The acceptance of the kinematic and geometrical selection criteria for the $W \rightarrow e\nu$ candidate event sample is obtained directly from Monte Carlo. The kinematic and geometric cuts used to select the sample are

- Central EM cluster ($|\eta| < 1.0$)
- Central EM cluster considered fiducial as determined from the CES cluster.
- Matching COT track with $p_T > 10$ GeV/c.
- EM cluster $E_T > 25$ GeV.
- $\not\!\!E_T > 25$ GeV.

As discussed in subsequent sections, the Monte Carlo is tuned to provide the best possible match with data. COT track p_T is scaled down in the Monte Carlo by 0.3% to match the observed scale in the data, and the event recoil E_T (the E_T observed in the calorimeter minus the E_T associated with the lepton) is tuned so that the Monte Carlo distributions match those observed in the data. In addition, we studied tuning the EM cluster E_T scale, the EM cluster E_T resolution, and the COT track p_T resolution but found that these parameters in the Monte Carlo were in good agreement with the data.

Table 6 shows the total number of $W \rightarrow e\nu$ events in our Monte Carlo sample and the number that pass each of the kinematic and geometric selection cuts listed above. Each individual selection cut is applied only to the subset of events that pass the other kinematic and geometrical criteria listed above it in the table. The Monte Carlo includes a realistic model of the interaction region, but we do not take the acceptance of our requirement on the z-position of the lepton vertex ($|z_0| < 60$ cm) directly from Monte Carlo. Instead, as discussed in section 20, we measure the efficiency of the z_0 cut from data using minimum bias events. In order to avoid double-counting the effect of this requirement, the event number used in the denominator of our acceptance calculation comes from the subset of events in the Monte Carlo sample where the z-coordinate of the generated primary vertex satisfies $|z_{vtx}| < 60$ cm. This is the first selection criterion applied to events in the Monte Carlo sample, and the acceptance of the subsequent requirements is based on the number of events listed next to this cut in the table.

Applied Cut	Number of Events	Cut Acceptance	Net Acceptance
Total Events	1933957		
$\lvert z_{vtx}\rvert < 60$ cm	1870156	0.9670 ± 0.0001	
Central EM Cluster	927231	0.4958 ± 0.0004	0.4958 ± 0.0004
Fiducial	731049	0.7884 ± 0.0004	0.3909 ± 0.0004
COT Track $p_T > 10$ GeV/c	647691	0.8860 ± 0.0004	0.3463 ± 0.0003
EM Cluster $E_T > 25$ GeV	488532	0.7543 ± 0.0005	0.2612 ± 0.0003
$\not\!\!E_T > 25$ GeV	447836	0.9167 ± 0.0004	0.2395 ± 0.0003

Table 6: $W \to e\nu$ Acceptance Calculation.

13.1 W Acceptance Systematics

13.1.1 Boson p_T Uncertainty

As discussed in section 6, we have tuned the boson p_{T} distribution generated by PYTHIA to CDF's Run 1 measurement of the fully corrected $d\sigma/dp_{\mathrm{T}}$ of ee pairs in the mass region $66 < M_{ee} < 116$ GeV. The "tuned" γ^*/Z p_{T} distribution is shown in Fig. 3.

In order to study how our understanding of the shape of the boson p_{T} distribution affects our acceptance calculation we vary the parameters in PYTHIA we used to tune this distribution. Our boson p_{T} tuning "knobs" are PARP(62) and PARP(64), the parton shower evolution Q^2 parameters, PARP(91) and PARP(93), the "K_{T} smearing" parameters. We perform a χ^2 comparison of the Z boson p_{T} between the Run 1 data and PYTHIA Monte Carlo as we vary the values of these parameters, as shown in figures 35- 38. We find the minima of the χ^2 distributions to be consistent with the values of these parameters which we used to generate all our Monte Carlo samples. The results are summarized in table 7.

The uncertainty on our understanding of the shape of the boson p_{T} distribution is obtained from the 3σ points in our χ^2 fits. We choose to use the 3σ points rather than the 1σ points because the parameters we used to tune the boson p_{T} are merely "knobs" rather than describing something physical we want to be more conservative in estimating the uncertainty on these tuning parameters. To determine how the $W \to e\nu$ acceptance changes with the shape of the W p_{T} distribution we reweight this distribution in our default Monte Carlo with factors obtained from the $\pm 3\sigma$ values of the PYTHIA parameters. We find that PARP(93) has a negligible effect on the shape of the boson p_{T} and on the acceptance. Figures 39- 41 show how the p_{T} distribution is affected by varying the parameters by 3σ. In table 8 we

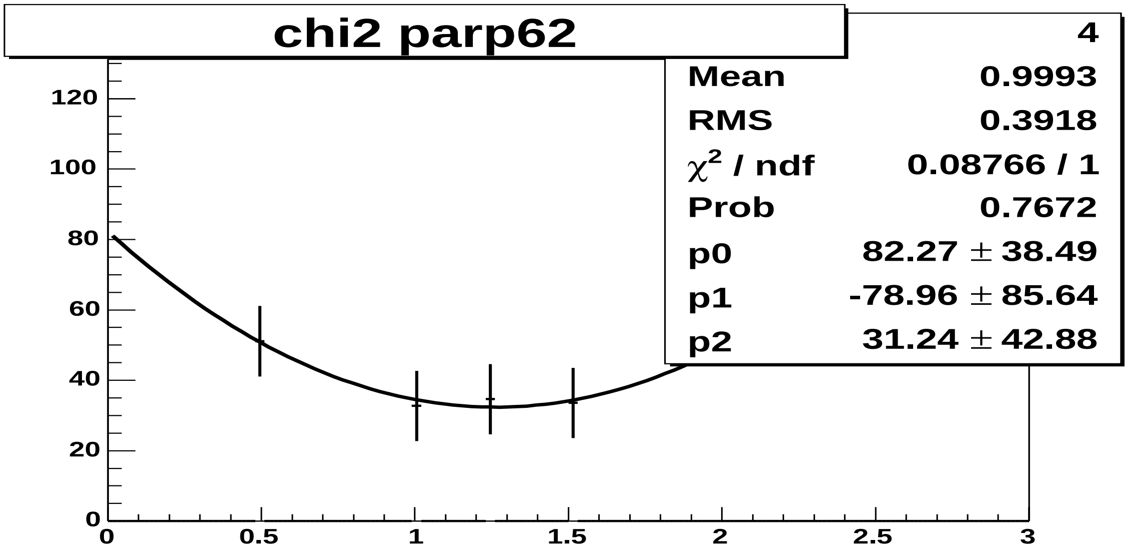

Figure 35: *χ^2 fits for PYTHIA Z boson p_T tuning parameter PARP(62).*

summarize the changes in the $W \to e\nu$ acceptance as we vary these parameters. We estimate the total uncertainty on the acceptance due to our understanding of the boson p_T distribution to be:

$$\sigma_A = 0.043\%.$$

Parameter	Description	Default Generated	Minimum	1 σ	3 σ
PARP(62)	Q^2 min. for parton showers	1.25	1.26	0.18	0.30
PARP(64)	scale factor for K_T evolution	0.2	0.2	0.02	0.03
PARP(91)	K_T sigma	2.1	2.0	0.17	0.3
PARP(93)	K_T max. cutoff	15	14	2	3

Table 7: *Results of χ^2 fits used to obtain PYTHIA Z boson p_T tuning parameters and their variations.*

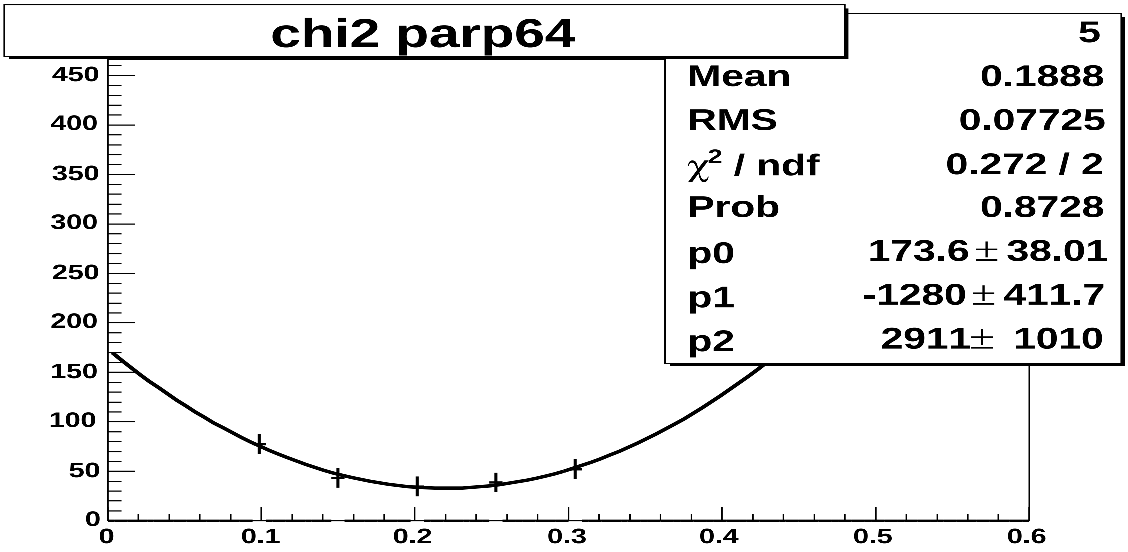

Figure 36: χ^2 *fits for PYTHIA Z boson* p_{T} *tuning parameter PARP(64).*

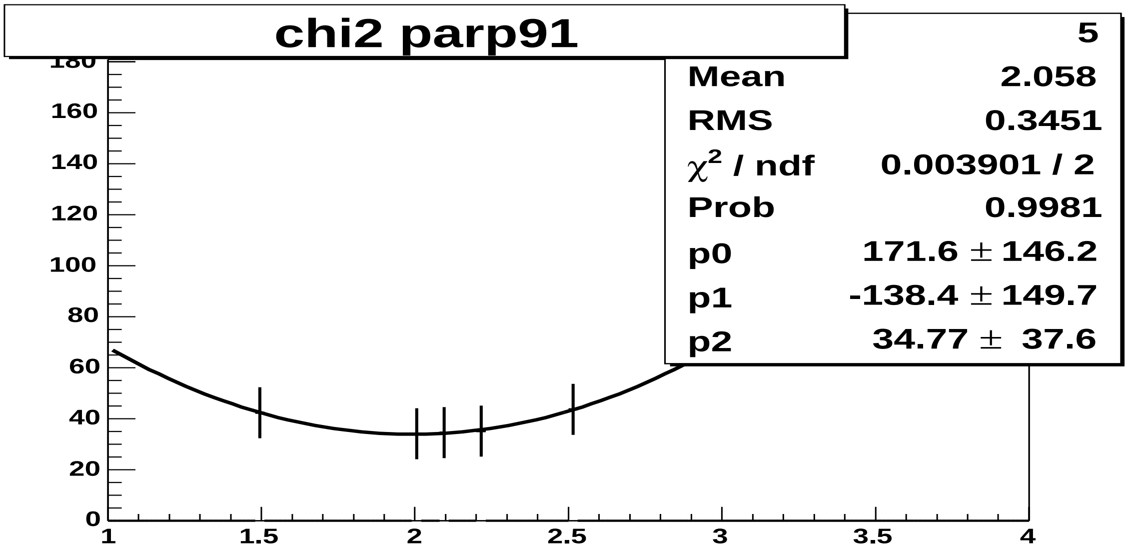

Figure 37: χ^2 *fits for PYTHIA Z boson* p_{T} *tuning parameter PARP(91).*

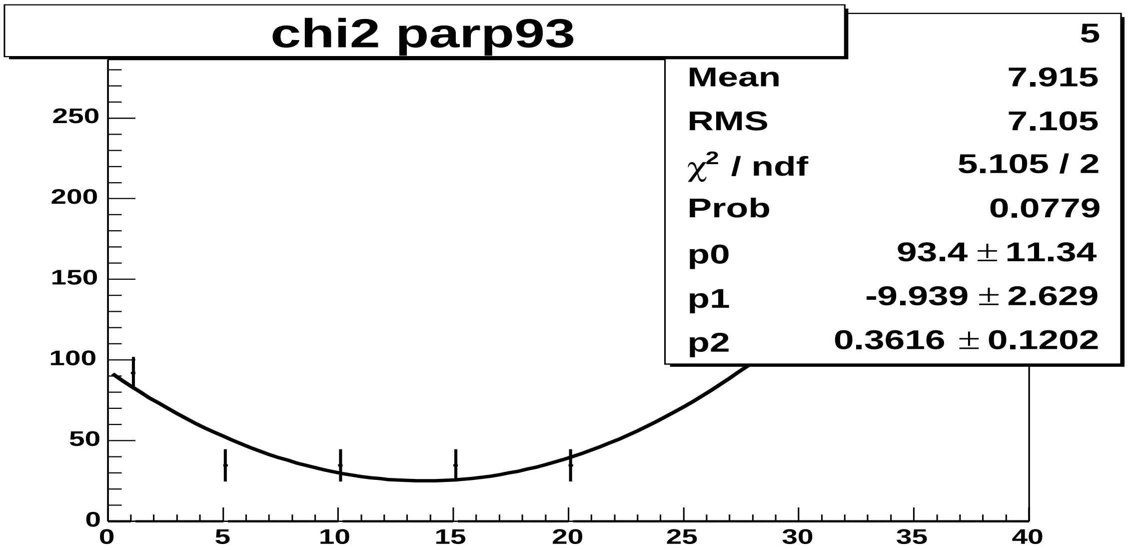

Figure 38: *χ^2 fits for PYTHIA Z boson p_{T} tuning parameter PARP(93).*

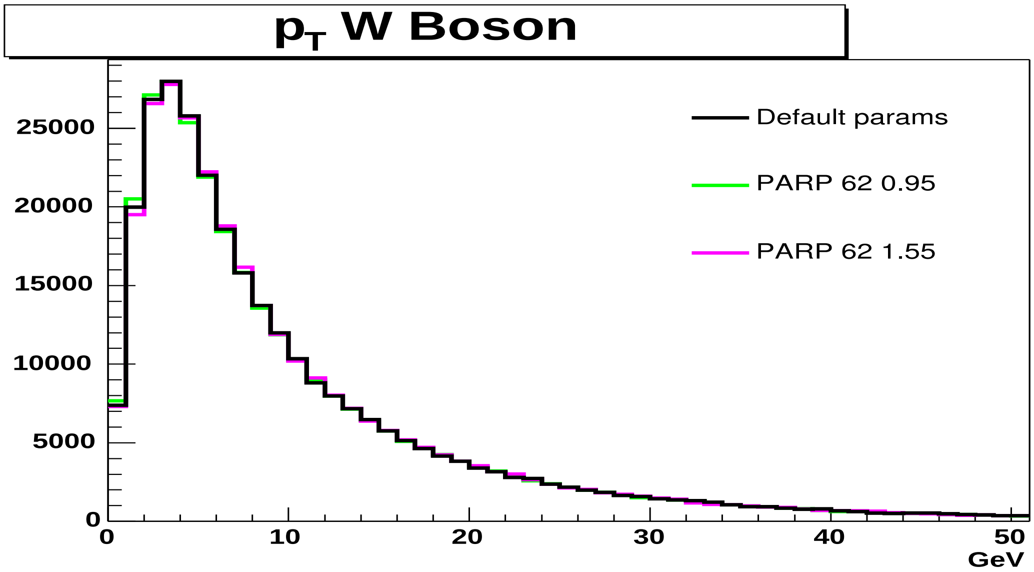

Figure 39: *W p_{T} distribution for our default PYTHIA parameters compared to the $\pm 3\sigma$ values for PARP(62).*

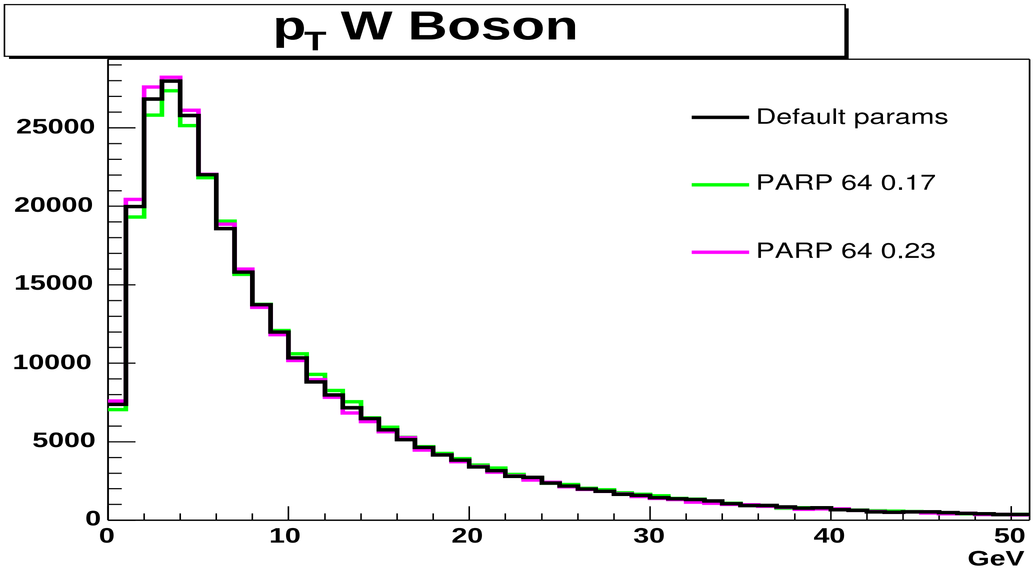

Figure 40: *W p_T distribution for our default PYTHIA parameters compared to the* $\pm 3\sigma$ *values for PARP(64).*

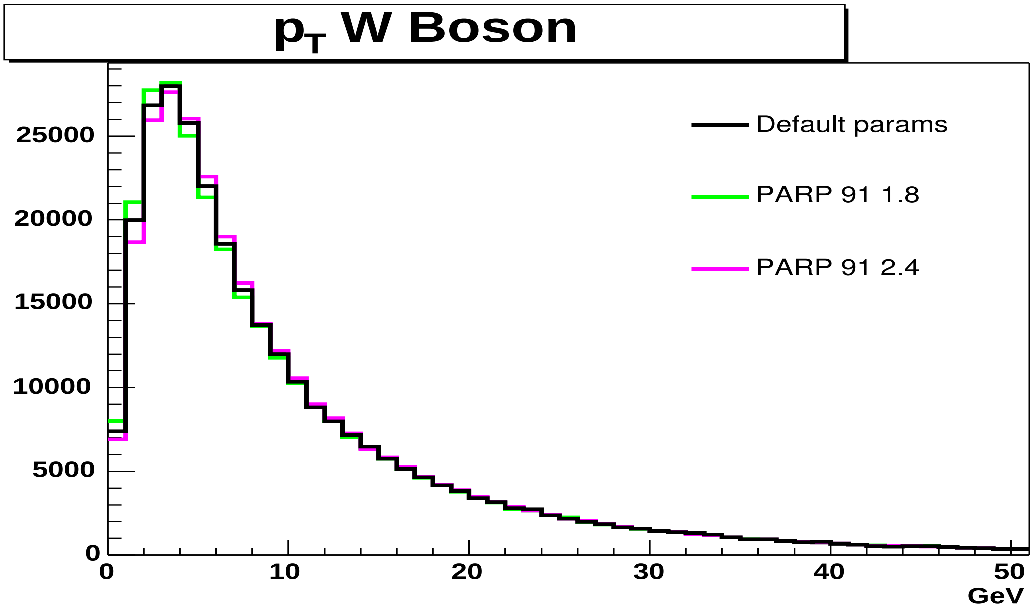

Figure 41: *W p_T distribution for our default PYTHIA parameters compared to the* $\pm 3\sigma$ *values for PARP(91).*

Parameter	Δ Acceptance/A (%)
PARP(62)	0.003
PARP(64)	0.040
PARP(91)	0.015
PARP(93)	0
Total	0.043

Table 8: % change in $W \to e\nu$ acceptance for different p_{T} tuning parameters in PYTHIA.

13.1.2 PDF Uncertainty

Momentum distributions of the quarks and gluons inside the proton are required as input for simulation of the Monte Carlo samples used to determine the experimental acceptance. Since these distributions are only known to a certain level of accuracy, the resulting uncertainties in these distributions contribute to the overall uncertainty on our determined acceptance values. This error contribution is estimated using CTEQ6 parton distribution functions (PDF's) which are described in greater detail in [42]. The CTEQ6 PDF parametrization uses the best values for the 20 parameters, $\mathbf{P_i}$, which describe the quark and gluon distributions within the proton (and anti-proton). These are determined by minimizing the χ^2 of a global fit to experimental data. Since the covariance matrix for the $\mathbf{P_i}$ parameters is non-diagonal in the vicinity of the fit minimum, it is difficult to propagate the fit errors back into uncertainties on experimentally measured quantities such as our acceptances. However, the CTEQ6 authors have been able to determine a different set of orthogonal parameters, $\mathbf{Q_i}$, which do in fact diagonalize the covariance matrix of the fit in the vicinity of the minimum. Based on this parametrization, individual $\pm\sigma$ variations of the $\mathbf{Q_i}$ can be transformed back into $\mathbf{P}$ space to generate a new set of "error" PDFs. An "up" and "down" PDF set is generated for each of the 20 $\mathbf{Q_i}$, resulting in a grand total of 40. Changes in measurable quantities such as our acceptance coming from the "up" and "down" PDF sets associated with each of the orthogonal $\mathbf{Q_i}$ are added in quadrature to determine a total uncertainty due to our PDF model. The actual procedure used to determine the changes in our acceptances arising from each of the "error" PDF sets is described in much greater detail in [43]. The final uncertainties due to the PDF model on the $W \to e\nu$ acceptance that we obtain from this procedure is:

$$\sigma_A = {}^{+1.15}_{-1.41}\%.$$

13.1.3 p_T/E_T Scale/Resolution Uncertainty

The acceptance of the electron-track p_T requirement and the electron-cluster E_T requirement are also taken directly from Monte Carlo. Therefore, it is also important to tune the scales and resolutions of the track p_T and cluster E_T in the Monte Carlo to match those observed in the data. More indirectly, the electron-cluster E_T enters into the recoil energy calculation and can therefore affect the $\not\!\!E_T$ measurement. As discussed in the previous section, the acceptance of the $\not\!\!E_T$ criteria comes directly from the Monte Carlo so inaccurate modeling of the E_T scale and/or resolution can also affect the central acceptance value via this criterion.

The Monte Carlo track-p_T scale and resolution is tuned using $Z \to \mu\mu$ candidate events. The fraction of background events in this sample is well below 1% so it is possible to make a direct comparison of the $Z \to \mu\mu$ invariant mass spectra in data and Monte Carlo to study the scale and resolution of the track-p_T measurement. The formula used to tune the track-p_T scale is shown in Equation 10

$$p'_T \;=\; K_{Pt} \times p_T \tag{10}$$

In order to determine the best value for the scaling factor K_{Pt}, we perform χ^2 fits between the $Z \rightarrow \mu\mu$ invariant mass distributions in data and Monte Carlo over a range of potential values for K_{Pt}. The fit results are shown in Figure 42. The best χ^2 fit is obtained for a Monte Carlo track-p_T scaling factor of 0.997. Since the mean of the $Z \rightarrow \mu\mu$ invariant mass peak is centered on the world average mass value, a Monte Carlo track-p_T scale factor below one indicates that the current p_T scale for reconstructed tracks in the data is too low. This result is consistent with Monte Carlo track-p_T scaling factors obtained from similar fits to the $J/\psi \rightarrow \mu\mu$ and $\Upsilon \rightarrow \mu\mu$ invariant mass peaks indicating that the scale factor is not p_T dependent.

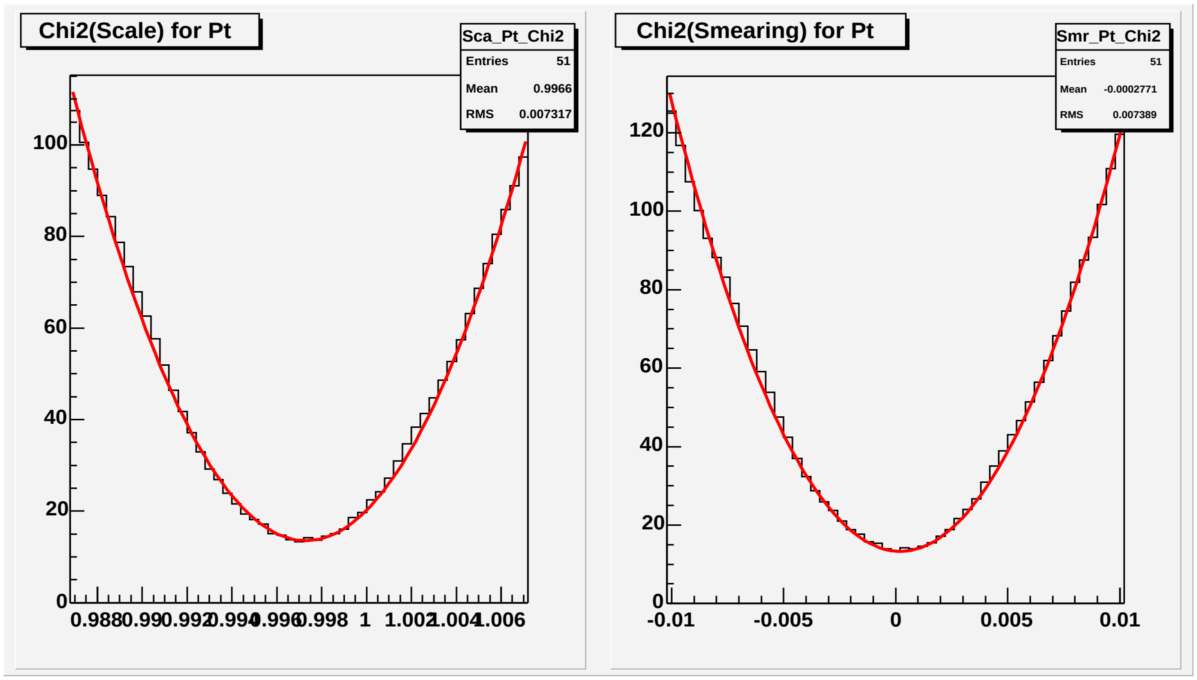

Figure 42: *χ^2 fits for K_{Pt} using $M_{\mu\mu}$ (left); χ^2 fits for σ_{Pt} using $M_{\mu\mu}$ (right).*

We also use χ^2 fits between the $Z \rightarrow \mu\mu$ invariant-mass distributions in data and Monte Carlo to tune the track-p_T resolution in the Monte Carlo. We smear the Monte Carlo track-p_T values by generating a random number from a Gaussian distribution with mean equal to one and width equal to σ for each track in the sample. The smearing is obtained by multiplying each track-p_T by its associated random number. Note that a value of zero for σ corresponds to the case of no additional p_T smearing since each random number is one by definition. The best value for σ is obtained from χ^2 fits between the $Z \rightarrow \mu\mu$ invariant mass distributions in data and Monte Carlo over a range of potential values for σ. These fit results are also shown in Figure 42. In this case, the best χ^2 fit is found to be for the case of $\sigma = 0$ indicating that track p_T resolution in the Monte Carlo is well modeled.

The exact same procedures are used to tune electron-cluster E_T scale and resolution in the Monte Carlo. The only difference is that the χ^2 fits are made to the $Z \to ee$ invariant mass distributions obtained from data and Monte Carlo rather than the $Z \to \mu\mu$ distributions. The results of these fits are shown in Figure 43. The fits indicate that both the scale and resolution of electron-cluster E_T in the Monte Carlo are in good agreement with data and no tuning of these parameters is necessary.

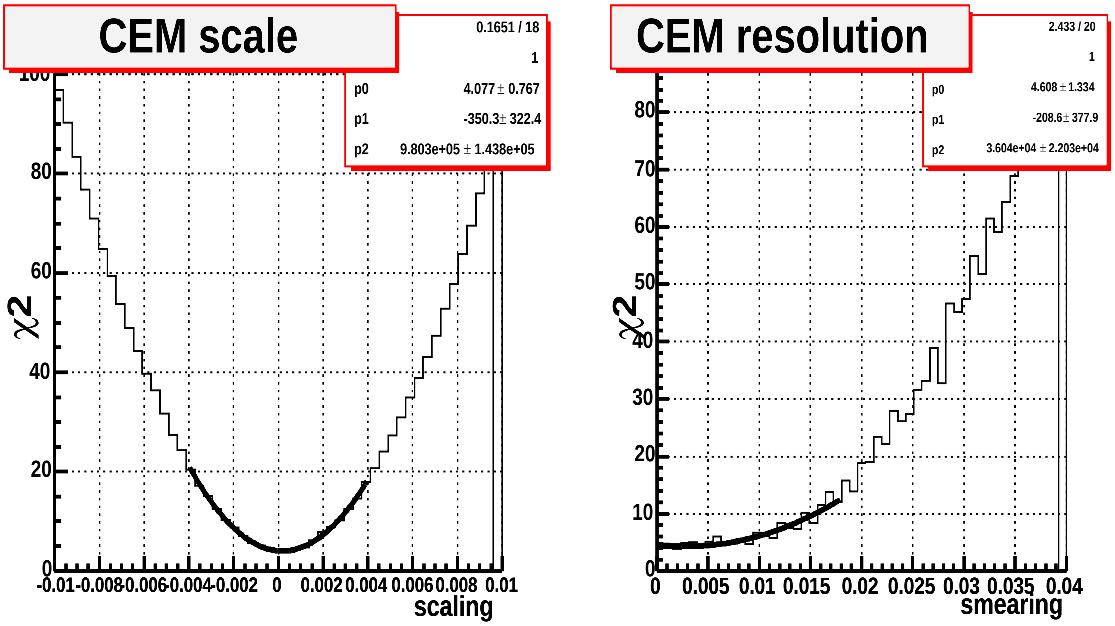

Figure 43: χ^2 *fits for* K_{Et} *using* M_{ee} *(left);* χ^2 *fits for* σ_{Et} *using* M_{ee} *(right).*

The track-p_T scaling factor of 0.997 is applied to lepton tracks in the $W \to e\nu$ Monte Carlo sample used to calculate the central acceptance value. Since the track p_T resolution, electron-cluster E_T scale, and the electron-cluster E_T resolution in the Monte Carlo are all found to be in good agreement with data, these parameters are not tuned in the sample used to obtain the central acceptance result. However, we still need to determine the error on the overall acceptance value due to each of these potential tuning parameters based on the uncertainties obtained from our χ^2 fit procedure. In the case of these tuning parameters, we choose the standard 3σ points from our χ^2 fits to estimate the error on the acceptance due to each parameter. For each of the four tuning parameters, the overall contribution to the error on the acceptance is obtained by re-calculating the $W \to e\nu$ acceptance with the individual tune parameter changed to its $\pm 3\sigma$ values. The larger change in acceptance is taken as the overall error due to the tuning parameter being studied. The results of the χ^2 fits used to obtain the central values and uncertainties for these tuning parameters is shown in Table 9. A comparison of the $Z \to \mu\mu$ and $Z \to ee$ invariant mass distributions in data and tuned Monte Carlo are shown in Figures 44 - 45.

Fit	K_{Pt}	σ_{Pt}	K_{Et}	σ_{Et}
Using	$M_{\mu\mu}$	$M_{\mu\mu}$	M_{ee}	M_{ee}
Degrees of Freedom	25	25	25	25
χ^2_{Min}				
Fit Value	0.997	1.000	1.000	1.000
$+3\sigma$ Value	1.000	1.003	1.003	1.015
-3σ Value	0.994	0.997	0.997	0.985
$+3\sigma$ % Acceptance Change	+0.025	-	+0.34	-0.028
-3σ % Acceptance Change	-0.027	-	-0.34	-

Table 9: *Results of χ^2 fits used to obtain track p_T and electron-cluster E_T scale and resolution tuning parameters.*

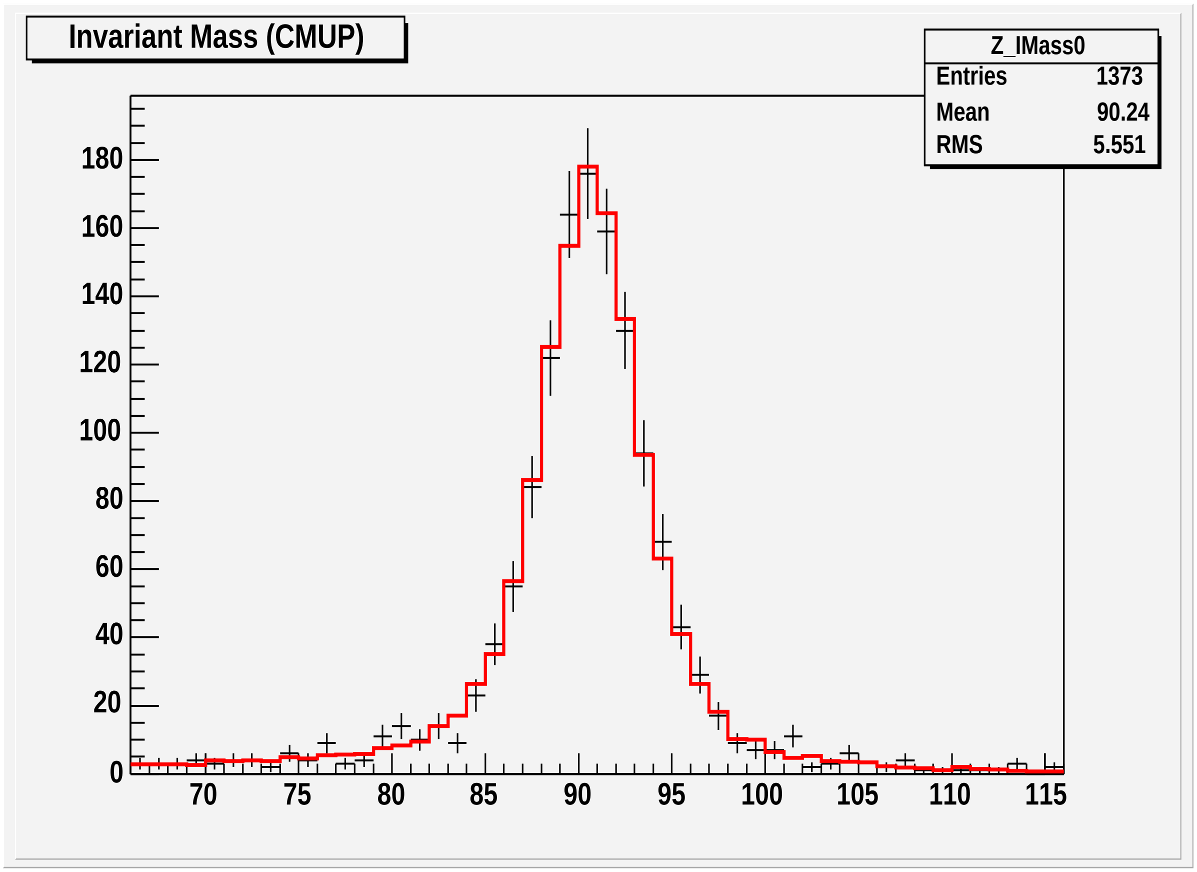

Figure 44: *Comparison of $Z \to \mu\mu$ invariant mass distribution in data and tuned Monte Carlo.*

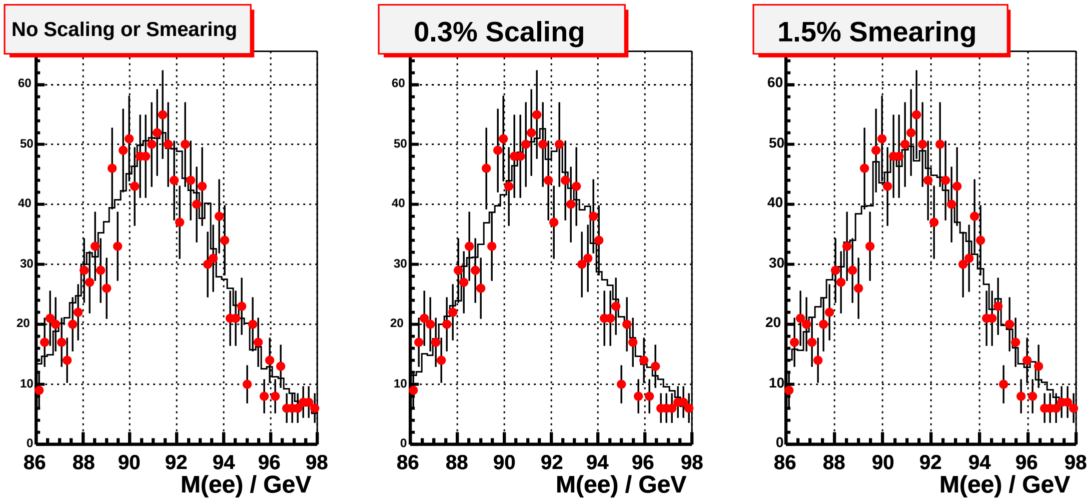

Figure 45: *Data (markers) and simulation (histograms) comparison for (left) no extra scaling or smearing of the simulation; (centre) 0.3% scaling; and (right) 1.5% smearing, corresponding to the* $\chi^2_{min} + 9$ *points.*

13.1.4 Material Uncertainty

To determine the systematic uncertainty due to our knowledge of the material description of the tracking volume in the Monte Carlo (section 7) we generated and simulated special samples which reflect the $\pm 1\sigma$ uncertainty in our measurements of the material in the central and in the plug (section III). In the central we added a thick copper cylinder, corresponding to an extra 1.5% X_0 with respect to the default, placed between the beam-line and the COT inner radius. In the plug we add an iron plate, corresponding to an extra 1/6 of X_0.

Table 10 summarizes how the acceptance changes in these samples compared to the default.

MC Dataset	Description	Δ A/A %
`wewk3e`	+ 1.5% X_0 Cu in central	-0.68
`wewk4e`	- 1.5% X_0 Cu in central	0.73
`wewkae`	+ 1/6 of X_0 Fe in plug	negl.
`wewk6e`	- 1/6 of X_0 Fe in plug	negl.
total		0.73

Table 10: % change in $W \to e\nu$ acceptance for material systematic.

13.1.5 Recoil Energy Uncertainty

The acceptance of the missing $\not\!\!E_T$ selection cut for $W \to e\nu$ events is taken directly from the Monte Carlo. Since the calorimeter energy measurement plays an important role in determining the $\not\!\!E_T$, it is important to tune the Monte Carlo model for calorimeter energy deposition in $W \rightarrow e\nu$ events to provide the best possible match with data. The modeling of hadronic showering, the boson recoil-energy, and the underlying event energy in the Monte Carlo can be inaccurate to some degree and lead to differences between the Monte Carlo model and the data. In addition, the current Monte Carlo does not model the effects of multiple interactions and accelerator backgrounds. To account for these potential differences between data and Monte Carlo, we tune the raw calorimeter distributions in Monte Carlo to match those observed in the data.

First, we define the recoil energy of an event in the directions parallel and perpendicular to the direction of the high p_T lepton from the W boson decay in the transverse plane of the detector. Equations 11 - 14 show the prescription used for calculating these components of the recoil energy.

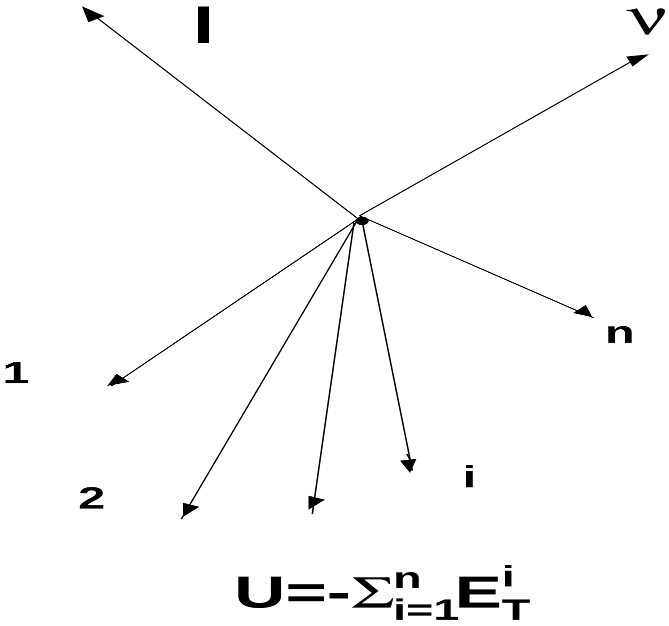

Figure 46: *Kinematics of W boson production and decay, as viewed in the transverse plane to the proton-antiproton beams.*

$$\begin{aligned}
U_x^{recl} &= -\not\!\!E_{T\,x} - (E_T^{EM} + E_T^{HAD})\cos(\phi_e) && (11)\\
U_y^{recl} &= -\not\!\!E_{T\,y} - (E_T^{EM} + E_T^{HAD})\sin(\phi_e) && (12)\\
U_\parallel^{recl} &= U_x^{recl}\cos(\phi_e) + U_y^{recl}\sin(\phi_e) && (13)\\
U_\perp^{recl} &= U_x^{recl}\sin(\phi_e) - U_y^{recl}\cos(\phi_e) && (14)
\end{aligned}$$

We assume that the appropriate corrections to apply to the Monte Carlo recoil-energy model are an overall scale correction for both the parallel and perpendicular directions and an additional constant term in the parallel direction (shift correction). The scaling correction accounts for potential problems in modeling calorimeter response and the effects of multiple interactions, the underlying event model, and accelerator backgrounds which should not be dependent on the lepton direction. The shift correction is designed to account for modeling effects that do have a lepton-direction dependence such as the W boson recoil model and the model for lepton energy deposition in the calorimeter. We expect that no shift correction should be applied to the recoil-energy in the direction perpendicular to the lepton, but we check this assumption by allowing for a potential additional constant term in the correction for this component.

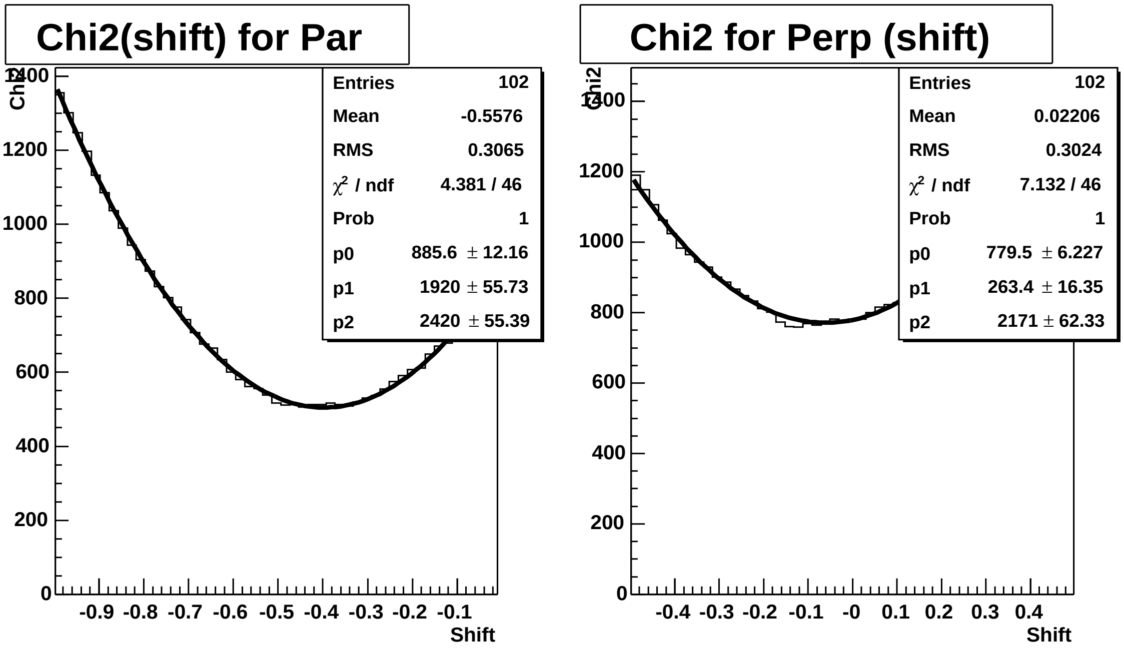

Figure 47: χ^2 *fits for* $C_{\parallel}$ *using* $U_{\parallel}^{recl}$ *(left) and* $C_{\perp}$ *using* $U_{\perp}^{recl}$ *(right).*

$$(U_{\parallel}^{recl})' = (K_{\parallel} \times U_{\parallel}^{recl}) + C_{\parallel} \tag{15}$$

$$(U_{\perp}^{recl})' = (K_{\perp} \times U_{\perp}^{recl}) + C_{\perp} \tag{16}$$

Equations 15 - 16 show the formula used to correct the Monte Carlo recoil energy distributions to match those seen in data. In order to determine the best values for the scaling and shifting constants in these formulas, we perform χ^2 fits between the data recoil energy distributions and corrected Monte Carlo distributions for a range of scaling and shifting constants. An iterative process is used in which we first determine the best possible shifting constants and then fit for scaling constants based on those values. We repeat this process until the χ^2 fits for both the scaling and shifting constants stabilize at set values. Figure 47 shows the results of the final χ^2 fits for the recoil energy shift corrections in the parallel and perpendicular directions. As expected, the fitted shift in the perpendicular direction is consistent with zero; and since no effects consistent with a shift in this direction are expected, we choose to apply no correction. The χ^2 fit prefers a non-negligible shift in the recoil energy along the lepton direction, however, and we apply this correction to the Monte Carlo sample used to calculate the central acceptance numbers.

The final χ^2 fits for the recoil energy scale corrections are shown in Figure 48. The fits shown in this figure are done independently for the directions parallel and perpendicular to the lepton direction and give similar results ($K_\parallel = 1.06$ and $K_\perp = 1.04$). Based on our model for these corrections, however, the scale corrections for both directions should be the same. Therefore, we can also perform a combined χ^2 fit of the recoil energy distributions for both directions to determine a single scaling correction. This χ^2 fit is shown in Figure 49 and as expected gives a scaling correction consistent with the individual fits to the recoil energy distributions in each direction. We choose to use the one scaling correction obtained from the combined fit to the recoil energy scale correction applied to both the parallel and perpendicular directions in the Monte Carlo sample used to calculate the central acceptance numbers. We can also check our result by performing a χ^2 fit to the $U_T^{recl} = ((U_\parallel^{recl})^2 + (U_\perp^{recl})^2)^{\frac{1}{2}}$ distribution for the single scaling factor, K. This fit is also shown in Figure 49 and the result for K is consistent with the values obtained from the other fit methods.

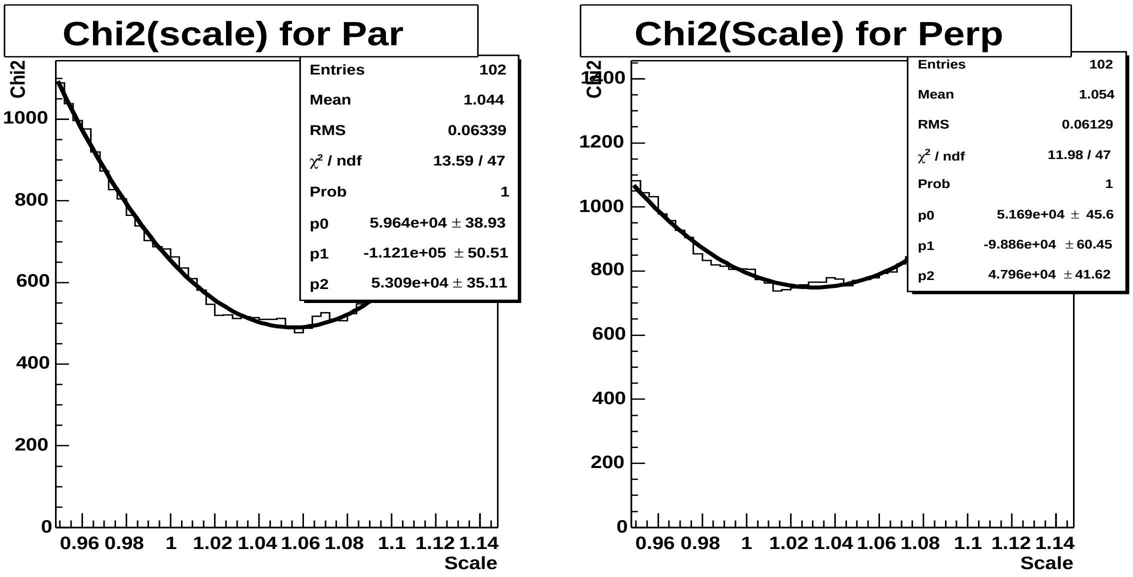

Figure 48: *χ^2 fits for $K_\parallel$ using $U_\parallel^{recl}$ (left) and $K_\perp$ using $U_\perp^{recl}$ (right).*

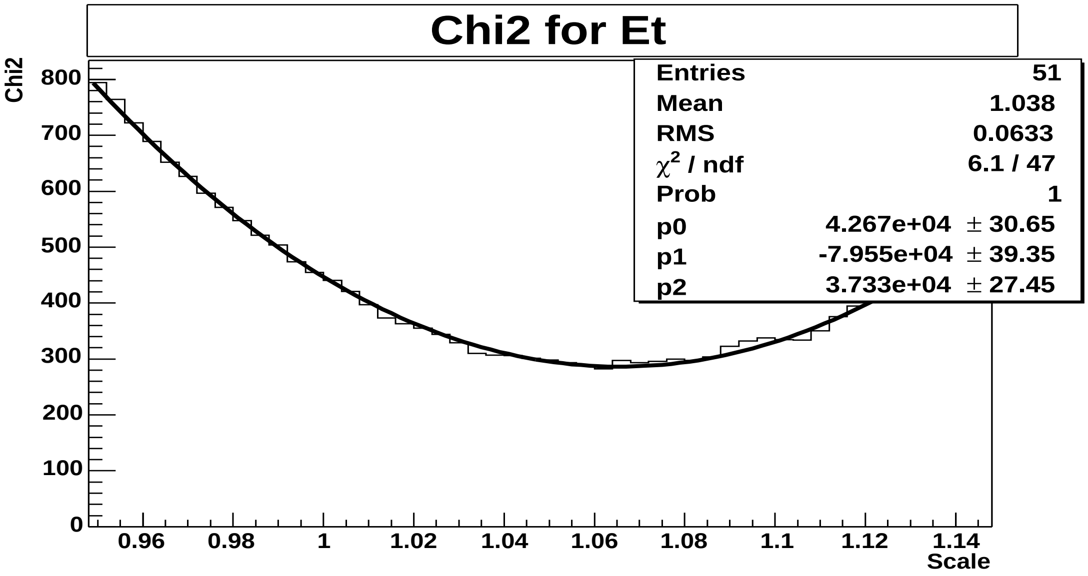

Figure 49: *Combined* χ^2 *fit for* K *using* $U_{\parallel}^{recl}$ *and* $U_{\perp}^{recl}$ *(left) and* U_{T}^{recl} *(right).*

The uncertainties on our recoil energy scaling and shifting corrections are obtained from the 3σ points in our χ^2 fits. We choose to use the 3σ points rather than the 1σ points because we are utilizing recoil energy tuning in the Monte Carlo to take into account a broad range of potential problems with our model. Because of this fact, we want to be more conservative in estimating the uncertainty on these tuning parameters. The overall error on the acceptance based on the uncertainty in the recoil energy tuning parameters is obtained from re-calculations of the $W \to e\nu$ acceptance with individual Monte Carlo tune parameters changed to their $\pm 3\sigma$ values. We add in quadrature the changes in acceptance found from modifying the overall scale correction K, the shift correction for the parallel direction $C_{\parallel}$, and the perpendicular direction $C_{\perp}$. The change in acceptance for each individual parameters is based on the larger of the two acceptance changes from the $\pm 3\sigma$ values. Note that we include the change in acceptance due to the 3σ shift in $C_{\perp}$ even though we choose to set the central value for this parameter to zero.

Fit Using	$K_{\parallel}$ $U_{\parallel}^{recl}$	$K_{\perp}$ $U_{\perp}^{recl}$	K U_{T}^{recl}	K $U_{\parallel}^{recl} + U_{\perp}^{recl}$	$C_{\parallel}$ $U_{\parallel}^{recl}$	$C_{\perp}$ $U_{\perp}^{recl}$
Degrees of Freedom	310	313	273	623	310	313
χ^2_{Min}	242	382	298	631	249	373
Fit Value	1.06	1.04	1.07	1.05	-0.4	-0.04
$+3\sigma$ Value	0.02	0.02	0.02	0.02	0.1	0.1
-3σ Value	0.02	0.02	0.02	0.02	0.1	0.1
$+3\sigma$ % Acceptance Change	-	-	-	-0.16	0.17	negligible
-3σ % Acceptance Change	-	-	-	0.17	-0.18	negligible

Table 11: *Results of χ^2 fits used to obtain recoil energy tuning parameters.*

The results of the χ^2 fits used to obtain the central values and uncertainties for the tuning parameters defined in Equations 15 - 16 are shown in Table 11. Also shown in this table are the changes in the overall $W \rightarrow e\nu$ acceptance obtained from changing each of the three utilized tune values to their $\pm 3\sigma$ values. As noted above, the overall error on the acceptance due to the recoil energy model is determined by adding in quadrature the larger of the acceptance changes for each of the three tune parameters. A comparison of the tuned Monte Carlo recoil energy distributions with those obtained from the data are shown in Figures 50 - 55. Good agreement is seen in each of the distributions ($U_{\parallel}^{recl}$, $U_{\perp}^{recl}$, and U_{T}^{recl}).

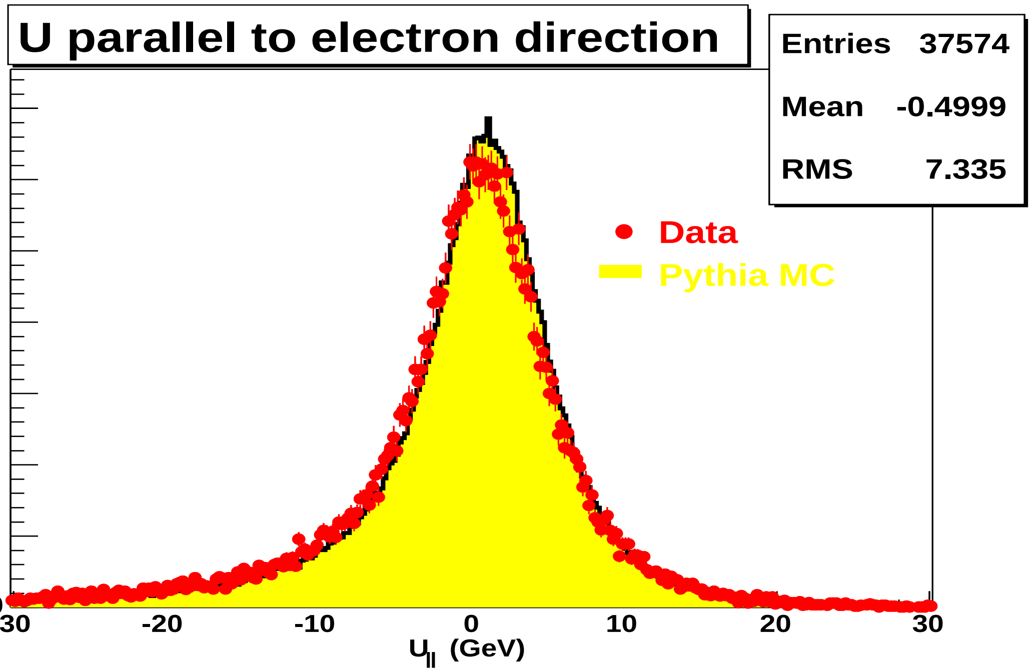

Figure 50: $U_{\parallel}^{recl}$ *in data (black) versus untuned Monte Carlo (red).*

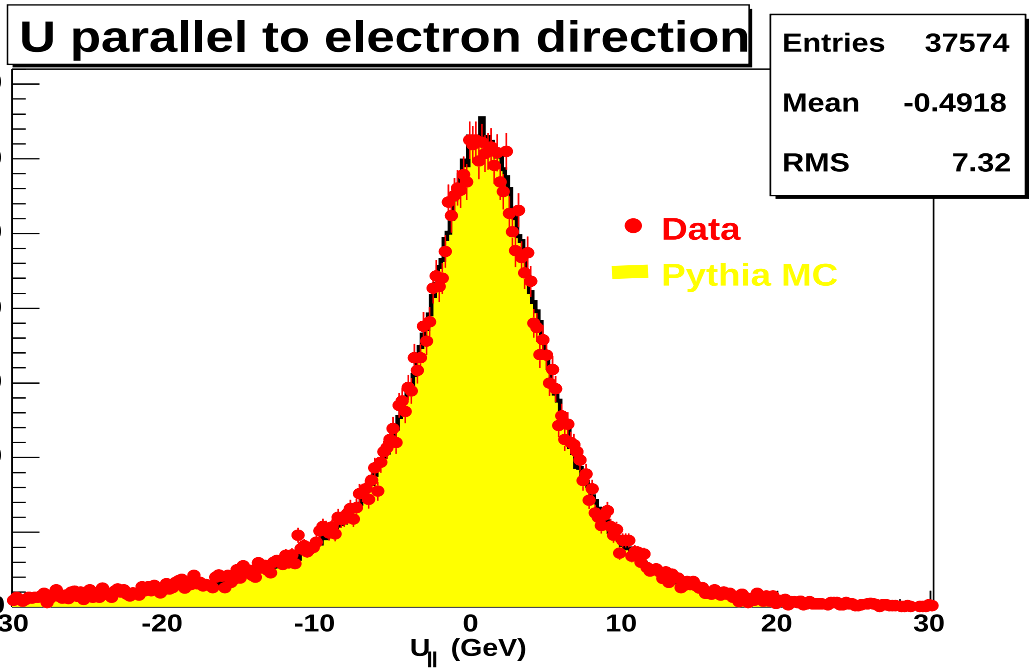

Figure 51: $U_{\parallel}^{recl}$ *in data (black) versus tuned Monte Carlo (red).*

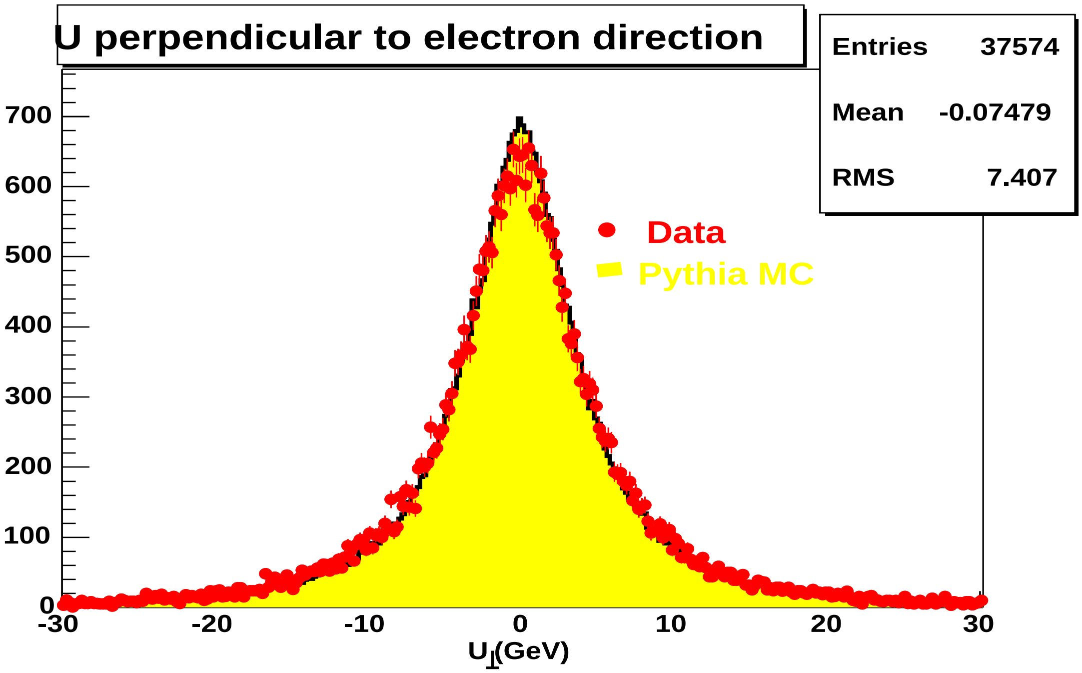

Figure 52: $U_{\perp}^{red}$ *in data (black) versus untuned Monte Carlo (red).*

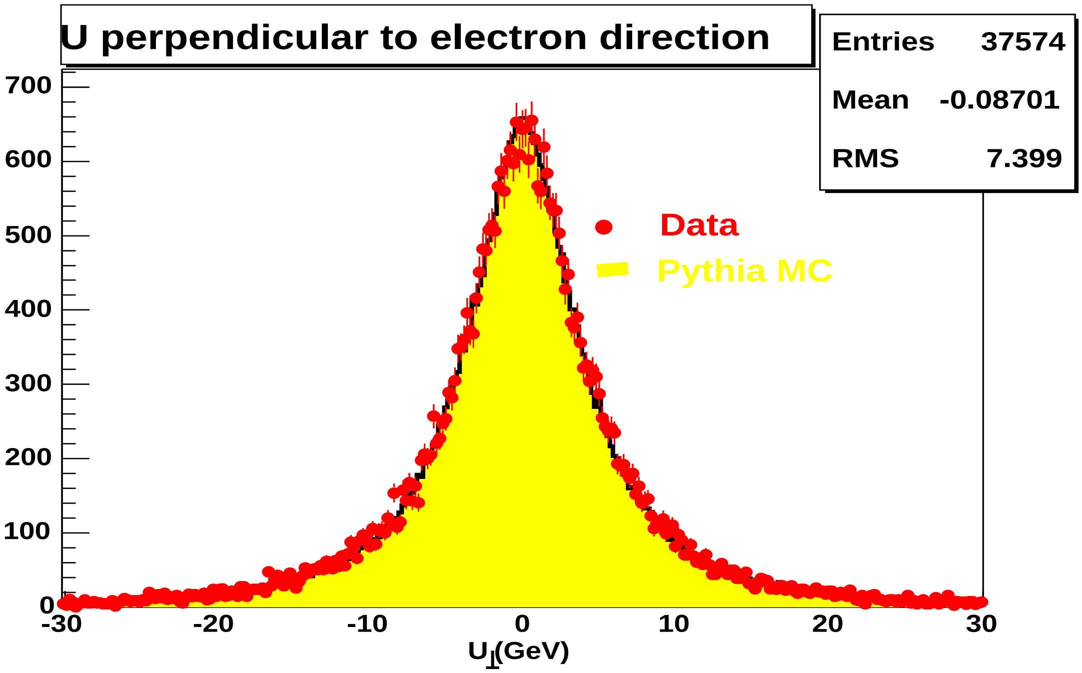

Figure 53: $U_{\perp}^{red}$ *in data (black) versus tuned Monte Carlo (red).*

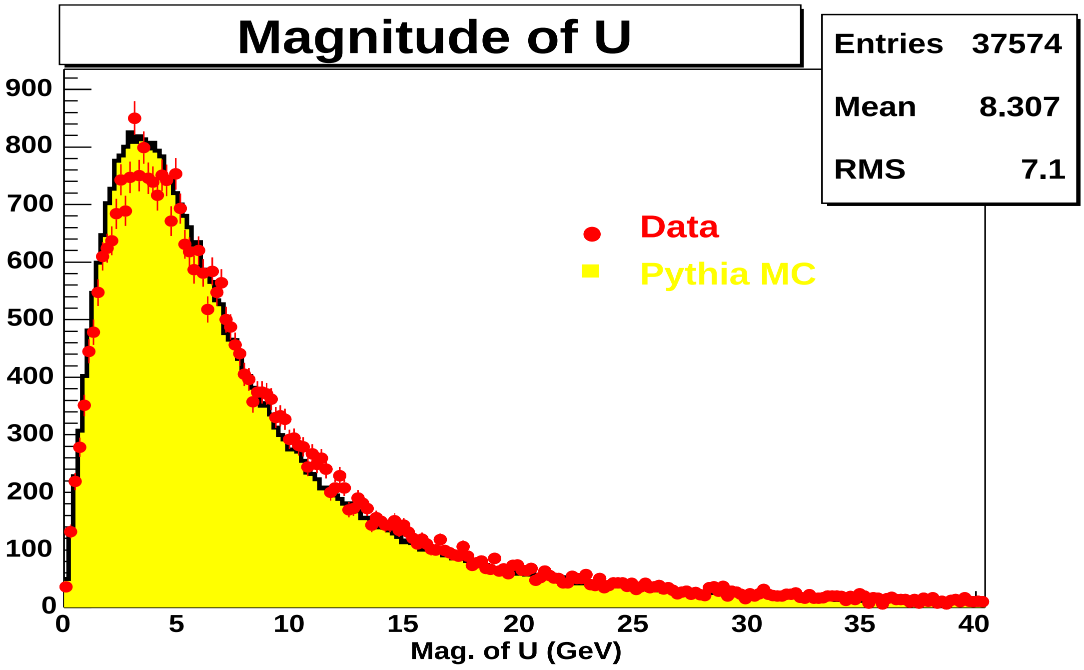

Figure 54: U_T^{rec} *in data (black) versus untuned Monte Carlo (red).*

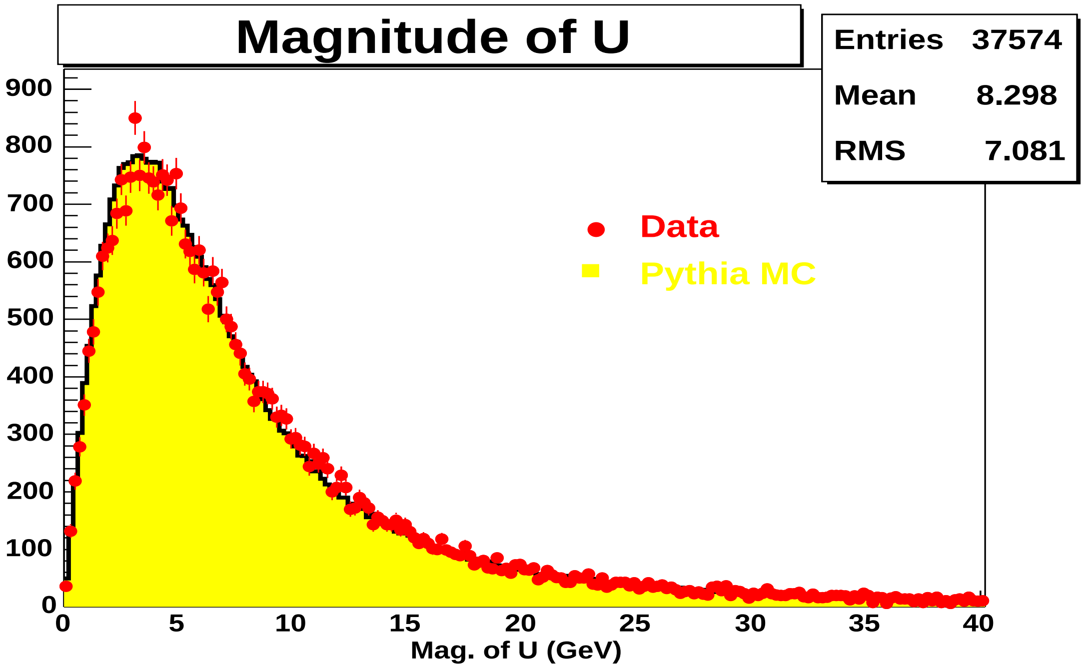

Figure 55: U_T^{rec} *in data (black) versus tuned Monte Carlo (red).*

13.2 W Acceptance Summary

The total $W \to e\nu$ acceptance is

$$A_W \;=\; (23.95 \pm 0.03(stat)^{+0.34}_{-0.39}(syst))\%$$

The systematic uncertainties on the acceptance are summarized in Table 12.

Source	$\Delta A/A$ (relative) (%)	ΔA (absolute) (%)
$E_T^{\rm e}$ scale	0.34	0.08
$E_T^{\rm e}$ resolution	0.03	0.01
p_T scale	0.03	0.01
p_T resolution	negl.	negl.
$\vec{U}$ scale	0.25	0.06
$p_T^{\rm W}$ modelling	0.04	0.01
Material	0.73	0.17
PDF's	$^{+1.15}_{-1.41}$	$^{+0.28}_{-0.34}$
Overall	$^{+1.43}_{-1.64}$	$^{+0.34}_{-0.39}$

Table 12: Systematic uncertainties on the acceptance.

14 Z acceptance

The acceptance for the geometric and kinematic cuts in Table 3 was determined using the MC sample of $Z^0/\gamma^* \to e^+e^-$ events described in section III. As stated there, the generated events have been simulated and have gone through the same reconstruction algorithms as the data. Events in this sample were selected by requiring:

1. The z position of the primary vertex at generator level to lie within ±60 cm of the proton-antiproton interaction point at $z = 0$; and the presence of at least 2 electrons[5] with the following characteristics[6]:

2. The cluster contained no towers in the Plug calorimeter.

3. The region "tower 9" was excluded.

4. The cluster was in the fiducial region (according to the CES variables) as shown in Figure 56 (see section 8 for the definition of the fiducial volume).

---

[5] Events with no reconstructed electron were discarded.

[6] The selection criteria are applied to the quantities obtained after passing through the entire reconstruction chain.

5. The p_T as measured by the beam-constrained COT tracking was greater than 10 GeV/c.
6. E_T was greater than 25 GeV.
7. The reconstructed invariant mass of the electrons was within 66 and 116 GeV/c^2.
8. The charge of the tracks associated with the electrons was of opposite sign.

The acceptance is

$$A_Z = \frac{\text{number of events passing cuts 1. to 8.}}{\text{number of events with } 66 < M_{\text{ee}}^{gen} < 116 \text{ GeV}/c^2 \text{ and } |z_{vertex}^{gen}| < 60 \text{ cm}}.$$

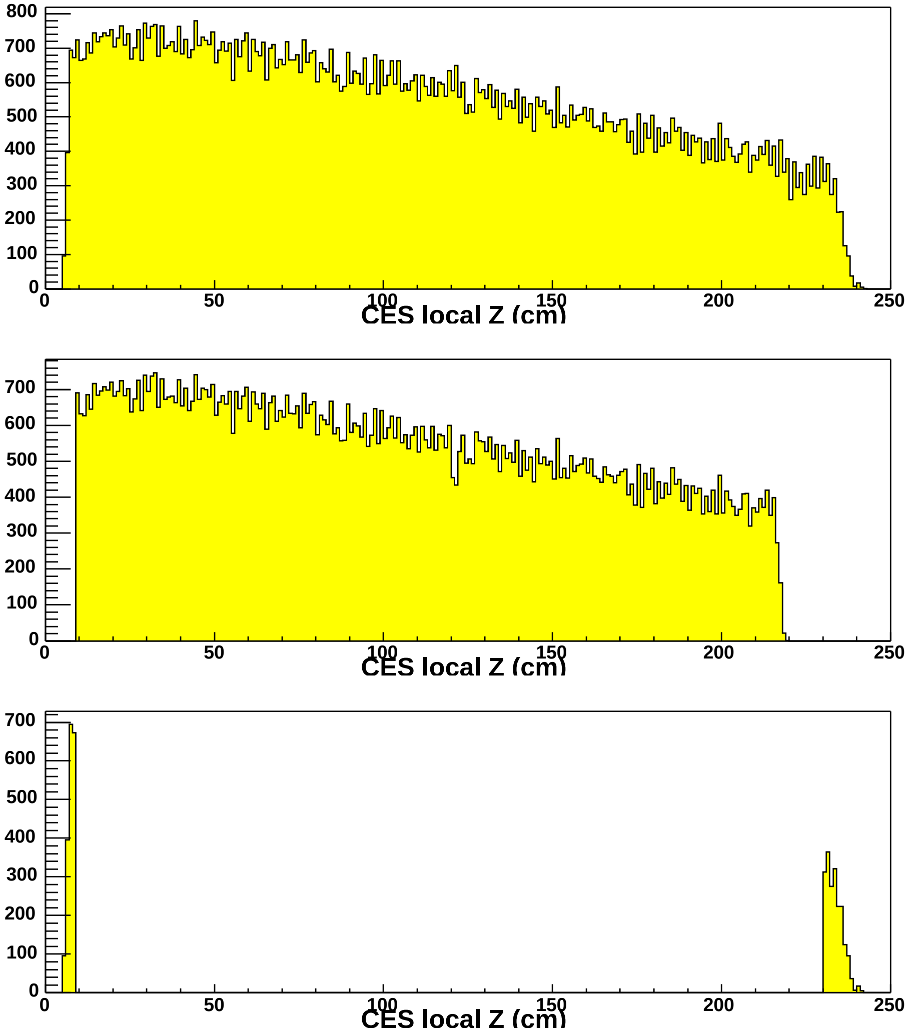

Figure 56: *The Z coordinate as reconstructed from the CES for all the electrons in the event(upper plot), for the electrons in the events passing the fiducial cut (middle plot), and for the events that fail the fiducial cut (bottom plot). The regions* $|Z_{CES}| < 9$ cm *and* $|Z_{CES}| > 230$ cm *are excluded as expected (see section 8 and Table 13).*

The effect of each cut is summarized in Table 13.

Selection	Default		-1σ $\mathbf{X_0}$ Material	$+1\sigma$ $\mathbf{X_0}$ Material
	# of events	Acceptance	Acceptance	Acceptance
generated $\|z^{gen}_{vertex}\|$ <60 cm	490756			
$\geq$ 1 `CdfEmObject`	488003			
first electron				
no plug towers	363994	96.67%	96.70%	96.66%
no seed in tower 9	350496	93.09%	93.13%	93.07%
fiducial:				%
$\|x\| < 21$ cm; 9< $\|z\|$ <230 cm	299530	79.55%	79.50%	79.61%
no “chimney”; no “tower 9”:				%
p_T >10 GeV/c	252881	67.16%	67.63%	66.78%
E_T >25 GeV	186318	49.48%	49.73%	49.22%
second electron				%
no plug towers	94418	25.08%	25.19%	25.01%
no seed in tower 9	88806	23.59%	23.67%	23.51%
fiducial:				%
$\|x\| < 21$ cm; 9< $\|z\|$ <230 cm	61908	16.44%	16.41%	16.50%
no “chimney”; no “tower 9”:				%
p_T >10 GeV/c	48410	12.86%	12.96%	12.76%
E_T >25 GeV	43799	11.63%	11.76%	11.54%
$66 < M_{ee} < 116$ GeV/c^2	42123	11.19%	11.30%	11.09%
opposite sign	41462	11.01%	11.16%	10.89%
Total Acceptance $\mathbf{A}_Z$		(11.01±0.05)%	11.2%	10.9%

Table 13: *Effect of each geometric/kinematic cut on electrons and events. The numbers in the middle columns are originated from the default* $Z^0 \rightarrow e^+e^-$ *Monte Carlo simulation and the numbers in the right column are originated from the simulation when the extra material is added. The fractions are with respect to the number of events with 66 <* M^{gen}_{ee} *<116 GeV/*c^2 *and* $|z^{gen}_{vertex}|$ *<60 cm, which is equal to 376523.*

The effect of reweighting the z primary vertex distribution has been studied at an earlier stage of the analysis[44] and found to be negligible. The effect of the reweighting of the p_T distribution will be discussed in section 14.1.1.

The acceptance is found to be

$$A_Z = 11.01 \pm 0.05(stat.)\%, \tag{17}$$

where the uncertainty is the statistical error of the Monte Carlo simulation sample. As a cross check, a calculation of the acceptance has been performed with the same cuts as defined in the Run I analyses [45; 46] and the details can be found in [44].

14.1 Z Acceptance Systematics

The systematic uncertainties on the calculation of the acceptance include several elements. Their single contributions are analysed in the following sections. In each case the input parameters of the Monte Carlo responsible of the effect (corresponding to the variable) under investigation are varied and the change in acceptance is examined.

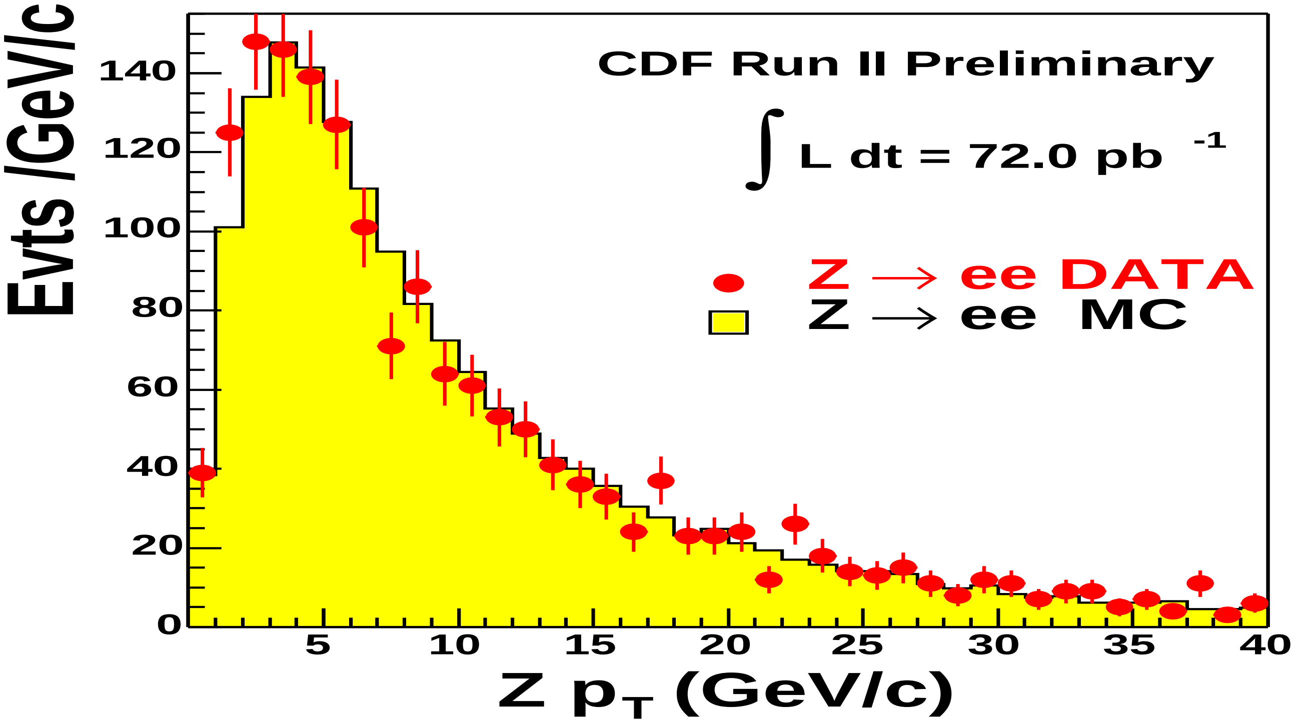

Figure 57: *The p_T distribution of the Z^0 boson as reconstructed from the momenta of the electrons in data (points) and Monte Carlo (solid histogram). The p_T distribution in the data is a bit broader than the one in the simulation. The number of events in the Monte Carlo sample has been normalized to the number of events in the data.*

14.1.1 Boson p_T Uncertainty

The distribution of the p_T of the Z^0 boson in the Monte Carlo directly affects the acceptance as it changes the momenta and angular distributions of the electrons. In the Monte Carlo the p_T of the Z boson is modelled according to a particular choice of input parameters, corresponding to the minimum of the χ^2 distribution between the Run I data and the MC events, as explained in section 6 and 13.1.1. The systematic uncertainty associated with this choice is studied by reweighting the default distribution, shown in Figure 57, using values $\pm 3\sigma$ away from the minimum for this set of parameters as indicated in Table 7[7]. The acceptances recalculated for each of these distributions are listed in Table 14. The difference between the acceptance of the reweighted distribution and the nominal value is taken as a systematic uncertainty. This results in a $\delta A_Z = 0.06\%$ variation in acceptance.

---

[7] The effect of PARP(93) is negligible, and thus not considered in this study.

Parameter	$A_Z(+3\sigma)$	$A_Z(-3\sigma)$	Δ A_Z(%)	$\Delta A_Z/A_Z$(%)
PARP(62)	11.0100	11.0138	0.0020	0.018
PARP(64)	11.0126	11.0109	0.0008	0.008
PARP(91)	11.0062	11.0175	0.0056	0.052
Total			0.0060	0.056

Table 14: *% change in $Z^0 \rightarrow e^+e^-$ acceptance for different p_T tuning parameters in PYTHIA. The bigger value is taken between the two, and the total uncertainty is obtained by adding the resulting ones in quadrature. The effect of changing PARP(93) is negligible and thus not considered in this study.*

14.1.2 PDF Uncertainty

Following the same procedure described in section 13.1.2, the relative systematic uncertainties in the $Z^0 \rightarrow e^+e^-$ acceptance are found to be

$$\sigma_{A_Z} \;=\; -2.03\% \quad \text{and} \quad +1.60\%,$$

corresponding to ΔA_Z = -0.224% and ΔA_Z = +0.176%.

14.1.3 p_T/E_T Scale/Resolution Uncertainty

The cut on the E_T of the electrons can be affected by the E_T scale and resolution correction factors applied in the data, as explained in section 5. The systematic uncertainties on these cuts was evaluated by varying the CEM energy scale and resolution separately and evaluating the change in acceptance. In Table 15 the energy scale variation up to 1% and the corresponding acceptances are given. A variation of ±0.3 is used in the final calculation of the uncertainty, which corresponds to a change of δA_Z = 0.008% in acceptance. The energy resolution has been moved up to 1.5%. In Table 16 the variations in resolution with the corresponding acceptances are summarised. The value of +1.5% is used in the final estimation of the uncertainty, resulting in a change of δA_Z = 0.005% in acceptance. In the same way as described above, the correction for the track p_T scale can affect the selection of the electrons through the p_T variable. This effect has been studied by scaling the track momentum by ±0.3%, corresponding to δA_Z = 0.005%, as reported in Table 17.

Energy scale change	$\mathbf{A_Z}$	$\boldsymbol{\delta}\mathbf{A_Z}$
+0.3%	11.0198%	+0.008%
Default	11.0118%	–
-0.3%	11.0065%	-0.006%

Table 15: *Effect on the acceptance due to the CEM energy scale variation. The 0.3% variation is used in the final calculation.*

Extra smearing of energy in MC	$\mathbf{A}_Z$	$\delta\mathbf{A_Z}$
+1.5%	11.0068%	+0.005%
Default	11.0118%	–

Table 16: *Effect on the acceptance due to the energy resolution variation. The value of 1.5% has been chosen in the final calculation.*

p_T **scale change**	$\mathbf{A}_Z$	$\delta\mathbf{A_Z}$
+0.3%	11.0171%	+0.005%
Default	11.0118%	–
-0.3%	11.0068%	-0.005%

Table 17: *Effect on the acceptance due to the scale of the track* p_T.

14.1.4 Material Uncertainty

An important source of systematic uncertainty is the amount of material in the detector simulation. In this analysis the $Z^0/\gamma^* \rightarrow e^+e^-$ Monte Carlo samples with ± 1.5% X_0 of copper, described in section III and 7, are used to determine the effect of the extra material on the acceptance.

Acceptance decreases quite significantly when the extra material is added, as shown in Table 13, where the acceptance is calculated after each cut for both Monte Carlo samples and the default. This decrease in acceptance is mainly due to the increase of external bremsstrahlung resulting in a lower p_T of the electrons.Figure 29(top) show the E/p distributions of the data, the default simulation, and the simulation with the extra material, as this quantity is directly affected by electron bremsstrahlung especially in the tail at higher E/p. The difference in behaviour of the three distributions in the region $1.5 < E/p < 2.5$ is indicative of the amount of material in the detector, as E/p in the tail is sensitive to the radiation length.

The systematic uncertainty due to precision with which the amount of the material in the detector is known is taken to be the largest difference between the default value and the values obtained with the two systematic samples. This reaults in a variation $\Delta A_Z = 0.15$ %.

14.2 Removing Drell-Yan Contributions from γ^* Exchange

A correction needs to be applied to the number of $Z^0 \rightarrow e^+e^-$ candidates to account for the fact that some of the e^+e^- pairs in the considered invariant mass window come from the continuum $p\bar{p} \rightarrow \gamma^* \rightarrow e^+e^-$ or the interference term between γ^* and Z^0, and not from Z^0 resonant production. The correction factor is obtained by the computation of the integrals $I_1 \equiv \int_{66}^{116} |Z^0 + \gamma|^2 dM$ and $I_2 \equiv \int_0^{\infty} |Z^0|^2 dM$ at $\sqrt{s}$=1.96 TeV using the PYTHIA generator; the number $\frac{I_2}{I_1} = 1.003$ is obtained, which is consistent with the most recent theoretical calculation at NNLO[47]

$$\frac{I_2}{I_1} = 1.004 \pm 0.001.$$

The ratio $\frac{I_2}{I_1}$= 1.004 ± 0.001 will be multiplied by the total number of Z^0/γ^* signal events.

14.3 Z Acceptance Summary

The systematic uncertainties on the Z acceptance are summarized in Table 18. The total systematic uncertainty on A_Z is -2.13%, +2.47%, with the main contributions coming from the modelling of the material and the PDFs.

source	**variation**	$\mathbf{\Delta A}_Z$	$\mathbf{\Delta A}_Z/\mathbf{A}_Z$
E_T^e scale	0.3% variation	0.008%	<0.073%
E_T^e resolution	1.5% extra smearing	0.005%	<0.045%
p_T^e scale	0.3% variation	0.005%	<0.048%
p_T modelling	$\pm 3\sigma$ variation	0.006%	0.056%
Material	±1.5% X_0	0.146%	1.33%
PDFs	CTEQ6L method	-0.22% , +0.176%	-2.03% , +1.60%
overall		-0.26% , +0.23%	-2.13% , +2.47%

Table 18: *Summary of the systematic uncertainties on the Z acceptance.*

Part VII

Efficiency

15 Calculation Method

The efficiency to detect a $W \rightarrow e\nu$ or $Z^0 \rightarrow e^+e^-$ decay that satisfies our kinematic and geometrical criteria is obtained from the formula shown in Equation 18.

$$\epsilon_{tot} = \epsilon_{z0} \times \epsilon_{trk} \times \epsilon_{rec} \times \epsilon_{id} \times \epsilon_{iso} \times \epsilon_{trg} \tag{18}$$

The ordering of the cuts, as depicted by their left to right order in the formula, is important. All of the efficiencies shown in this formula are efficiencies for the subset of $W \rightarrow e\nu$ and $Z^0 \rightarrow e^+e^-$ events that pass both the kinematic and geometric criteria of our sample and the requirements associated with each of the efficiency terms to the left of the term under consideration. For example, ϵ_{trg} is the trigger efficiency for $W \rightarrow e\nu(Z^0 \rightarrow e^+e^-$) events in our sample that have one(two) reconstructed lepton track(s) ($|z_0| < 60$ cm) and cluster(s) that pass all of the identification cuts and the isolation cut used in this analysis. These dependencies play an important role in properly accounting for correlations between different event selection criteria.

ϵ_{z0} is the fraction of $p\bar{p}$ collisions that occur within ± 60 cm of the center of the detector along the z-axis (parallel to the direction of the beams). Interactions that occur outside of this range are more difficult to detect and reconstruct due to the fact that the calorimeter towers are less projective from the outer part of the interaction area. The z-coordinate of the event vertex is taken from the impact parameter of the high-p_T lepton track along the z axis, z_0. Since the event selection criteria can bias our sample against events originating in the outer interaction region, ϵ_{z0} is measured from the vertex distribution in minimum bias events.

ϵ_{trk} is the efficiency for reconstructing the track of the high-p_T lepton in the COT, and ϵ_{rec} is the efficiency for matching the track to the associated EM cluster. Both efficiencies are based on events originating in collisions within ± 60 cm of the detector origin.

For tracks matched to clusters, ϵ_{id} is the efficiency of the electron identification criteria used to remove backgrounds. As this efficiency accounts for the set of cuts applied to the electron in the events, its value will be different for W events where one tight electron is required and for Z events, where two electrons with two different sets of cuts are required. The different calculations are discussed in section 17.

The same is valid for ϵ_{trg}, the trigger efficiency for one (in the case of $W \rightarrow e\nu$ events) or two ($Z^0 \rightarrow e^+e^-$ events) isolated, high quality electrons.

We discuss the measurement of each of these efficiency terms in the proceeding sections. Table 19 summarizes the results of these measurements and gives the resulting total efficiency for $W \rightarrow e\nu$ and $Z^0 \rightarrow e^+e^-$ events, as obtained from Equation 18.

Selection Criteria	Label	W Efficiency	Z Efficiency	Technique
Track z_0	ϵ_{z0}	0.950 ± 0.004	0.950 ± 0.004	Minimum Bias Events
Track Reconstruction	ϵ_{trk}	1.000 ± 0.004	1.000 ± 0.008	Silcon Tracks
Cluster Matching	ϵ_{rec}	0.998 ± 0.004	0.996 ± 0.008	$Z \rightarrow ee$
Electron Identification Cuts	ϵ_{id}	0.818 ± 0.008	0.859 ± 0.008	$Z \rightarrow ee$
Trigger	ϵ_{trg}	0.966 ± 0.001	0.999 ± 0.007	W NoTrack
Total	ϵ_{tot}	0.749 ± 0.009	0.810 ± 0.014	Product

Table 19: $W \rightarrow e\nu$ and $Z^0 \rightarrow e^+e^-$ Efficiency Calculation. The differences in the calculation methods for ϵ_{id} and ϵ_{trg} are explained in the corresponding sections.

16 Electron Trigger Efficiency

The high-E_T central electron trigger, ELECTRON_CENTRAL_18, is the primary trigger for $W \to e\nu$, and $Z \to ee$ cross section measurements. This section summarizes the results of studies of the trigger efficiency for high-E_T electrons (CDF note 6234 [48]) in data taken between March 2002 and May 2003. For more details please see CDF note 6234. Data used to measure the efficiency before the January 2003 shutdown (for winter 2003 conference results) used 4.8.4 REMAKE version of samples (offline release 4.9.1hpt3) and after the shutdown used 4.11.1 REMAKE version of samples. The studies were done in four run periods, three run periods before the January 2003 shutdown corresponding to different XFT requirements [49] and the fourth period for data taken after the shutdown.

Section 16.1 describes the triggers used for high-E_T electrons. The measurements of the tracking trigger efficiencies in different periods are described in section 16.2 and the measurements of the calorimeter trigger efficiencies are discussed in section 16.3. Section 16.4 summarizes and concludes the studies.

16.1 Trigger Definitions

The requirements for the ELECTRON_CENTRAL_18 path are

1. L1_CEM8_PT8 for Level 1
    - It requires a single trigger tower be found in the central region of the calorimeter with EM $E_T \geq 8$ GeV, Had/EM ≤ 0.125 (this requirement has no effect for towers with $E_T < 14$ GeV), and an XFT track pointing to that tower. The XFT tracks must have at least 10 (or 11) hits in at least 3 (or 4) layers and momentum $P_T \geq 8.34$ GeV/c. The hit and layer requirements vary for different run ranges and are summarized in Table 21.
2. L2_CEM16_PT8 for Level 2
    - It requires the L1_CEM8_PT8 trigger at Level 1 and the presence of a central cluster with EM $E_T \geq 16$ GeV and Had/EM ≤ 0.125. A track match must also occur between an XFT track of momentum $P_T \geq 8.34$ GeV/c and the cluster seed tower.
3. L3_CEM18_PT9 for Level 3
    - It requires a central EM offline cluster with $E_T > 18$ GeV, and Had/EM ≤ 0.125. A COT track with $P_T > 9$ GeV/c must also be matched to the EM cluster.
    - In L3_ELECTRON_CENTRAL_18_v-6 (version used for data after the January 2003 shutdown), several requirements were added to the Level 3 path including $L_{shr} < 0.4$, and CES-track matching in Z ($\Delta Z < 8$ cm). Other new features are

use of θ of the COT track to calculate the transverse component, instead of $z = 0$, and use of 3 hadronic towers instead of 2 in the Had/EM calculation.

A summary of the requirements for these high-E_T electron triggers at Level 1, Level 2, and Level 3 is presented in Table 20.

Trigger Name	Requirement	
L1_CEM8_PT8	ET_CENTRAL $\geq$ 8 GeV HAD_EM_CENTRAL $\leq$ 0.125 (this Had/EM cut has no effect for ET_CENTRAL $>$ 14 GeV)	
	XFT_PT $\geq$ 8.34 GeV/c XFT_LAYERS = 4 or $\geq$ 3	
L2_CEM16_PT8	L2_EM_ET $\geq$ 16 GeV L2_HAD_EM_RATIO $\leq$ 0.125 DCAS_HIGH_EM_CENTRAL_SEED $\geq$ 8 GeV DCAS_HIGH_EM_CENTRAL_SHOULDER $\geq$ 7.5 GeV	
	L2_TRACK_PT $\geq$ 8.34 GeV/c	
L3_ELECTRON_CENTRAL_18	Before Jan. 2003 Shutdown (Period 1 - 3)	After Jan. 2003 Shutdown (Period 4)
	CalorRegion = 0 cenEt $>$ 18 GeV cenHadEm $\leq$ 0.125 nEmObj $\geq$ 1	CalorRegion = 0 cenEt $>$ 18 GeV cenHadEm $\leq$ 0.125 nEmObj $\geq$ 1 lshr $\leq$ .4 cenDeltaZ $\leq$ 8 cm ZVert = 2 nTowersHadEm = 3
	cenTrackPt $\geq$ 9.0 GeV/c	

Table 20: *Requirements for the Level-1, Level-2, and Level-3 triggers used in the high-E_T electron trigger path, ELECTRON_CENTRAL_18*

.

The Level-1 track-trigger definitions have been changed in order to optimize trigger rates, efficiencies, and fake rates as the instantaneous luminosity increases. So far there are three different definitions of Level-1 track triggers for electrons, and we will associate them with Period 1, Period 2, and Period 3. Table 21 summarizes the requirements for the different run ranges and the luminosity for good runs within those ranges.

Many changes occurred during the January 2003 shutdown which could have an effect on the efficiency measurement. For example, the calorimeter ADC-to-MeV conversion factors were updated to reduce the difference between online electron energy and offline corrected electron energy. Also during this time period Level-3 tracking algorithms were changed to fix inefficiencies at high η. Level-3 track triggers use COT tracks produced by the "histogram-linking" (HL) algorithm. These tracks are required to have at least 1 stereo hit and 12 axial hits. Data before the January 2003 shutdown used an HL algorithm based on offline version 4.3 where tracks with a seed superlayer other than 8 was known to be inefficient. Data after the January 2003 shutdown use an HL algorithm based on offline version 4.8.4. Correspondingly we have chosen to define a fourth run period to study the efficiency under these new conditions.

16.2 Track Trigger Efficiencies

The W no-track trigger, W_NOTRACK, as detailed in Table 22, demands the same calorimeter requirements that are used for the high-E_T electron trigger, but does not require tracks associated with the EM clusters. Trigger efficiencies associated with tracks (XFT and Level-3 tracks) thus can be measured with events coming from the W no-track trigger. We start with events passing the W no-track trigger and a COT good run requirement (COT_OFFLINE = 1), and apply offline $W \rightarrow e\nu$ selection criteria to them. A W candidate is required to have an electron with $E_T > 25$ GeV and $\not{E}_T$ greater than 25 GeV. We reject candidates with seed towers in wedge 22 east during Period 1, for which the readout cables were swapped for a short period of time before the June 2002 shutdown. For this study, we use 5085 $W \rightarrow e\nu$ candidates in Period 1, 5066 in Period 2, 22203 in Period 3 and 27030 in Period 4. The track trigger efficiency measurements are relative to the offline tracking efficiency for high-E_T electrons, which is $(99.7^{+0.3}_{-0.8})\%$ using offline version 4.9.1.[50]

16.2.1 Level-1 Tracking Efficiency

The XFT trigger efficiencies with $P_T > 8.34$ GeV/c, L1_XFT_PT8, are measured by requiring the L1_CEM8_PT8 bit to be set:

$$\epsilon(L1\_XFT\_PT8) = \frac{\#\ of\ W\ candidates\ passing\ L1\_CEM8\_PT8}{\#\ of\ W\ candidates} \tag{19}$$

Since the EM8 bit has already fired in order to satisfy the W no-track trigger and the offline W cuts, measuring the efficiency of the L1_CEM8_PT8 trigger provides the L1_XFT_PT8

Period	Run Range	Luminosity (pb^{-1})	hits per superlayer	# of superlayers
1	141544-147868	10.2	≥ 10	4
2	147869-152629	18.5	≥ 10	≥ 3
3	152630-158732	43.5	≥ 11	≥ 3
4	158733-163527	51.4	≥ 11	≥ 3

Table 21: *Requirements for the XFT tracks for high-p_T electron triggers.*

efficiency. We find 4920 out of 5085 events in Period 1, 5015 out of 5066 events in Period 2, 21517 out of 22203 events in Period 3, and 26049 out of 27030 events in Period 4 passing the L1_CEM8_PT8 trigger. Thus we measure the L1_XFT_PT8 trigger efficiency to be $(96.76 \pm 0.25)\%$ in Period 1, $(98.99 \pm 0.14)\%$ in Period 2, $(96.91 \pm 0.12)\%$ in Period 3, and $(96.37 \pm 0.11)\%$ in Period 4.

We do not observe any dependence, within statistical uncertainties, on variables such as calorimeter isolation, track isolation, # of jets in the event, ΣE_T, H_T, ϕ and charge of the track. A significant inefficiency occurs for tracks near $\eta \sim 0$ as a result of the COT space bars and charge collection inefficiency due to the shorter particle path length. The η-dependent trigger efficiency is fit to

$$\epsilon(L1\_XFT\_PT8) = 1 - \frac{p0}{2\pi\sigma} \cdot exp(-\frac{\eta^2}{2\sigma^2}), \tag{20}$$

where $p0 = 0.054 \pm 0.004$ and $\sigma = 0.297 \pm 0.023$ for Periods 1 through 3 combined and $p0 = 0.179 \pm 0.006$ and $\sigma = 0.272 \pm 0.007$ for Period 4. Figure 58 (left) shows the measurements and fit result.

Trigger Name	Requirement	
L1_EM8_&_MET15	ET_CENTRAL or ET_PLUG $\geq$ 8 GeV HAD_EM_CENTRAL or HAD_EM_PLUG $\leq$ 0.125	
	MET $\geq$ 15 GeV	
L2_CEM16_L1_MET15	L2_EM_ET $\geq$ 16 GeV L2_HAD_EM_RATIO $\leq$ 0.125 DCAS_HIGH_EM_CENTRAL_SEED $\geq$ 8 GeV DCAS_HIGH_EM_CENTRAL_SHOULDER $\geq$ 7.5 GeV	
	L1 MET	$\geq$ 15 GeV
L3_W_NOTRACK_MET25	Before Jan. 2003 Shutdown (Period 1 - 3)	After Jan. 2003 Shutdown (Period 4)
	CalorRegion = 0 cenEt > 25 GeV cenHadEm $\leq$ 0.125 nEmObj $\geq$ 1	CalorRegion = 2 cenEt > 25 GeV cenHadEm $\leq$ 0.125 nTowersHadEm = 3 nEmObj $\geq$ 1 plugEt $\geq$ 25 GeV plugHadEm $\leq$ .125
	MetCut $\geq$ 25 GeV	

Table 22: Requirements for the Level-1, Level-2, and Level-3 triggers used in the W no-track trigger path, W_NOTRACK. Plug electrons are added during the January 2003 shutdown.

16.2.2 Level-2 Tracking Efficiency

Level 1 passes the XFT information to Level 2. We check whether there are any errors in getting the XFT information into Level 2, namely, whether the Level-2 PT8 bit is set when the Level-1 PT8 bit is set:

$$\epsilon(L2\_XFT\_PT8) = \frac{\#\text{ of W's passing L1\_CEM8\_PT8 \& L2\_XFT\_PT8}}{\#\text{ of W's passing L1\_CEM8\_PT8}} \tag{21}$$

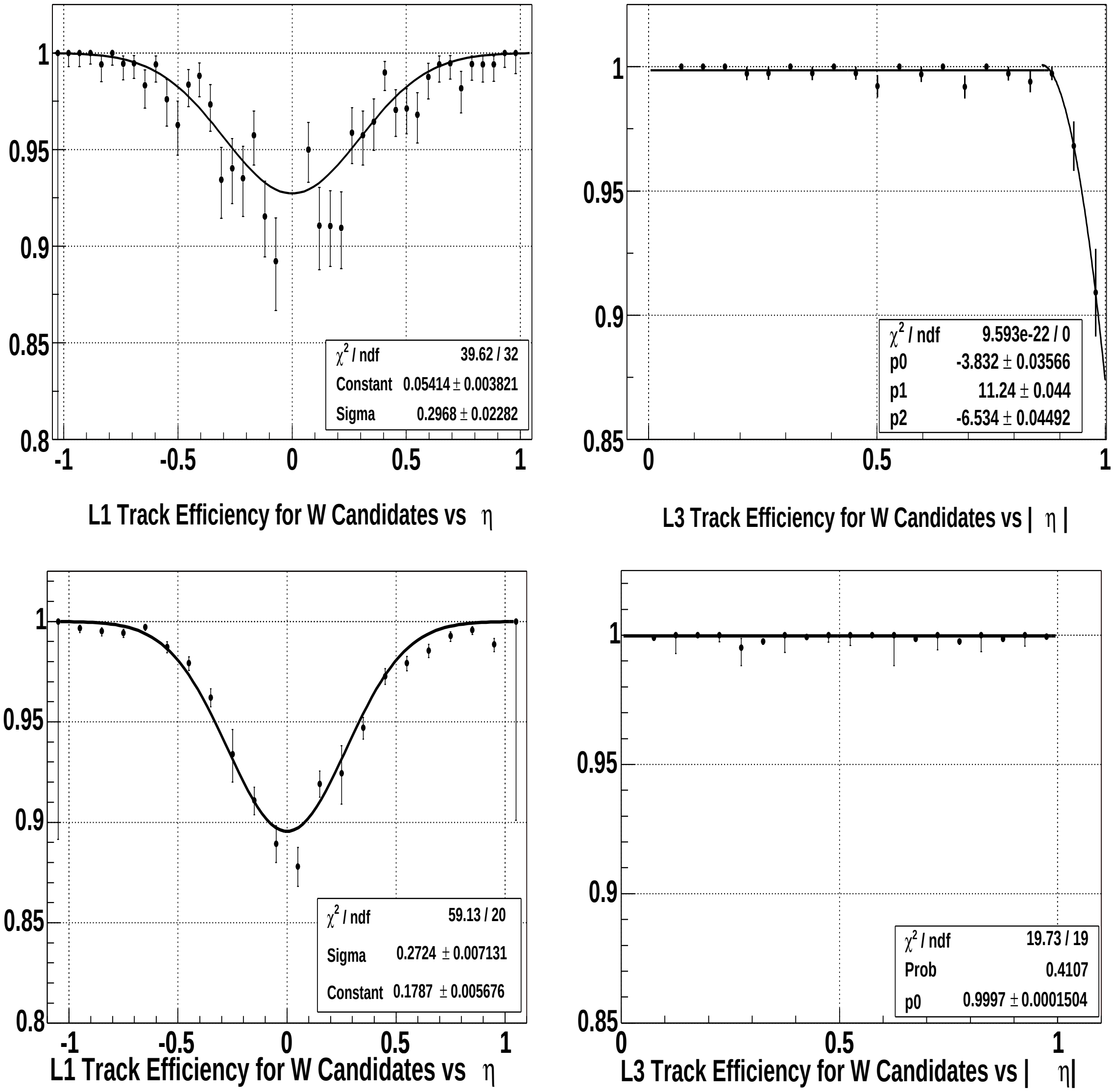

Figure 58: *Level-1 (left) and Level-3 (right) tracking efficiencies as a function of detector η measured by CES for Periods 1, 2, and 3 combined (top) and Period 4(bottom).*

We find seven events that failed passing the Level-1 information to Level 2, resulting in an efficiency of $(99.99 \pm 0.01)\%$.

16.2.3 Level-3 Tracking Efficiency

The Level-3 tracking efficiency is measured by requiring the L1_CEM8_PT8 and L2_CEM16_PT8 bits set and counting the W events with the Level-3 Electron 18 bit set:

$$\epsilon(L3\_PT9) = \frac{\#\text{ of W}'\text{s passing L1\_CEM8\_PT8 \& L2\_CEM16\_PT8 \& L3\_CEM18\_PT9}}{\#\text{ of W}'\text{s passing L1\_CEM8\_PT8 \& L2\_CEM16\_PT8}} \tag{22}$$

We find that 4900 events out of 4920 events pass the Level-3 track requirement, thus $(99.59 \pm 0.09)\%$, for the data in Period 1. In Period 2 and 3, 4962 events out of 5018 events and 21351 out of 21515 events pass the Level-3 track requirement resulting in efficiencies of $(98.94 \pm 0.14)\%$ and $(99.24 \pm 0.06)\%$, respectively. The η-dependent trigger efficiency for $|\eta| > 0.9$ in Periods 1 through 3 is fit to

$$\epsilon(L3\_PT9) = (-3.83 \pm 0.12) + (11.24 \pm 0.14) \cdot |\eta| + (-6.53 \pm 0.13) \cdot |\eta|^2, \tag{23}$$

as shown in Figure 58 (top right) and the average trigger efficiency for $|\eta| < 0.9$ is measured to be $(99.85 \pm 0.07)\%$.

In Period 4 we find that 26019 out of 26047 pass the Level-3 track requirement resulting in an efficiency of $(99.89 \pm 0.02)\%$. This increase in efficiency is expected due to the changes in the Level-3 tracking algorithm for high η (tracks with a seed superlayer other than 8) described in section 16.1. As expected, no η dependence is observed; see Figure 58.

Table 23: The track trigger efficiencies for the high-E_T electrons (trigger path name ELECTRON_CENTRAL_18).

Trigger	Efficiency			
	Period 1	Period 2	Period 3	Period 4
`L1 XFT PT8`	0.9676(25)	0.9899(14)	0.9688(20)	0.9637(12)
`L2 XFT PT8`	$1.0000(^{+00}_{-02})$	$1.0000(^{+00}_{-05})$	0.9999(01)	0.9999(01)
`L3 Tracking`	0.9959(09)	0.9894(14)	0.9924(10)	0.9989(02)
Total	0.9636(26)	0.9794(20)	0.9613(22)	0.9625(12)

Table 23 summarizes the average efficiencies of track triggers for the high-E_T electron trigger at Level 1, Level 2, and Level 3 for four data-taking periods. We are planning on adding the luminosity weighted averages to this table.

16.3 Calorimeter Trigger Efficiencies

16.3.1 Level-1 Calorimeter Efficiency

L1_CEM8 trigger selects events with trigger tower EM $E_T > 8$ GeV. If $E_T < 14$ GeV, it also requires the Had/EM value of the tower to be less than 0.125. We study the L1_CEM8 trigger by using the L1_EM8 trigger, which is decoupled from other requirements at Level 1.

The high-p_T inclusive muon sample, which requires one tight CMU or CMX muon without an isolation cut, provides an unbiased sample for calorimeter trigger studies. We select events which have CEM activity compatible with the L1_EM8 trigger. Events with significant PEM activity (any plug trigger tower with EM energy greater than 3 GeV) are vetoed in the sample in order to make the L1_EM8 trigger resemble the L1_CEM8 trigger. After the plug veto, the study sample before the January 2003 shutdown contains about 800,000 events, many of which have very high EM E_T calorimeter clusters. The sample after the January 2003 shutdown contains approximately 111,000 events.

We combine calorimeter towers into the trigger tower geometry and define the trigger tower energy to be the sum of the contributing towers' offline energies. We require Had/EM < 0.05 for the trigger tower. Events with at least one such trigger tower are selected and the trigger efficiency is measured by testing whether the selected events fire the L1_EM8 trigger bit. Figure 59 shows the efficiency as a function of the highest trigger-tower EM E_T in the event. We find the efficiency for $E_T^{trigger\ tower}$ between 8 and 14 GeV to be 99.5% for data before the January 2003 shutdown and 99.0% for data after the January 2003 shutdown. This inefficiency is due to differences in Had/EM values between trigger-level data and offline data. For $E_T^{trigger\ tower} > 14$ GeV where the trigger does not require a Had/EM cut, the trigger is fully efficient.

The effect of the inefficiency at $E_T^{trigger\ tower} < 14$ GeV on high E_T electrons is estimated by studying $E_T^{trigger\ tower}$ distribution of these electrons. Figure 60 shows the fraction of Z electrons that have $E_T^{trigger\ tower} < 14$ GeV as a function of electron E_T. We find that less than 1% of electrons with $E_T = 25$ GeV have $E_T^{trigger\ tower} < 14$ GeV, therefore the probability for electrons with $E_T = 25$ GeV to fail the L1_CEM8 trigger is less than $1\% \times 1\% = 0.01\%$. We thus conclude that the L1_CEM8 trigger efficiency for electrons with $E_T > 25$ GeV is 100%.

16.3.2 Level-2 Calorimeter Trigger Efficiency

The efficiency of the calorimeter portion of L2_CEM16_PT8 is measured using $W \to e\nu$ data coming from a backup trigger. We also check the efficiency for inclusive electrons as a crosscheck.

The L2_CEM16 trigger efficiency is measured with W events passing the W_NOTRACK_NO_L2 trigger. This trigger requires $E_T > 25$ GeV at Level 3, and is identical to the W_NOTRACK trigger with the exception that it uses L2_PS50_L1_CEM8_PT8 at Level 2. For the pre-January shutdown data we find that the L2_CEM16 trigger fires 100%

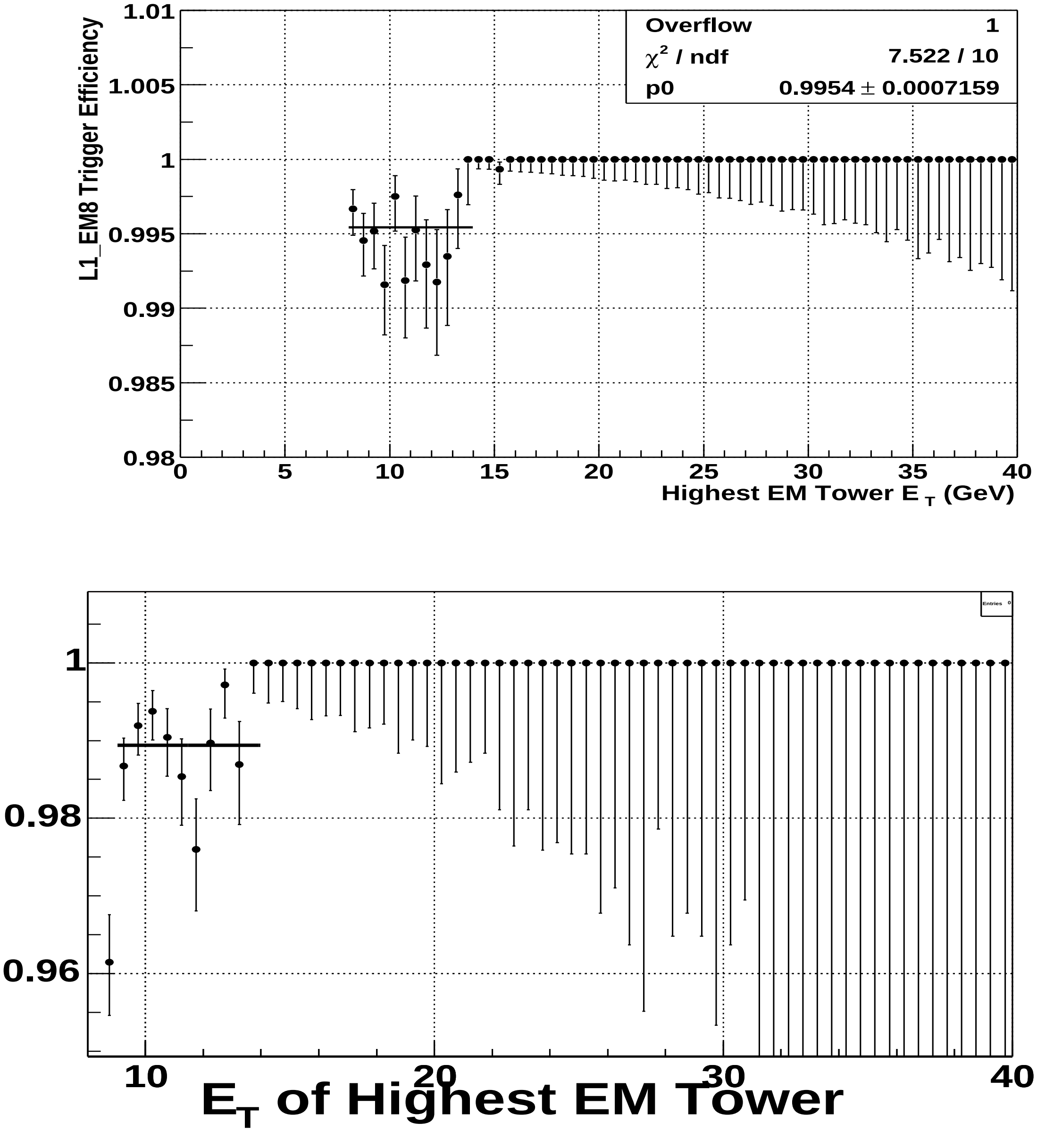

Figure 59: *The Level-1 EM8 calorimeter trigger efficiency in Periods 1, 2, and 3 combined (left) and Period 4 (right) as a function of the highest trigger-tower EM* E_T *in the event.*

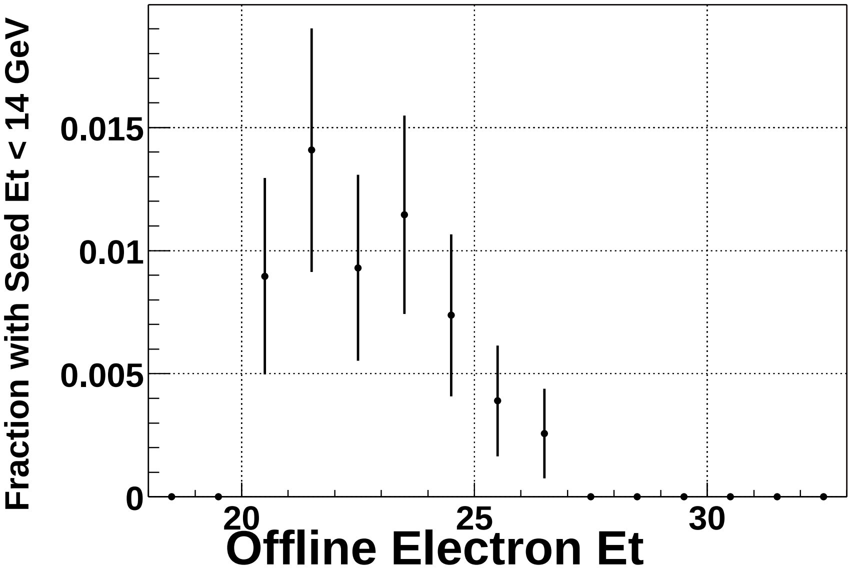

Figure 60: *The fraction of electron EM clusters with Level-1 trigger tower* $E_T < 14$ *GeV as a function of electron* E_T *in the* $Z \rightarrow e^+e^-$ *Monte Carlo sample.*

of the W candidates with electron $E_T > 25$ GeV, and for the post-shutdown data we find that 564 out of 565 events pass, corresponding to an efficiency of $(99.82^{+0.13}_{-0.27})\%$.

As a cross-check, we measure the efficiency of the Level 2 calorimeter clustering using inclusive electrons so we can measure the energy dependence. The ELECTRON_CENTRAL_18_NO_L2 trigger is used the measure the efficiency of the L2 trigger. The ELECTRON_CENTRAL_18_NO_L2 and ELECTRON_CENTRAL_18 have identical Level-1 and Level-3 triggers. The only difference is that at Level-2 ELECTRON_CENTRAL_18_NO_L2 auto-accepts a fraction of the Level-1 triggers rather than requiring Level-2 electron clusters.

We apply the baseline cuts with a lower E_T cut of 18 GeV and an isolation cut of less than 4 GeV. The E_T distribution of electron candidates and the resulting L2_CEM16 trigger efficiency are shown in Figure 61. The efficiency, $\epsilon(L2\_CEM16)$, is fitted to a function

$$\epsilon(L2\_CEM16) = 1 - p0 \cdot exp(-p1 \cdot E_T). \tag{24}$$

The L2_CEM16 trigger fires about 96% of electrons at $E_T \simeq 20$ GeV and the efficiency reaches up to 100% at $E_T \simeq 30$ GeV. Differences in the clustering algorithm, tower energy calculation, and tower energy corrections between Level 2 and offline contribute to the trigger inefficiency. A similar study with consistent conclusions was presented in Ref. [51]. The energy dependence measured in the inclusive electrons is consistent with the efficiency measured with the $W \rightarrow e\nu$ sample.

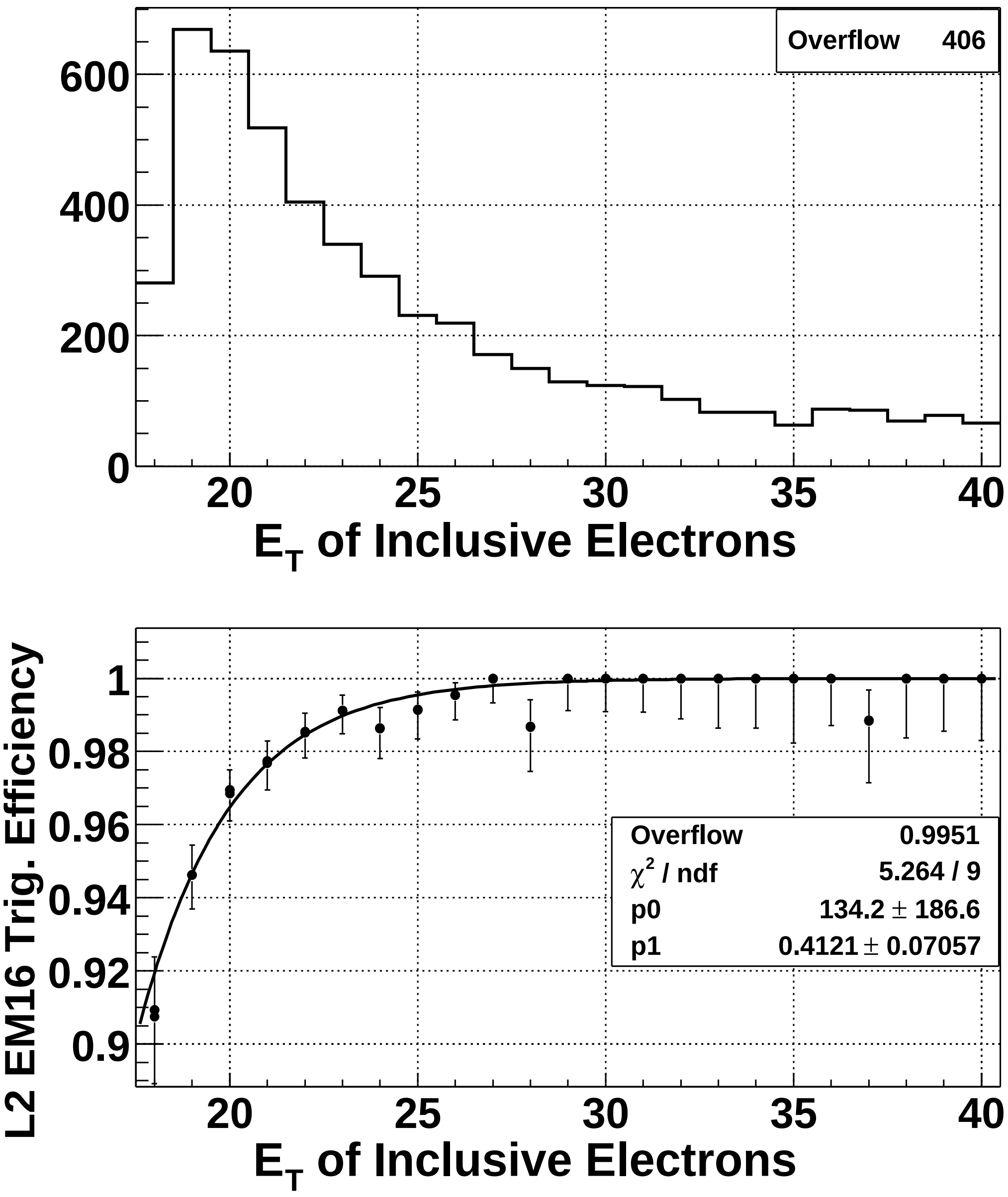

Figure 61: *E_T distribution of electron candidates from data before the January 2003 shutdown passing the L2_PS50_L1_CEM8_PT8 trigger and the "baseline cuts" (top) and L2_CEM16 trigger efficiency as a function of E_T (GeV) of electron candidates (bottom). No $\not\!\!E_T$ cut is applied to the events; however, there is a flat isolation requirement of less than 4 GeV.*

16.3.3 Level-3 Calorimeter Trigger Efficiency

We measure two aspects of the Level-3 trigger efficiency. Differences in the tower energy corrections could cause an inefficiency close to the trigger threshold, and new electron identification cuts applied in Period 4 could cause an inefficiency. To study the calorimeter portion of the L3_ELECTRON_CENTRAL_18 trigger we use a sample of inclusive, isolated electrons passing the ELECTRON_CENTRAL_8 path and the L2_CEM16_PT8 trigger. The trigger efficiency reaches 100% at $E_T \simeq 23$ GeV, and so is fully efficient for this analysis. We also check the affect of the new electron identification cuts on the efficiency. We did not find any differences in trigger efficiency in various trigger table versions. The Level-3 trigger efficiency is fully efficient for electrons with $E_T > 25$ GeV.

16.4 Summary

The measurements of the trigger efficiencies for W and Z electrons with $E_T > 25$ GeV passing the ELECTRON_CENTRAL_18 trigger, from a variety of data samples, are summarized in Table 24.

The average Level-1 and Level-3 track trigger efficiencies are measured to be $(96.76 \pm 0.25)\%$ and $(99.59 \pm 0.09)\%$ before the June 2002 shutdown, $(98.99 \pm 0.14)\%$ and $(98.94 \pm 0.14)\%$ between July 2002 and September 2002, $(96.91 \pm 0.12)\%$ and $(99.24 \pm 0.10)\%$ between September 2002 and January 2003, and $(96.37 \pm 0.11)\%$ and $(99.89 \pm 0.02)\%$ between January and June 2003. The differences are a result of the changes in the XFT track requirements and Level-3 tracking algorithms. [8] The η dependence of these triggers for each of the time periods has been measured. We measure the Level-2 track trigger efficiency to be 100% as expected. The Level-1 calorimeter trigger is consistent with 100% efficient. The Level-2 and Level-3 calorimeter triggers are E_T dependent, but fully efficient for electrons with $E_T > 25$ GeV.

Trigger	Efficiency			
L1_CEM8	$> 99.9\%$			
L2_CEM16	$(99.82^{+0.13}_{-0.27})\%$			
L3_CEM18	$> 99.9\%$			
	Period 1	Period 2	Period 3	Period 4
L1_XFT_PT8	0.9676(25)	0.9899(14)	0.9691(12)	0.9637(12)
L2_XFT_PT8	$1.0000(^{+00}_{-02})$	$1.0000(^{+00}_{-02})$	0.9999(01)	0.9999(01)
L3_PT9	0.9959(09)	0.9894(14)	0.9924(10)	0.9989(02)
Total Track Trigger	0.9636(26)	0.9794(20)	0.9613(22)	0.9625(12)

Table 24: *Summary of electron trigger efficiencies for various time periods (see section 16.1) for electrons with* $E_T > 20$ *GeV.*

---

[8] The exact definitions of the time periods are described in section 16.1.

In summary, the average tracking-trigger efficiency for triggering a single electron in the event is calculated by multiplying the values described in the previous paragraphs in each period, and weighting them by the integrated luminosities in the three periods. Its value is measured to be $\epsilon^W_{trig} = \langle \epsilon^e_{trig} \rangle = 96.6 \pm 0.1\%$.
In the selection of the $\mathrm{Z}^0 \rightarrow \mathrm{e}^+\mathrm{e}^-$ events, because there are two chances to fire the trigger, the average tracking trigger efficiency for at least one of the Z^0 electrons to fire the trigger is estimated to be

$$\epsilon^Z_{trig} = \langle \epsilon^{ee}_{trig} \rangle = \epsilon^e_{trig} + (1 - \epsilon^e_{trig})\epsilon^e_{trig} = \epsilon^e_{trig}(2 - \epsilon^e_{trig}) = (99.884 \pm 0.007)\%. \tag{25}$$

17 ID Efficiency

The identification efficiency for a central electron from W and Z decays in the fiducial region to pass the tight cuts, described in Section IV, is measured using the second leg of $Z^0 \rightarrow ee$ events. To isolate such a sample we select events with the following requirements:
- One tight central electron as defined in Table 25.
- A second electromagnetic cluster in the central region, with $E_T > 25$ GeV.
- An opposite sign track pointing to the second cluster, fiducial to CES, with $p_T > 10$ GeV and $|z_0| < 60$ cm. We call this object the *probe* electron.
- The invariant mass of the tight electron and the probe leg is required to be in a tight window around Z^0 mass (75, 105) GeV.

We refer to the number of central-central Z^0's passing these cuts as N_{CC}. Although Z→ *ee* events tend to be quite clean, multiple hadron jet events could mimic the signature of a Z event. Therefore we subtract the number of same-sign corrected QCD background, here “corrected” means that we explicitly take out the non-QCD same-sign events contribution due to the “tridents”. The number of non-QCD same-sign events is estimated using Monte Carlo. (See [23] or [35] for details).

Using the sample of N_{CC} events we apply, one by one, the “tight” central electron cuts on the second leg, and calculate the individual efficiencies of these cuts using the expression:

$$\epsilon^i_c = \frac{N_{Ti} + N_{TT}}{N_{CC} + N_{TT}}, \tag{26}$$

where N_{TT} is the number of events where both legs pass the tight central cuts and N_{Ti} is the number of events where one leg passes the tight cuts and the other passes the ith electron identification cut.

For the total efficiency, when both legs pass the tight cuts, the equation above becomes:

$$\epsilon_c = \frac{2N_{TT}}{N_{CC} + N_{TT}} \tag{27}$$

More details on the derivation of these expressions are provided in [23] or [35]. Table 26 summarizes the efficiency of each of the tight central cuts using this sample. The overall efficiency ϵ_C is $(81.8 \pm 0.8)\%$. Because of the correlations between different cuts ϵ_C is not simply the product of the individual cut efficiencies.

Variable	"tight" central	"loose" central	"probe" central
E_T	> 25GeV	> 25 GeV	> 25 GeV
p_T	> 10 GeV	> 10 GeV	> 10 GeV
Iso4	< 0.1	< 0.1	
E_{had}/E_{em}	< 0.055 + 0.00045*E	< 0.055 + 0.00045*E	
E/p	< 2.0 (or $p_T > 50$ GeV)		
Lshr	< 0.2		
$Q * \Delta x$	-3.0 cm, 1.5 cm		
$\|\Delta z\|$	< 3.0 cm		
χ^2_{strip}	< 10		
$\|z_0\|$	< 60.0 cm	< 60.0 cm	< 60.0 cm
COT Track quality	3 axial and 3 stereo SL with at least 7 hits each	3 axial and 3 stereo SL with at least 7 hits each	
FIDELE	1 (fiducial in CEM)	1 (fiducial in CEM) opposite charge	1 (fiducial in CEM) opposite charge

Table 25: $Z^0 \to e^+e^-$ Selection Cuts. We also require $75\,GeV < M_{ee} < 105\,GeV$.

Variable	MC ($E_T > 25$ GeV)	Data ($E_T > 25$ GeV)
	Nth eff. (%)	Nth eff. (%)
E_{had}/E_{em}	98.82 ± 0.04	99.0 ± 0.3
E/P	90.50 ± 0.12	91.2 ± 0.5
Iso4	97.40 ± 0.07	97.0 ± 0.4
Lshr	97.02 ± 0.07	98.9 ± 0.3
$Q * \Delta x$	98.33 ± 0.05	98.2 ± 0.3
$\|\Delta z\|$	99.44 ± 0.03	99.0 ± 0.2
χ^2_{strip}	98.09 ± 0.06	96.3 ± 0.4
# Axial & Stereo SL	98.92 ± 0.04	97.0 ± 0.3
Total ϵ_T	82.42 ± 0.17	81.8 ± 0.8
Total ϵ_L	95.32 ± 0.09	93.4 ± 0.5

Table 26: Efficiency of the tight central electron identification cuts (ϵ_c) using both Monte Carlo and Z data samples, for $E_T > 25$ GeV. All uncertainties shown are statistical.

For the case of the W events selection, the efficiency ϵ^W_{id} appearing in the formula 18 is just the efficiency of the tight electron selection, ϵ_T, as it is the only electron in the event.

In the case of the Z events, the efficiency ϵ_{id}^{Z} in the formula on page 81 is a function of the two efficiencies, one for the tight electron selection, ϵ_T, the same as for the W, and the other for the loose electron selection, ϵ_L, as listed in Table 3; that is,

$$\epsilon_{id}^{Z} = \epsilon_T(2\epsilon_L - \epsilon_T). \tag{28}$$

The total selection efficiency of $Z^0 \rightarrow e^+e^-$ events, consisting of one tight electron and one loose electron, is

$$\epsilon_{id}^{Z} = \epsilon_T(2 \cdot \epsilon_L - \epsilon_T) = (85.9 \pm 0.8)\%. \tag{29}$$

The efficiency for the selection of $W^\pm \rightarrow e^\pm\nu$ events is

$$\epsilon_{id}^{W} = \epsilon_T = (81.8 \pm 0.8)\%. \tag{30}$$

18 Track Reconstruction Efficiency

The track reconstruction efficiency is defined as the efficiency for the offline track reconstruction algorithm to reconstruct a track of a high-p_T electron or muon. To measure it we identify a clean and unbiased sample of charged particles with high purity. Decays of $W \rightarrow e\nu$ can be identified using only calorimeter information and offer such a sample. The tracking efficiency will then be the fraction of such events which have a COT track pointing to the "electron" cluster. We begin with the W no-track sample, which consist of events with $\not\!\!E_T > 25$ GeV and at least an electromagnetic cluster with $E_T > 20$ GeV. To remove the backgrounds such as out-of time cosmic-rays, beam-related splashes, photons or leading π^0's which shower early in the detector, we apply the following selection requirements:

- $E_T > 25$ GeV, $p_T^W > 10$ GeV.
- no extra jets in the event: $N_{jet} = 0$, where for jet we use cone-algorithm with R = 0.7 and $E_{min}^{jet} = 3$ GeV, excluding the electron candidate EM cluster.
- fiducial cuts: $|\eta_{EMcluster}| <1.05$, $z_{CES} > 0$ cm, $|x_{CES}| < 22$ cm.
- electron id: $E_{had}/E_{em} < 0.05$, Lshr < 0.2, $\chi^2_{strip} < 4$, $\chi^2_{wire} < 4$ and iso(0.7) < 4 GeV.
- CPR match: $|x_{CPR} - x_{CES}| < 4$ cm.

All tracks considered are COT defTracks, required to extrapolate within 5 cm of the seed tower to be considered a match to the EM cluster. In order to further reduce track-less background a reconstructed track in the silicon detector, pointing to the EM cluster,independent of the COT is required. We find 1368 candidate events with a matching silicon track, and 1363 of these have a matching COT track. This yields a tracking efficiency of $\epsilon_{COT}(Si)$ = 99.63 $^{+0.35}_{-0.40}$ %, where the statistical and systematic uncertainties have been included (see [50] for details). There are two main sources of systematic uncertainties considered: the selection of silicon stand-alone tracks (SISA) which affects the silicon tracks fake rate, and the possibility of correlated failures of the COT and the silicon detector.

Using a $W \rightarrow e\nu$ Monte Carlo sample, the MC tracking efficiency is determined as $\epsilon_{COT}(Si)$ = 99.66 $^{+0.15}_{-0.24}$ %, consistent with the data estimate. The ratio of the COT tracking efficiencies in data and Monte Carlo, R_{COT}, is

$$R_{COT} = 1.000 \pm 0.004, \tag{31}$$

where statistical and systematic uncertainties have been included. A careful scan of the failing events reveals that in nearly every case a SISA track is pointing to the "electron" cluster. The track shares its silicon hits with a soft electron spiraling off, such that it does not match the "electron" cluster and no matching COT track will be found. Therefore the tracking inefficiency is mainly due to bremsstrahlung radiation: the SISA track points into the photon direction, while the COT track follows the soft electron direction.

19 Central EM Cluster Reconstruction Efficiency

The EM cluster reconstruction efficiency is defined as the efficiency for the offline EM cluster reconstruction algorithm to reconstruct a cluster corresponding to a high-p_T electron. Possible inefficiencies in this procedure might come from detector failures, such as the presence of dead towers in the calorimeter or proton beam splashes, or from inefficiencies in the code or in the selection criteria. In order to measure it we use the $Z^0 \rightarrow e^+e^-$ data and Monte Carlo samples defined in Part III and II.1[9] respectively. In both cases we started selecting a "very-tight"high-p_T electron (VTE) from the initial sample. This electron has been selected according to the criteria listed in table 2, but with tightened Isolation and Lshr cuts of

- Iso Frac (Δ R = 0.4) < 0.05;
- Lshr < 0.0.

This is done to reduce the background and insure that the electron is a good electron coming from the Z. Among the events with a VTE, we select events with a "tight track", satisfying the criteria listed in table 27 and having the vertex within 5 cm from the z_0 vertex of the track associated to the VTE. In addition, the invariant mass of the tight track and the very-tight electron has to be within the 80-100 GeV/c^2 window. At this point we are reasonably

Variable	Cut
fiduciality	fiducial at the CES
p_T	> 15 GeV
$\|z_0\|$	< 60.0 cm
# Stereo SL	$= 4$ with ≥ 8 hits
# Axial SL	$= 4$ with ≥ 8 hits

Table 27: Criteria used in the selection of the tight track as defined in the text.

---

[9] This calculation used data collected from March 2002 (run 141544) until May 2003 (run 163527), corresponding to roughly 100 pb^{-1} of data.

confident that the events we selected with one VTE and one tight-track ($N_{(VTE+TT)}$) are real $Z^0 \rightarrow e^+e^-$ events. To calculate the efficiency, we select a subsample of $N_{(VTE+TT)}$ by requiring the presence of a CdfEmObject in the event, with a track which falls within a cone of $\Delta R < 0.4$ from the tight-track (the number of such events is indicated as $N_{(VTE+TT+EMC)}$). The EM cluster reconstruction efficiency ϵ_{EMC} is thus defined as $\frac{N_{(VTE+TT+EMC)}}{N_{(VTE+TT)}}$. We estimated

- $\epsilon^{MC}_{EMC} = \frac{8067}{8128} = (\ 99.2 \pm 0.1\ )\%$
- $\epsilon^{data}_{EMC} = \frac{600.0}{605.9} = (\ 99.0 \pm 0.4\ )\%$

where the number of events in the data has been corrected for the background estimated from same sign events in the same way as it has been done in section 12.1. Only the statistic uncertainties have been included in the calculation. The ratio of the EM cluster recontruction efficiencies in the data and MC, R_{EMC}, is thus

$$R_{EMC} = 0.998 \pm 0.004. \tag{32}$$

A careful scan of the failing events is currently on-going [52].

20 Vertex Efficiency

The requirement that the event vertex fall within ±60 cm of the center of CDF limits the event acceptance to a portion of the full luminous region of $p\bar{p}$ collisions while the luminosity reported by the CLC detector is over the full luminous region in z. Minimum bias data are used to measure the longitudinal profile of the $p\bar{p}$ luminous region, and the Tevatron $p\bar{p}$ longitudinal beam profile function is used to estimate the fraction of the luminous region at large z. The Tevatron $p\bar{p}$ beam luminosity function [53] is:

$$\frac{d\mathcal{L}(z)}{dz} = N_p N_{\bar{p}} \frac{1}{\sqrt{2\pi}\sigma_z} \frac{\exp\left(-z^2/2\sigma_z^2\right)}{4\pi\sigma_x(z)\,\sigma_y(z)}, \tag{33}$$

where z is Z_{vtx}, $N_{p,\,\bar{p}}$ are the p, $\bar{p}$ fluxes, and

$$\sigma_x^2(z) \simeq \frac{1}{6\pi\gamma}\beta_x(z)\,\epsilon_x \tag{34}$$

$$\sigma_y^2(z) = \frac{1}{6\pi\gamma}\beta_y(z)\,\epsilon_y \tag{35}$$

$$\beta(z) = \beta^*[1 + (\frac{z - z_0}{\beta^*})^2] \tag{36}$$

are the transverse beam widths. This function is simplified by assuming $\beta_x^* = \beta_y^*$, but allowing two independent z_0's:

$$\frac{d\mathcal{L}(z)}{dz} = N_0 \frac{\exp\left(-z^2/2\sigma_z^2\right)}{\sqrt{[1 + (\frac{z-z_{01}}{\beta^*})^2][1 + (\frac{z-z_{02}}{\beta^*})^2]}} \tag{37}$$

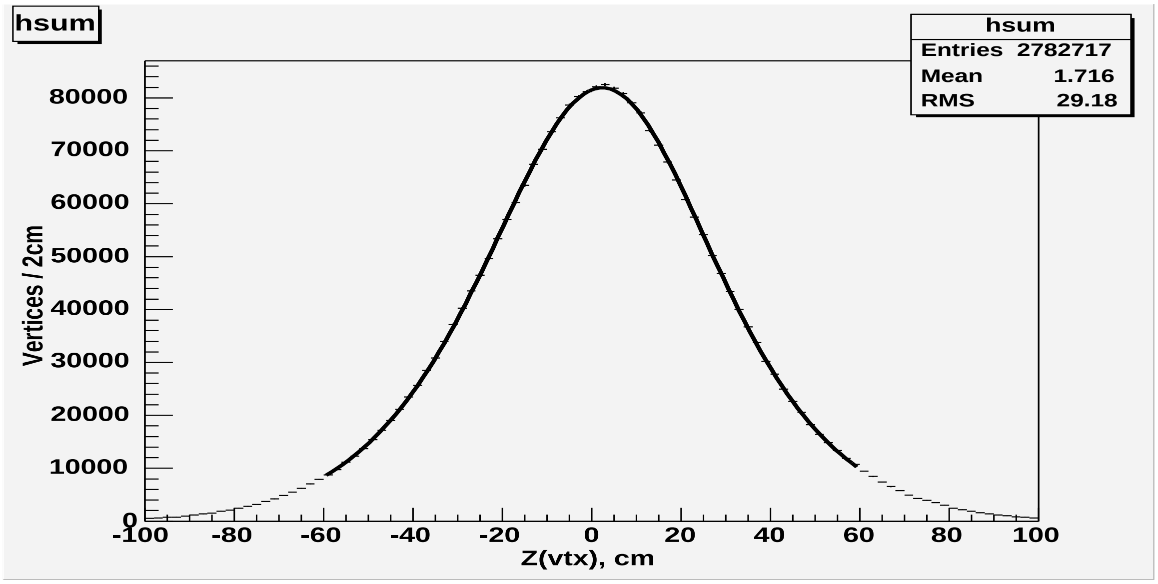

Figure 62: *The measured* Z_{vtx} *distribution. The units are cm and there are 100 bins. The curve is the fit to the luminosity function for* $|z| < 60$ *cm, and it has* $\chi^2 = 119$.

The distribution of the $p\bar{p}$ interaction point(s) along the beam-line z-axis for min-bias events taken in the same period as the cross-section data is shown in Fig. 62.

The min-bias data are weighted to have the same run-by-run integrated luminosity as the cross section data. The Z_{vtx} distribution shown in Fig. 62 has some biases at large values of z because of increased contamination from non-$p\bar{p}$ interactions such as beam-gas interactions and the falloff of the COT track acceptance. These difficulties are avoided by only fitting the measured Z_{vtx} distribution to $d\mathcal{L}(z)/dz$ within $|z| < 60$ cm, where the non-$p\bar{p}$ interactions are small, and the COT track acceptance is high and uniform. The $|Z_{\text{vtx}}| \leq 60$ cm cut acceptance is calculated using,

$$\epsilon(|z| < 60) = \frac{\int_{-60}^{+60} [d\mathcal{L}(z)/dz]\, dz}{\int_{-\infty}^{+\infty} [d\mathcal{L}(z)/dz]\, dz} \,. \tag{38}$$

This acceptance has been evaluated for the full data set and for sub-samples of the data set. The sub-sample analysis indicates that there are slight differences in the z-profiles of the $p\bar{p}$ collisions with time. The maximum shift in $\epsilon(|z| < 60)$ is 0.006, and half of this is taken as an estimate of the systematic error related to shifts in the beam z profile.

The luminosity acceptance of the $|Z_{\text{vtx}}| < 60$ cm cut for the cross section dataset is: $\epsilon(|Z_{\text{vtx}}| < 60)$:

$$\epsilon_{\text{vtx}} = 0.950 \pm 0.002\,(\text{stat}) \pm 0.003\,(\text{syst})\,.$$

The statistical uncertainty is from the fit errors. Additional details can be found in CDF6660 [54].

Part VIII

Results

In this chapter all the elements estimated in the previous sections are combined in the calculation of the Z and W cross sections, in sections 21 and 22.

21 W cross section estimation

We estimate the $W \rightarrow e\nu$ cross-section using Run 2 data and compare it to the Run 1 measurement. The cross-section is:

$$\sigma \cdot B(p\bar{p} \rightarrow W \rightarrow e\nu) = \frac{N_W - N_{BG}}{A_W \cdot \epsilon(Z_{vtx} < 60) \cdot \epsilon_c \cdot \epsilon_T \cdot \mathrm{R}_{COT} \cdot \mathrm{R}_{EMC} \cdot \int \mathcal{L}dt}, \tag{39}$$

where N_W is the number of $W \rightarrow e\nu$ candidate events and N_{BG} is the estimated number of background events. A_W is the kinematic and geometric acceptance taken from Monte Carlo. $\epsilon(Z_{vtx} < 60)$ is the efficiency of the $|Z_{vtx}| \leq 60$ cm cut. ϵ_c is the central electron cut efficiency, ϵ_T is the trigger efficiency, R_{COT} is the COT track reconstruction data/MC scale factor, R_{EMC} is the central EM cluster reconstruction data/MC scale factor and $\int \mathcal{L}dt$ is the integrated luminosity.

We have:

$$\begin{aligned}
N_W &= 37584 \\
N_{BG} &= 1656 \pm 52(stat) \pm 295(syst) \\
A_W &= (23.895 \pm 0.03(stat)^{+0.34}_{-0.39}(syst))\% \\
\epsilon(Z_{vtx} < 60) &= (95.0 \pm 0.2(stat) \pm 0.3(syst))\% \\
\epsilon_c &= (81.8 \pm 0.8(stat) \pm 0.2(syst))\% \\
\epsilon_T &= (96.6 \pm 0.1(stat))\% \\
R_{COT} &= (100.0 \pm 0.4)\% \\
R_{EMC} &= (99.8 \pm 0.4)\% \\
\int \mathcal{L}dt &= (72.0 \pm 4.3(syst))\, pb^{-1}
\end{aligned}$$

Finally, we measure

$$\sigma \cdot B(p\bar{p} \rightarrow W \rightarrow e\nu) = (2.781 \pm 0.015_{\mathrm{stat}}{}^{+0.057}_{-0.062}{}_{\mathrm{syst}} \pm 0.167_{\mathrm{lum}})\ \mathrm{nb}. \tag{40}$$

Theorists W. James Stirling *et al.* recently worked on an improved calculation of the $W \rightarrow e\nu$ cross-section, taking account of the higher Tevatron collider energy. Table 28 shows their results for $\sqrt{s} = 1.8$ TeV compared to $\sqrt{s} = 1.96$ TeV. The higher energy

Corrections	$\sqrt{s}$ (TeV)	$\sigma \cdot B(p\bar{p} \to W \to e\nu)$ (nb)
LO	1.80	1.763
NLO	1.80	2.411
NNLO	1.80	2.501
LO	1.96	1.939
NLO	1.96	2.639
NNLO	1.96	2.731

Table 28: Improved calculation of $W \to e\nu$ cross-section by W. James Stirling *et al.* for both $\sqrt{s} = 1.8$ TeV and $\sqrt{s} = 1.96$ TeV.

increases the W event rate by 9 %. An error of ± 0.002 is assigned on the NNLO result which reflects the small residual uncertainty in the NNLO splitting functions. No other parameters have been changed since the previous calculation [55]. Additional uncertainties will come from the PDF's and from the measurement of $B(W \to e\nu)$. They are currently studying the PDF uncertainty on these numbers.

At $\sqrt{s} = 1.96$ TeV, the prediction from the Run 1 analysis [56] is (scaling up by 9 %):

$$\sigma \cdot B(p\bar{p} \to W \to e\nu) \quad = \quad (2.72 \pm 0.13)\,\text{nb}. \tag{41}$$

Our analysis yields a value that is within 1 σ of the expected value from the Run 1 measurement and the theoretical prediction.

22 Z cross section estimation

The cross section $\sigma(\bar{\text{p}}\text{p} \to \text{Z}^0)$ times the branching ratio $\text{Br}(\text{Z}^0 \to \text{e}^+\text{e}^-)$ is calculated using the expression

$$\sigma_Z \cdot B(\text{Z}^0 \to \text{e}^+\text{e}^-) = \frac{I_2}{I_1} \cdot \frac{\text{N}^{candidates}_{Z/\gamma^*} - \text{N}^{background}_{\text{Z}}}{\text{A}_Z \cdot \epsilon^Z_{trig} \cdot \epsilon_{zvertex} \cdot \epsilon^Z_{id} \cdot \int \mathcal{L}dt \cdot \text{R}^2_{COT} \cdot \text{R}^2_{EMC}} \tag{42}$$

where

- $\text{N}^{candidates}_{Z/\gamma^*} = 1730 \pm 42(stat.)$;
- $\text{N}^{background}_{\text{Z}} = 4.5 \pm 7.1$;
- $\text{A}_Z = (11.01^{+0.23}_{-0.27})\%$;
- $\epsilon^Z_{trig} = (99.884 \pm 0.007)\%$;
- $\epsilon_{zvertex} = (95.0 \pm 0.4)\%$;

- $\epsilon_{id}^{Z} = (85.9 \pm 0.8)\%$;
- $\mathrm{R}_{COT} = (1.000 \pm 0.004)$;
- $\mathrm{R}_{EMC} = (0.998 \pm 0.004)$;
- $\int \mathcal{L}dt = (72.0 \pm 4.3)\ \mathrm{pb}^{-1}$;
- $\frac{\mathrm{I}_2}{\mathrm{I}_1} = 1.004 \pm 0.001$.

Substituting these values

$$\begin{aligned} \sigma_Z \cdot Br(\mathrm{Z}^0 \to \mathrm{e}^+\mathrm{e}^-) &= 269.3 \pm 6.5(stat.)^{+6.9}_{-7.6}(syst.) \pm 16.2(lum.)\,\mathrm{pb} \quad (43) \\ &= (269.3^{+18.7}_{-19.0})\ \mathrm{pb}. \quad (44) \end{aligned}$$

In Table 29 these values are compared with those obtained in Run Ia, where the luminosity is taken from [57] and the other quantities are taken from [45][10]. The uncertainty on the luminosity measurement is dependent on the uncertainty on the p$\bar{\mathrm{p}}$ inelastic cross section. The two measurements of this cross section differ from each other of about 6%; to be conservative, in Run II the uncertainty on the luminosity has been increased to cover this number; in Run I the CDF measurement was used[58], which results in a smaller uncertainty. An update from Run Ia and Run Ib, but without a detailed breakdown of the systematic errors, is given in [59]. The measured Run Ia+Ib value is

$$\begin{aligned} \sigma_Z \cdot Br(\mathrm{Z}^0 \to \mathrm{e}^+\mathrm{e}^-) &= (253 \pm 4(stat. + syst.) \pm 10(lum.))\,\mathrm{pb} \\ &= (253 \pm 11)\,\mathrm{pb}; \end{aligned}$$

scaling this value up by 9% for the $\sqrt{s}$ dependence, it becomes

$$\sigma_Z \cdot Br(\mathrm{Z}^0 \to \mathrm{e}^+\mathrm{e}^-) = (276 \pm 12)\,\mathrm{pb}, \quad (45)$$

which is consistent with the measurement reported here.

W. James Stirling *et al.*[60] have worked on an improved calculation of the $\mathrm{W} \to \mathrm{e}\nu$ and $\mathrm{Z}^0 \to \mathrm{e}^+\mathrm{e}^-$ cross-sections, including the higher colliding energy at the Tevatron. The predicted value at $\sqrt{s} = 1.96$ TeV with NNLO corrections is (250.5 ± 3.8) pb for $\mathrm{Z}^0 \to \mathrm{e}^+\mathrm{e}^-$ (where the uncertainty comes primarily from the uncertainty on the PDF calculation) which agrees well with the measurement reported here and with the more recent theoretical calculation [47] of (252 ± 9) pb. The calculation of the cross sections in this paper is based on the zero-width approximation approach described in [61; 62]. The estimation of the uncertainty from the PDFs on these total cross sections has been performed with the NLL CTEQ6 and MRST2001E error PDFs sets according to the prescriptions in [63; 64], obtaining the relative uncertainties of 3.5% and 1.1% respectively. To be conservative, the CTEQ6 errors are used. Table 30

---

[10] Note that the kinematic cuts in Run Ia are looser than in the ones in Run IIa.

Variable	**Run Ia**	**Run IIa**
$\mathcal{L}(\text{pb}^{-1})$	19.7 ± 0.7	72.0 ± 4.3
$\text{N}_Z^{candidates}$ (CC) in $66< M_{ee} <116$ GeV$/c^2$	529	1730
$\text{N}_\text{Z}^{background}$ (CC) in $66< M_{ee} <116$ GeV$/c^2$	1 ± 1	4.5 ± 7.1
A_Z^{CC}	$(15.2 \pm 1.2)\%$	$(11.01 \pm^{+0.23}_{-0.27})\%$
ϵ_T	$(84.5 \pm 1.2)\%$	$(81.8 \pm 0.7)\%$
ϵ_L	$(91.7 \pm 0.8)\%$	$(93.4 \pm 0.5)\%$
ϵ_{trig}	$(89.2 \pm 0.3)\%$	$(99.884\pm0.007)\%$
$\epsilon_{Z_{vtx}}$	$(95.5 \pm 1.1)\%$	$(95.0 \pm 0.4)\%$
$\frac{\text{I}_2}{\text{I}_1}$	1.005 ± 0.002	$1.004 \pm 0.001\%$
$\sqrt{s}(p\bar{p})$	1.8 TeV	1.96 TeV
$\sigma_Z \cdot Br(\text{Z}^0 \to \text{e}^+\text{e}^-)$ (pb)	248 ± 25	$269 \pm ^{+18.7}_{-19.0}$

Table 29: *Parameters involved in the* $\text{Z}^0 \to \text{e}^+\text{e}^-$ *cross-section calculation in Run Ia and Run IIa. Note that the kinematic cuts in Run Ia are looser than in the ones in Run IIa.*

Corrections	$\sqrt{s}$ (TeV)	$\sigma_Z \cdot Br(\text{Z}^0 \to \text{e}^+\text{e}^-)$(nb)
LO	1.80	0.1607
NLO	1.80	0.2204
NNLO	1.80	0.2297
LO	1.96	0.1763
NLO	1.96	0.2407
NNLO	1.96	0.2502

Table 30: *Improved calculation of* $\text{Z}^0 \to \text{e}^+\text{e}^-$ *cross-section by W.James Stirling et.al. for both* $\sqrt{s}$ *= 1.8 and* $\sqrt{s}$ *= 1.96 TeV.*

shows the recent calculations of Stirling *et al.* [60] for $\sqrt{s}$ = 1.8 TeV compared to $\sqrt{s}$ = 1.96 TeV. The higher energy increases the Z^0 cross section by ∼ 9%. The uncertainties reflect the 1.5% uncertainty on the calculation of the PDFs [65]. The other parameters have been updated since the previous calculation [55] to incorporate the latest results from LEP. For a complete list of the parameters used in this calculation see Table 31. Figure 63 shows this measurement compared with the other measurements in the literature and with the theoretical predictions from Stirling *et.al.*.

Parameter	**value**
$Br(\mathrm{Z}^0 \rightarrow \mathrm{e}^+\mathrm{e}^-)$	0.033658
$Br(\mathrm{W}^0 \rightarrow \mathrm{e}\nu^-)$	0.0168
M_W	80.4230
M_Z	91.1876
$\sin^2_{\theta_W}$	0.23143
G_F	1.16639
W coupling: $\sqrt{2} \cdot G_F \cdot M_W^2$	yes
W coupling: $\pi \cdot \frac{\alpha}{sin^2_{\theta_W}}$	no
Z coupling: $\sqrt{2} \cdot G_F \cdot \frac{M_Z^2}{4}$	yes
Z coupling: $\pi \cdot \frac{\alpha}{4sin^2_{\theta_W}} \cdot cos^2_{\theta_W}$	no
CKM elements:	
V_{ud}	0.9734
V_{us}	0.2196
V_{ub}	0.0036
V_{cd}	0.224
V_{cs}	0.996
V_{cb}	0.0412

Table 31: *List of parameters used in the theoretical calculation of the NNLO* $\mathrm{Z}^0 \rightarrow \mathrm{e}^+\mathrm{e}^-$ *and* $\mathrm{W}^\pm \rightarrow \mathrm{e}^\pm\nu$ *cross sections.*

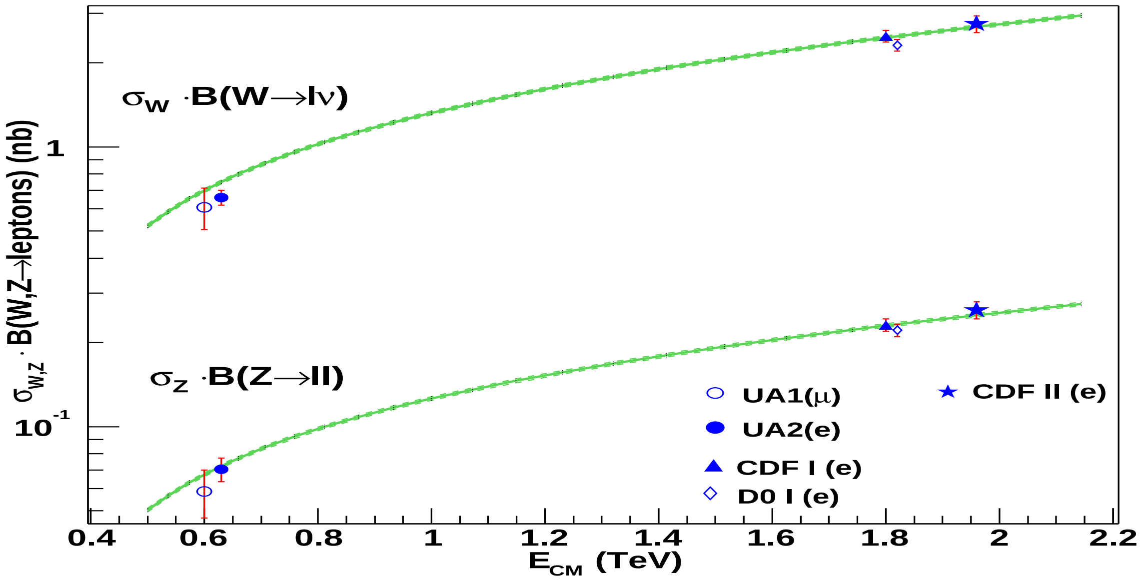

Figure 63: $Z \rightarrow \ell^+\ell^-$ *and* $W^\pm \rightarrow \ell^\pm\nu$ *cross section measurements as a function of the center of mass energy* $\sqrt{s}$ *for this measurement (indicated with the star) compared with other measurements in literature. The solid line corresponds to the standard model calculation from [55].*

23 Estimation of the Ratio of Cross Sections

The ratio of the W and Z cross sections is an important test of the Standard Model. A measurement of this ratio precisely tests the branching ratio $B(W \to \mathrm{e}\nu)$ in addition to $\Gamma(W \to \mathrm{e}\nu)/\Gamma(W)$. $B(W \to \mathrm{e}\nu)$ is sensitive to new physics and could be affected by new decay modes of the W boson. A new high mass resonance which decays to W or Z bosons would result in a change in their productions cross sections. The ratio of cross sections is expressed as

$$\mathrm{R} = \frac{\sigma(\mathrm{p\bar{p}} \to W)}{\sigma(\mathrm{p\bar{p}} \to \mathrm{Z})} \frac{\Gamma(W \to \mathrm{e}\nu)}{\Gamma(\mathrm{Z} \to \mathrm{e^+e^-})} \frac{\Gamma(\mathrm{Z})}{\Gamma(W)}. \tag{46}$$

The value of R can be used to extract $\Gamma(W)$, using the LEP measurement of $\Gamma(\mathrm{Z} \to \mathrm{e^+e^-})/\Gamma(\mathrm{Z})$ at the Z pole and the theory values of $\Gamma(W \to \mathrm{e}\nu)$ and $\sigma(\mathrm{p\bar{p}} \to W)/\sigma(\mathrm{p\bar{p}} \to \mathrm{Z})$. Experimentally, the value of the ratio is extracted from

$$\mathrm{R} = (\sigma_W \cdot B(W \to \mathrm{e}\nu))/(\sigma_Z \cdot B(\mathrm{Z}^0 \to \mathrm{e^+e^-})) = \tag{47}$$

$$= \frac{I_1}{I_2} \cdot \frac{\mathrm{N}_W^{candidates} - \mathrm{N}_W^{background}}{\mathrm{N}_Z^{candidates} - \mathrm{N}_Z^{background}} \cdot \frac{A_Z}{A_W} \cdot \frac{\epsilon_Z}{\epsilon_W} \tag{48}$$

where

- $\frac{I_1}{I_2}$ is the correction factor for the removal of the $\gamma^* \to \mathrm{e^+e^-}$ Drell-Yan events;
- $\mathrm{N}_W^{candidates}$ is the number of W candidates observed in the data;
- $\mathrm{N}_W^{background}$ is the number of expected background events in the W candidate sample;
- $\mathrm{N}_Z^{candidates}$ is the number of Z^0 candidates observed in the data;
- $\mathrm{N}_Z^{background}$ is the number of expected background events in the Z^0 candidate sample;
- A_Z and A_W are the acceptances for the Z^0 and W decays, including the efficiencies for the kinematic cuts on the topology of the event and the geometric acceptance of the detector;
- ϵ_Z and ϵ_W are the total efficiencies for the Z^0 and the W to pass all the reconstruction, lepton identification and trigger criteria, respectively.

In this section we will consider W events in which electrons fall in the central region of the CDF detector and Z events which fall both in the plug and in the central. In the ratio of efficiencies, the vertex, track, cluster, lepton identification and trigger efficiencies either partially or fully cancel. For central-central (CC) Z's:

$$\frac{\epsilon_Z^{CC}}{\epsilon_W} = \epsilon_{trk} \cdot \epsilon_{clus} \cdot (2 \cdot \epsilon_L - \epsilon_T) \cdot (2 - \epsilon_{trig}) \tag{49}$$

For central-plug (CP) Z's:

$$\frac{\epsilon_Z^{CP}}{\epsilon_W} = \epsilon_P \tag{50}$$

For CC+CP Z's:

$$\frac{\epsilon_Z^{CC+CP}}{\epsilon_W} = [F_{CC} \cdot \epsilon_{trk} \cdot \epsilon_{clus} \cdot (2 \cdot \epsilon_L - \epsilon_T) \cdot (2 - \epsilon_{trig})] + [F_{CP} \cdot \epsilon_P] \tag{51}$$

These efficiencies have either been reported elsewhere in this note or in [32; 33]. The factors, F_{CC} and F_{CP} are the fractions CC vs. CP accepted events obtained from Monte Carlo.

In the next section we summarize the inputs to R for when we use CC, CP, or CC+CP Z's.

23.1 Summary of $\sigma_{(W\rightarrow \mathrm{e}\nu)}$ and $\sigma_{(\mathrm{Z}^0/\gamma^*\rightarrow \mathrm{e}^+\mathrm{e}^-)}$ Measurements

Tables 32- 34 shows a summary of the $W \rightarrow e\nu$ and $Z^0 \rightarrow e^+e^-$ cross section results for CC, CP and CC+CP Z's, respectively.

We use the quantities presented in these tables to extract the ratio of cross sections. The systematic uncertainty on R is dominated by the systematic uncertainties on the acceptances, A_W and A_Z. The single effects entering in these estimates have been analyzed individually on the ratio $\mathrm{A}_Z/\mathrm{A}_W$ and the results are reported in tables 35- 37.

Many of the systematic uncertainties in the acceptances cancel in the ratio. The dominant sources comes from the variation of PDF's and in the amount of material in the detector used in the simulation.

	W's	**CC Z's**
Candidates	37584	1730
Background :		
QCD	587 ± 299	1.6 ± 7.0
$Z \rightarrow \tau^+\tau^-$	–	1.4 ± 0.3
$Z^0 \rightarrow e^+e^-$	317 ± 14	–
$W \rightarrow \tau\nu$	752 ± 17	–
$W \rightarrow e\nu$	–	1.5 ± 0.9
Total Background	1656 ± 300	4.5 ± 7.1
Signal	$35928 \pm 194_{stat} \pm 300_{syst}$	$1725.4 \pm 41.6_{stat} \pm 7.1_{syst}$
Acceptance :		
$A_{W,Z}$	$23.95 \pm 0.03_{stat}{}^{+0.34}_{-0.39}{}_{syst}$ %	$11.01 \pm 0.05_{stat}{}^{+0.23}_{-0.27}{}_{syst}$ %
A_Z/A_W	0.460 ± 0.005	
ID Efficiencies :		
ϵ_T	81.8 ± 0.8%	81.8 ± 0.8%
ϵ_L		93.4 ± 0.5%
$\epsilon_{W,Z}$	81.8 ± 0.8%	85.9 ± 0.8%
Trigger Efficiencies :		
$\epsilon_{W,Z}$	96.6 ±0.1 %	99.9 ± 0.7 %
COT Track Efficiencies (data/MC scale factor):		
$\epsilon_{W,Z}$	100.0 ±0.4 %	100.0 ± 0.8 %
Cluster Reconstruction Efficiencies (data/MC scale factor):		
$\epsilon_{W,Z}$	99.8 ±0.4 %	99.6 ± 0.8 %
Drell-Yan correction(I_1/I_2)		1.004 ± 0.001
Luminosity	72.0 ± 4.3 pb^{-1}	
Vertex cut efficiency	95.0 ± 0.4 %	
$\sigma(\text{p}\bar{\text{p}} \rightarrow \text{W} \rightarrow \text{e}\nu)/\sigma(\text{p}\bar{\text{p}} \rightarrow \text{Z}^0 \rightarrow \text{ee})$	$10.33 \pm 0.26_{stat}{}^{+0.17}_{-0.18}{}_{syst}$	

Table 32: *Summary of the results from the W cross section and CC Z cross section analyses.*

	W's	**CP Z's**
Candidates	37584	2512
Background :		
QCD	587 ± 299	39 ± 17
$Z \rightarrow \tau^+\tau^-$	–	2.3 ± 0.3
$Z^0 \rightarrow e^+e^-$	317 ± 14	–
$W \rightarrow \tau\nu$	752 ± 17	–
$W \rightarrow e\nu$	–	15.3 ± 2.6
Total Background	1656 ± 300	57 ± 17
Signal	$35928 \pm 194_{stat} \pm 300_{syst}$	$2455 \pm 50_{stat} \pm 17_{syst}$
Acceptance :		
$A_{W,Z}$	$23.95 \pm 0.03_{stat}{}^{+0.34}_{-0.39}{}_{syst}$ %	$20.87 \pm 0.07_{stat}{}^{+0.21}_{-0.22}{}_{syst}$ %
A_Z/A_W	$0.872^{+0.014}_{-0.011}$	
ID Efficiencies :		
ϵ_T	81.8 ± 0.8%	–
ϵ_P	–	88.3 ± 1.5 %
$\epsilon_{W,Z}$	81.8 ± 0.8%	88.3 ± 1.5 %
Trigger Efficiencies :		
$\epsilon_{W,Z}$	96.6 ±0.1 %	96.6 ±0.1 %
COT Track Efficiencies (data/MC scale factor):		
$\epsilon_{W,Z}$	100.0 ±0.4 %	100.0 ± 0.4 %
Cluster Reconstruction Efficiencies (data/MC scale factor):		
$\epsilon_{W,Z}$	99.8 ±0.4 %	100.0 %
Drell-Yan correction(I_1/I_2)		1.004 ± 0.001
Luminosity	72.0 ± 4.3 pb^{-1}	
Vertex cut efficiency	95.0 ± 0.4 %	
$\sigma(\text{p}\bar{\text{p}} \rightarrow \text{W} \rightarrow \text{e}\nu)/\sigma(\text{p}\bar{\text{p}} \rightarrow \text{Z}^0 \rightarrow \text{ee})$	$11.22 \pm 0.24_{stat}{}^{+0.29}_{-0.27}{}_{syst}$	

Table 33: *Summary of the results from the W cross section and CP Z cross section analyses.*

	W's	**CC+CP Z's**
Candidates	37584	4242
Background :		
QCD	587 ± 299	41 ± 18
$Z \rightarrow \tau^+\tau^-$	–	3.7 ± 0.4
$Z^0 \rightarrow e^+e^-$	317 ± 14	–
$W \rightarrow \tau\nu$	752 ± 17	–
$W \rightarrow e\nu$	–	16.8 ± 2.8
Total Background	1656 ± 300	62 ± 18
Signal	$35928 \pm 194_{stat} \pm 300_{syst}$	$4180 \pm 65_{stat} \pm 18_{syst}$
Acceptance :		
$\mathrm{A}_{W,Z}$	$23.95 \pm 0.03_{stat}{}^{+0.34}_{-0.39}{}_{syst}$ %	$31.89 \pm 0.08_{stat}{}^{+0.38}_{-0.40}{}_{syst}$ %
$\mathrm{A}_Z/\mathrm{A}_W$	1.33 ± 0.01	
F_{CC}	-	34.5 ± 0.1 %
F_{CP}	-	65.5 ± 0.1 %
ID Efficiencies :		
ϵ_T	81.8 ± 0.8%	81.8 ± 0.8%
ϵ_L		93.4 ± 0.5%
ϵ_P	–	88.3 ± 1.5 %
Trigger Efficiencies :		
$\epsilon_{W,Z}$	96.6 ±0.1 %	96.6 ± 0.1 %
COT Track Efficiencies (data/MC scale factor):		
$\epsilon_{W,Z}$	100.0 ±0.4 %	100.0 ± 0.4 %
Cluster Reconstruction Efficiencies (data/MC scale factor):		
$\epsilon_{W,Z}$	99.8 ±0.4 %	99.8 ± 0.4 %
Drell-Yan correction(I_1/I_2)		1.004 ± 0.001
Luminosity	72.0 ± 4.3 pb^{-1}	
Vertex cut efficiency	95.0 ± 0.4 %	
$\sigma(\mathrm{p\bar{p}} \rightarrow \mathrm{W} \rightarrow \mathrm{e}\nu)/\sigma(\mathrm{p\bar{p}} \rightarrow \mathrm{Z}^0 \rightarrow \mathrm{ee})$	$10.85 \pm 0.18_{stat}{}^{+0.19}_{-0.18}{}_{syst}$	

Table 34: *Summary of the results from the W cross section and CC+CP Z cross section analyses.*

Systematic	$\delta \mathbf{A_W}$	$\delta \mathbf{A_Z^{CC}}$	$\delta(\mathbf{A_Z^{CC}}/\mathbf{A_W})$
Central Energy Scale	0.08	0.01	0.0014
Plug Energy Scale	-	-	-
Central Energy Resolution	0.01	0.01	0.0001
Plug Energy Resolution	-	-	-
Electron p_T Scale	0.01	0.01	0.0001
p_T Boson	0.01	0.01	0.0003
W Recoil Energy	0.06	-	0.0011
Central Material	0.17	0.15	0.0027
Plug Material	negl.	negl.	negl.
PDF's	$^{+0.27}_{-0.34}$	$^{+0.18}_{-0.22}$	$^{+0.0025}_{-0.0032}$
Total	$\mathbf{A_W = 23.95^{+0.34}_{-0.39}}\%$	$\mathbf{A_Z^{CC} = 11.01^{+0.23}_{-0.27}}\%$	$\mathbf{A_Z^{CC}/A_W = 0.4600^{+0.0041}_{-0.0046}}$

Table 35: Systematic uncertainties in W and CC Z acceptances and on the ratio of acceptances.

Systematic	$\delta \mathbf{A_W}$	$\delta \mathbf{A_Z^{CP}}$	$\delta(\mathbf{A_Z^{CP}}/\mathbf{A_W})$
Central Energy Scale	0.08	0.07	0.0009
Plug Energy Scale	-	0.04	0.0015
Central Energy Resolution	0.01	0.01	0.0002
Plug Energy Resolution	-	0.02	0.0006
Electron p_T Scale	0.01	0.01	0.0001
p_T Boson	0.01	0.02	0.0004
W Recoil Energy	0.06	-	0.0022
Central Material	0.17	0.15	0.0013
Plug Material	negl.	0.07	0.0028
PDF's	$^{+0.27}_{-0.34}$	$^{+0.09}_{-0.12}$	$^{+0.0127}_{-0.0097}$
Total	$\mathbf{A_W = 23.95^{+0.34}_{-0.39}}\%$	$\mathbf{A_Z^{CP} = 20.87^{+0.22}_{-0.23}}\%$	$\mathbf{A_Z^{CP}/A_W = 0.8717^{+0.0134}_{-0.0106}}$

Table 36: Systematic uncertainties in W and CP Z acceptances and on the ratio of acceptances.

Systematic	δA_W	δA_Z^{CC+CP}	$\delta(A_Z^{CC+CP}/A_W)$
Central Energy Scale	0.08	0.07	0.0021
Plug Energy Scale	-	0.04	0.0015
Central Energy Resolution	0.01	0.02	0.0003
Plug Energy Resolution	-	0.02	0.0006
Electron p_T Scale	0.01	0.01	0.0003
p_T Boson	0.01	0.02	0.0003
W Recoil Energy	0.06	-	0.0033
Central Material	0.17	0.30	0.0027
Plug Material	negl.	0.07	0.0028
PDF's	$^{+0.27}_{-0.34}$	$^{+0.21}_{-0.24}$	$^{+0.0101}_{-0.0077}$
Total	$A_W = 23.95^{+0.34}_{-0.39}\%$	$A_Z^{CC+CP} = 31.89^{+0.39}_{-0.41}\%$	$A_Z^{CC+CP}/A_W = 1.332^{+0.0117}_{-0.0097}$

Table 37: Systematic uncertainties in W and CC+CP Z acceptances and on the ratio of acceptances.

23.2 Results on R

Using the numbers in table 32- 34 and substituting in the expression 48 we find

$$\mathrm{R} = 10.33 \pm 0.26_{stat}{}^{+0.17}_{-0.18}{}_{syst}, \quad \text{for CC Z's} \tag{52}$$

$$\mathrm{R} = 11.22 \pm 0.24_{stat}{}^{+0.29}_{-0.27}{}_{syst}, \quad \text{for CP Z's} \tag{53}$$

$$\mathrm{R} = 10.85 \pm 0.18_{stat}{}^{+0.19}_{-0.18}{}_{syst}, \quad \text{for CC + CP Z's} \tag{54}$$

This quantity can be compared with the value obtained with the value published in Run 1 of 10.90±0.43 [66]. The NNLO calculation at $\sqrt{s} = 1.96$, $\mathrm{R} = 10.67 \pm 0.15$ [47], calculated by W.Sakumoto agrees with our measured value within 1σ. The largest theoretical uncertainty on the W and Z cross sections used for this calculation comes from the choice of the PDFs; for CTEQ6 it is assigned to be 3.5%. This calculation can be compared with the value 10.92 obtained by Stirling [55] using the values reported in tables 28 and 30. We choose to compare our measurement to the calculation in [47] since the propagation of the theoretical uncertainties on the ratio of the cross sections is unknown for the calculation in [55].

From formula 46 given above we can extract the total width of the W boson $\Gamma(W)$. We do this after combining the ratio of cross sections in the muon channel [67; 68]; details are given in [68]

Part IX

Conclusions

Using 72.0 pb^{-1} of good Run II CDF data we measure:

$$\sigma \cdot B(p\bar{p} \to W \to e\nu) = (2.781 \pm 0.015(stat.)^{+0.057}_{-0.062}(syst.) \pm 0.167(lum.))\ \mathrm{nb} \tag{55}$$

$$\sigma_Z \cdot Br(\mathrm{Z}^0 \to \mathrm{e}^+\mathrm{e}^-) = 269.3 \pm 6.5(stat.)^{+7.2}_{-8.0}(syst.) \pm 16.1(lum.)\ \mathrm{pb.}\ [\mathrm{CC}] \tag{56}$$

$$\sigma_Z \cdot Br(\mathrm{Z}^0 \to \mathrm{e}^+\mathrm{e}^-) = 248.1 \pm 4.9(stat.) \pm 5.9(syst.) \pm 14.8(lum.)\ \mathrm{pb.}\ [\mathrm{CP}] \tag{57}$$

$$\sigma_Z \cdot Br(\mathrm{Z}^0 \to \mathrm{e}^+\mathrm{e}^-) = 256.3 \pm 3.9(stat.) \pm 5.3(syst.) \pm 15.3(lum.)\ \mathrm{pb.}\ [\mathrm{CC}+\mathrm{CP}] \tag{58}$$

The CP and combined CC+CP cross sections are reported elsewhere [32; 33].

$$\mathrm{R} = 10.33 \pm 0.26(stat.)^{+0.17}_{-0.18}(syst.),\ \text{for CC Z}'\text{s} \tag{59}$$

$$\mathrm{R} = 11.22 \pm 0.24(stat.)^{+0.29}_{-0.27}(syst.),\ \text{for CP Z}'\text{s} \tag{60}$$

$$\mathrm{R} = 10.85 \pm 0.18(stat.)^{+0.19}_{-0.18}(syst.),\ \text{for CC + CP Z}'\text{s} \tag{61}$$

Combinations of these measurement with the muon channel are reported in [67; 68].

Part X

Acknowledgments

We would like to thank Electron Task Force (ETF), the W/Z cross-section group, and the luminosity group for their contributions, help and fruitful discussions. We also like to thank W. J. Stirling for providing cross section predictions at 1.96 TeV. We thank Ashutosh Kotwal for providing fruitful comments and guidance of the analysis.

References

[1] K. Hagiwara et al. *Phys. Rev.* **D** *66*, (010001-294), 2002. 10

[2] K. Hagiwara et al. *Phys. Rev.* **D** *66*, (010001-282), 2002. 10

[3] W.J. Stirling A.D. Martin, R.G. Roberts and R.S. Thorne. hep-ph/0007099, 2000. URL NNLO. 10

[4] R. Hamberg, T. Matsuura, and W.L. van Neerven. Nucl. Phys. **B345**, 331, 1990). 10

[5] R. Hamberg, T. Matsuura, and W.L. van Neerven. Nucl. Phys. **B359**, 343, 1991. 10

[6] W.L. van Neerven and E.B. Zijlstra. Nuch. Phys. **B382**, 11, 1992. 10

[7] UA1 Collaboration (C. Albajar *et al.*). Z. Phys. C44, (15), 1989. 10

[8] UA2 Collaboration (J. Alitti *et al.*). Z. Phys. C47, (11-22), 1990. 10

[9] T. Affolder *et al.* (CDF Collaboration). Phys. Rev. Lett. **84**, 845, 2000. 10

[10] F. Abe *et al.* (CDF Collaboration). Phys. Rev. **D59**,052002, 1999. 10

[11] F. Abe *et al.* (CDF Collaboration). Phys. Rev. Lett. **76**, 3070, 1996. 10

[12] B. Abbott *et al.* (D0 Collaboration). Phys. Rev. D60, 052003, 1999. 10

[13] Evelyn Thomson. Description of data samples for Top Group for Summer 2003. URL CDF 6548. 11

[14] Eva Halkiadakis. Criteria and Good Run Luminosity Sum, 2003. URL GOOD RUN LIST. 12

[15] Jacobo Konigsberg. CDFs Official Luminosity Web Page. URL DFC Luminosity. 13

[16] D. Acosta *et al.* A First Look at the CLC Luminosity Measurements, 2002. URL CDF 6052. 13

[17] J.Konigsberg S.Klimenko. Average cross-section of the inelastic $p\bar{p}$ scattering at 1.8 TeV, 2003. URL CDF 6314. 13

[18] Beate Heinemann. Offline Calibration of the Calorimeter, 2003. URL CDF 6406. 13

[19] K. Yasuoka *et al.* *NIM*, A(267), 1988. 13

[20] Beate Heinemann Angela Wyatt. Correction for Leakage Energy in the Central and Plug Calorimeters in Run II, 2002. URL CDF 6167. 14, 20

[21] Peter T. Beam Constrained COT Tracking, 2002. URL BC. 14

[22] M. Coca *et al.* A First Look at Run 2 High p_T Electrons, 2001. URL CDF 5803. 14

[23] Giulia Manca Young-Kee Kim. Z to electrons Cross Section measurement with Run II data, 2003. URL CDF 6281. 14, 94

[24] W.J. Robertson M. Brozovic, A.T. Goshaw. Jet Vertex Resolution in a Run 1 Z Event Sample, 2001. URL CDF 5698. 14

[25] Torbjorn Sjöstrand, Leif Lonnblad, and Stephen Mrenna. Pythia 6.203: Physics and manual *and* http://www.thep.lu.se/ torbjorn/pythia.html. *Comput. Phys. Commun.*, 135(238), 2001. URL PYTHIA. 15, 16

[26] CTEQ. URL CTEQ. 15

[27] H.L. Lai *et al.* *Eur. Phys. J.*, C(12):375, 2000. 16

[28] F. Abe *et al.* *Phys. Rev. Lett*, 84:845, 2000. 16

[29] F. Abe *et al.* *Phys. Rev.*, D(63):011101R, 2000. 17

[30] Laurent Vacavant. GEANT Description of the CDF Inner Tracker Passive Material, 2002. URL CDF 5825. 17

[31] Shanhuei(Sunny) Chuang *et al.* Estimate of the amount of material in the CDF tracker using high-Pt electrons, 2003. URL CDF 6573. 18

[32] A. Robson *et al.* A Measurement of $\sigma \cdot B$ ($Z^0 \rightarrow e^+e^-$) Using Run 2 Central and Plug Electrons in 72 pb^{-1}, 2004. URL CDF 6642. 20, 108, 114

[33] P. Renton A. Robson, G. Manca. A Combined Measurement of $\sigma \cdot B$ ($Z^0 \rightarrow e^+e^-$) using Central-Central and Central-Plug Events in 72 pb^{-1}, 2004. URL CDF 6896. 20, 108, 114

[34] Electron Task Force. Electron Baseline Cuts for Summer 2003. URL BASELINE ELE. 20

[35] Sarah Lockwitz Mircea Coca, Eva Halkiadakis. Central Electron Identification Efficiencies for Summer 2003 Conferences, 2003. URL CDF 6580. 20, 94

[36] Robert G. Wagner. Electron Identification for Run II: Algorithms, 2000. URL CDF 5456. 20

[37] Peter Wilson. Calorimeter Isolation and Lateral Shower Leakage for Photons and Electrons, 1997. URL CDF 4170. 20

[38] Robert G. Wagner (ANL). Understanding and Using Lshr, 2003. URL CDF 6249. 21

[39] Jian Kang. W/Z Cross Section Meeting, June 3, 2003. URL "Dijet MC bkg studies". 34

[40] Ken Bloom. Estimating QCD Backgrounds to W Production, 2003. URL CDF 6559. 37

[41] Greg Veramendi *et al.* Measurement of forward-backward asymmetry using dielectron candidates. CDF Note 5989, . URL CDF 5989. 40

[42] J.Huston et al. New generation og parton distributions with uncertainties from global qcd analysis. *JHEP*, (07):12, 2002. 62

[43] E. Halkiadakis *et al.* PDF Uncertainties for W and Z Cross Section Measurements, 2004. URL CDF 6890. 62

[44] Giulia Manca Young-Kee Kim. $z^0 \rightarrow e^+e^-$ cross section measurement with run ii data, 2003. URL CDF 6202. 77

[45] F. Abe et al. *Phys.Rev.Lett.*, 64, 1990. 77, 102

[46] J. Wahl. *W and Z Boson Acceptances in the R analysis* cdf note 4599. June 21, 1999. CDF Note 4599. 77

[47] W.K. Sakumoto. W/Z Cross Section Predictions for sqrt(s)=1.96 TeV, 2003. URL CDF 6341. 81, 102, 113

[48] Jason Nielsen *et al.* Trigger Efficiencies for high E_T Electrons. CDF Note 6234, Version 2, . URL CDF 6234. 83

[49] Brian Winer Richard Hughes, Evelyn Thomson. Performance Study of the eXtremely Fast Tracker in High Luminosity. CDF Note 5986. URL CDF 5986. 83

[50] D. Glenzinski *et al.* Run IIa COT Tracking Efficiency, 2003. URL CDF 5973. 85, 96

[51] Rick J. Tesarek Heather Ray, Monica Tecchio. Level 2 Electron Trigger Efficiencies for Run II. CDF Note 6098. URL CDF 6098. 91

[52] G.Veramendi G.Manca. ETF Meeting, February 4, 2004. URL "Central Electron Reconstruction Efficiency". 98

[53] P. Derwent W. Badgett. Event Z Vertex Cut Efficiency as a Luminosity Correction for Run IA, 1994. URL CDF 2703. 98

[54] W.K. Sakumoto and A. Hocker. Event $|Zvtx| < 60$ cm Cut Acceptance for Run II, 2003. URL CDF 6660. 99

[55] A.D. Martin *et al.* Phys. Lett. B **531**, 216 , 2002. 101, 103, 106, 113

[56] F. Abe *et al.* *Phys. Rev. Lett.*, 76:3070, 1996. 101

[57] F. Abe et al. Measurement of $\sigma \cdot b(w \to e\nu)$ and $\sigma \cdot b(z\ 0 \to e\ +e\ -)$ in $p\bar{p}$ collisions at $\sqrt{s} = 1.8$ tev. *Phys. Rev. Lett.*, 76:3070–3075, 1996. hep-ex/9509010. 102

[58] D. Cronin-Hennessy, A. Beretvas, and P. F. Derwent. Luminosity monitoring and measurement at cdf. *Nuclear Instruments and Methods in Physics Research*, A 443/1:37–50, 2000. 102

[59] T. Affolder et al. Measurement of d(sigma)/dy for high mass drell-yan e+ e- pairs from p anti-p collisions at $\sqrt{s} = 1.8$ tev. *Phys. Rev.*, D63:011101, 2001. hep-ex/0006025. 102

[60] W.J. Stirling. *private communication.* 102, 103

[61] R. Hamberg, W.L. van Neerven, and T. Matsuura. . *Nucl.Phys.*, B359, 1991. 102

[62] R.V. Harlander and W.B. Kilgore. . *Phys.Rev.Lett.*, 88, 2002. 102

[63] J. Pumplin et al. New Generation of Parton Distributions with Uncertainties from Global QCD Analysis . hep-ph/0201195. 102

[64] A.D. Martin et al. Uncertainties of predictions from parton distributions. I: experimental errors. . hep-ph/0211080. 102

[65] A.D. Martin, R.G. Roberts, W.J. Stirling, and R.S. Thorne. Uncertainties of predictions from parton distributions I: Experimental errors, hep-ph/0211080. 2002. 103

[66] F.Abe *et al.* *Phys.Rev.*, **D52**, 1995. 113

[67] D. Amidei *et al.* Measurements of $W \to \mu\nu$ and $Z\to \mu^+\mu^-$ production cross sections and R using CDF Run II Data. CDF Note 6711, . URL CDF 6711. 113, 114

[68] Michael Schmitt. Updated Combination of e and mu Measurements of the W and Z Cross Sections and Their Ratio, 2004. URL CDF 6895. 113, 114